UNIVERSITÉ DE LORRAINE | BIBLIOTHÈQUES UNIVERSITAIRES

AVERTISSEMENT

Ce document est le fruit d'un long travail approuvé par le jury de soutenance et mis à disposition de l'ensemble de la communauté universitaire élargie.

Il est soumis à la propriété intellectuelle de l'auteur. Ceci implique une obligation de citation et de référencement lors de l'utilisation de ce document.

D'autre part, toute contrefaçon, plagiat, reproduction illicite encourt une poursuite pénale.

Contact bibliothèque : ddoc-theses-contact@univ-lorraine.fr
(Cette adresse ne permet pas de contacter les auteurs)

LIENS

Code de la Propriété Intellectuelle. articles L 122. 4
Code de la Propriété Intellectuelle. articles L 335.2- L 335.10
http://www.cfcopies.com/V2/leg/leg_droi.php
http://www.culture.gouv.fr/culture/infos-pratiques/droits/protection.htm

THÈSE

présentée pour l'obtention du titre de

DOCTEUR de L'UNIVERSITÉ DE LORRAINE

Spécialité Mécanique des Matériaux

par

Youssef IDRISSI

Nanoindentation and Bayesian Inference for Robust Characterization of Single Crystal Elastic Constants in Cubic Materials

---

Soutenue le 25 février 2025, à Metz, devant le jury composé de :

Shabnam ARBAB CHIRANI	Professeure des Universités, ENSTA Brest, IRDL	*Rapporteure*
Marc FIVEL	Directeur de Recherche, CNRS, SIMaP	*Rapporteur*
Salima BOUVIER	Professeure des Universités, UTC, Lab. Roberval	*Présidente*
Célia CAER	Ingénieure de Recherche, ENSTA Bretagne, IRDL	*Examinatrice*
Thiebaud RICHETON	Chargé de Recherche, CNRS, LEM3	*Co-Directeur*
Jean-Sébastien LECOMTE	Chargé de Recherche, CNRS, LEM3	*Directeur*
Damien TEXIER	Chargé de Recherche, CNRS, ICA	*Invité*

Acknowledgements

First of all, I wanna dedicate this work to my father who passed away in the final stages of my thesis. His loss has been a hard hit, but his wisdom, kindness, and unwavering support shaped me into the person I am today. Him and my mother were always there for me, providing unconditional love and support. I would not be where I am today without them. I am thankful everyday for the values they have instilled in me and I hope that I am making them proud.

I also wanna express my sincere gratitude to the members of the jury for taking the time to evaluate my work and to be there on the day of my defense. I am sure that their expertise and constructive feedback will be invaluable to the refinement of this thesis.

This work would not have been possible without my thesis directors, Jean-Sébastien and Thiebaud. Your expertise and insightful advice have been instrumental in shaping this work. You also went beyond and above, acting as a second family and supporting me during my hardships. I could not have wished for better thesis directors. Thank you for believing in my potential. This thesis is as much a reflection of your mentorship as it is of my efforts.

I can't forget my close friends Mashechka, Badia, Hniya, Zakariae, Younes, and Zidane. You have been a constant source of support, laughter, and encouragement. Your friendship has been a beacon of light during this journey, lifting my spirits during the toughest moments and celebrating every milestone with me. This achievement would not have been possible without your presence in my life.

Finally, I want to thank the administrative staff at LEM3. You've made every administrative procedure seamless by being very proactive, and very reactive when problems arose.

Abstract

Estimating the elastic constants of materials constitutes a real challenge, particularly when dealing with multiphase materials. For single-phase materials, scientists have used techniques such as ultrasonic pulse echo or a combination of X-rays and diffuse thermal scattering. For multiphase materials, these techniques, if used alone, can only give the macroscopic elastic constants of the materials, and cannot distinguish the elastic constants of a specific phase. In the present work, a new protocol is presented using a coupling of nanoindentation experiments, Vlassak and Nix model, and Bayesian inference to statistically estimate the elastic constants of cubic materials.

The originality of our method lies in writing the cubic stiffness tensor not in terms of the usual constants but in terms of the directional Young's modulus $E_{<100>}$,the directional Poisson's ratio $\nu_{<100>}$ and the Zener coefficient A. Interestingly, $E_{<100>}$ then becomes a pre-factor of the stiffness tensor so that indentation modulus ratios depend on just two dimensionless parameters, A and $\nu_{<100>}$.

Consequently, we have developed a Bayesian inference code that considers indentation modulus ratios and varies only A and $\nu_{<100>}$. This approach has many advantages: computation time is greatly reduced, the use of indentation modulus ratios increases the number of data and reduces the influence of the calibration parameters, the limits of $\nu_{<100>}$ and the lower limit of A are known and are material's independent and the upper limit of A can be easily conjectured unlike the ranges of C_{ij} constants, which are much harder to estimate a priori.

Furthermore, the method efficiency allows for continuous variation of the uncertainty considered in the experimental moduli, leading to stabilized Bayesian inference results. The choice of the

finally retained values is thus simplified, converging to the uniqueness of the single crystal elastic constants. This method is applied to high-purity Ni, as a known sample material, and Inconel 718, as a less-known material. The predicted elastic constants align well with literature data. The findings of this research have been published in the journal Acta Materialia.

Résumé court en Français

Estimer les constantes élastiques des matériaux constitue un véritable défi, en particulier lorsqu'il s'agit de matériaux multiphasés. Pour les matériaux monophasés, les scientifiques ont utilisé des techniques telles que l'écho ultrasonique par impulsion ou une combinaison de rayons X et de diffusion thermique. Pour les matériaux multiphasés, ces techniques, si elles sont utilisées seules, ne peuvent fournir que les constantes élastiques macroscopiques des matériaux, sans permettre de distinguer les constantes élastiques d'une phase spécifique.

Dans le présent travail, un nouveau protocole est présenté en combinant des expériences de nanoindentation, le modèle de Vlassak et Nix, ainsi que linférence Bayésienne pour estimer statistiquement les constantes élastiques des matériaux cubiques. L'originalité de cette méthode réside dans l'écriture du tenseur de rigidité cubique non pas en termes des constantes habituelles, mais en termes du module de Young directionnel $E_{<100>}$, du coefficient de Poisson directionnel $\nu_{<100>}$, et du coefficient de Zener A. De manière intéressante, $E_{<100>}$ devient alors un facteur prépondérant du tenseur de rigidité, de sorte que les rapports des modules d'indentation anisotropes dépendent uniquement de deux paramètres sans dimension, A et $\nu_{<100>}$.

Par conséquent, nous avons développé un protocole d'inférence Bayésienne qui prend en compte les rapports des modules d'indentation anisotropes et ne fait varier que A et $\nu_{<100>}$. Cette approche présente de nombreux avantages : le temps de calcul est considérablement réduit, l'utilisation des rapports des modules d'indentation augmente le nombre de données et réduit l'influence des paramètres de calibration et les incertitudes expérimentales. De plus, les limites de $\nu_{<100>}$ et la limite inférieure de A sont connues et indépendantes du matériau, tandis que la limite supérieure de

A peut être facilement conjecturée, contrairement aux plages des constantes C_{ij}, qui sont beaucoup plus difficiles à estimer.

En outre, l'efficacité de la méthode permet une variation continue de l'incertitude considérée dans les modules expérimentaux, ce qui conduit à des résultats stabilisés de l'inférence bayésienne. Le choix des valeurs finalement retenues est ainsi simplifié, convergeant vers l'unicité des constantes élastiques des monocristaux. Cette méthode est appliquée au nickel de haute pureté, utilisé comme matériau de référence connu, et à l'Inconel 718, un matériau moins connu. Les constantes élastiques prédites s'alignent bien avec les données de la littérature. Les résultats de cette recherche ont été publiés dans la revue Acta Materialia.

Résumé long en Français

Estimer les constantes élastiques des matériaux constitue un véritable défi, en particulier lorsqu'il s'agit de matériaux multiphasés. Pour les matériaux monophasés, les scientifiques ont utilisé des techniques telles que l'écho ultrasonique par impulsion ou une combinaison de rayons X et de diffusion thermique. Pour les matériaux multiphasés, ces techniques, si elles sont utilisées seules, ne peuvent fournir que les constantes élastiques macroscopiques des matériaux, sans permettre de distinguer les constantes élastiques d'une phase spécifique.

Dans le présent travail, un nouveau protocole est présenté en combinant des expériences de nanoindentation, le modèle micromécanique de Vlassak et Nix (Vlassak *et al.*, 1993; Vlassak *et al.*, 1994; Vlassak *et al.*, 2003), ainsi que l'inférence Bayésienne pour estimer statistiquement les constantes élastiques des matériaux cubiques.

Le premier chapitre examine les bases théoriques et méthodologiques essentielles à la compréhension du sujet de recherche. Il s'attarde sur les principaux concepts et modèles analytiques qui structurent le domaine d'étude, tout en identifiant les limites des approches existantes. Une revue approfondie de la littérature met en exergue les modèles de Vlassak et Nix (Vlassak *et al.*, 1993; Vlassak *et al.*, 1994; Vlassak *et al.*, 2003) et d'Oliver et Pharr (Oliver *et al.*, 1992; Oliver *et al.*, 2004), couramment utilisés pour interpréter les résultats expérimentaux en nanoindentation. Sur le plan expérimental, la nanoindentation instrumentée constitue une technique clé pour caractériser les propriétés mécaniques locales. L'analyse critique des études antérieures met en évidence les divergences théoriques et méthodologiques qui persistent dans la discipline. Une attention particulière est portée aux stratégies d'amélioration des modèles, notamment par la prise

en compte de l'anisotropie élastique dans les formulations analytiques. De plus, l'application de méthodes bayésiennes pour la calibration des modèles constitue une avancée prometteuse, permettant de réduire l'incertitude associée aux paramètres expérimentaux et d'améliorer la robustesse des prédictions.

Le second chapitre détaille les procédures expérimentales employées pour déterminer avec précision les constantes élastiques monocristallines (SECs) de matériaux cubiques par nanoindentation. La complexité du comportement des matériaux, en particulier concernant les matériaux plycristallins et multiphasés, exige une attention particulière à chaque étape du processus expérimental pour garantir des résultats fiables et reproductibles. Le nickel de haute pureté (99,99%) a été sélectionné comme matériau de référence en raison de ses propriétés élastiques bien documentées. L'Inconel 718, un matériau plus complexe avec un profil SEC moins établi, a été choisi comme matériau cible. Les échantillons ont été soumis à des techniques de préparation de surface pour minimiser la rugosité et assurer des conditions optimales pour les mesures de nanoindentation. La diffraction d'électrons rétrodiffusés (EBSD) a été utilisée pour caractériser l'orientation cristallographique des grains. L'étalonnage de l'indenteur sphérique est essentiel pour la précision des mesures. Deux méthodes d'étalonnage ont été utilisées : une basée sur la géométrie du pénétrateur et une autre utilisant la méthode de Kalidindi (Kalidindi *et al.*, 2008; Pathak *et al.*, 2015). Les essais de nanoindentation ont été réalisés en mode dynamique pour obtenir des valeurs stabilisés de modules de nanoindentation avec la profondeur (Fig. 1). Les paramètres ont été soigneusement choisis pour optimiser l'extraction des propriétés élastiques. La préparation minutieuse des échantillons a permis d'obtenir des surfaces de haute qualité, essentielles pour la précision des mesures de nanoindentation. La cartographie de nanoindentation à haute vitesse a, quant à elle, permis de visualiser la distribution spatiale des modules de nanoindentation, révélant une excellente corrélation avec les orientations cristallographiques mesurées par EBSD.

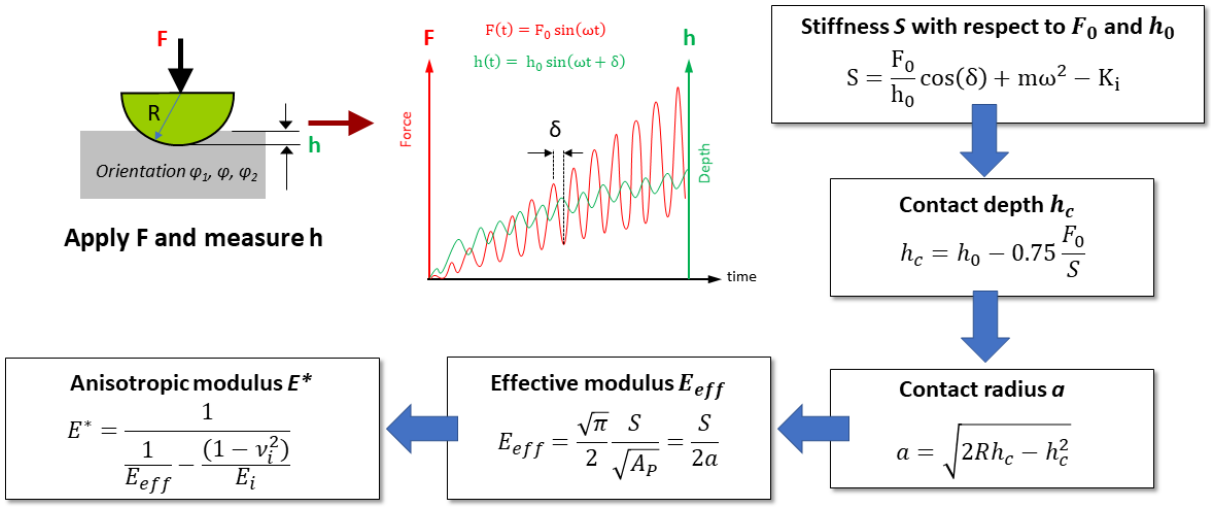

Figure 1: Protocole expérimental pour obtenir E^*
en utilisant une pointe sphérique et le mode Sinus.

Le troisième chapitre détaille la mise en œuvre numérique du modèle de Vlassak et Nix (Vlassak *et al.*, 1993; Vlassak *et al.*, 1994; Vlassak *et al.*, 2003), un élément critique pour le calcul du module anisotrope E^*. Le modèle, ancré dans la méthode de la fonction de Green de surface (Barnett *et al.*, 1975) et le formalisme de Stroh (Stroh, 1958), est essentiel pour les études de nanoindentation visant à comprendre les propriétés des matériaux à l'échelle nanométrique. Nous explorons le cadre computationnel utilisé pour dériver efficacement E^*. Le processus de détermination de E^* utilise un formalisme matriciel qui améliore l'efficacité de l'approche originale de Vlassak et Nix (Vlassak *et al.*, 1993; Vlassak *et al.*, 1994; Vlassak *et al.*, 2003). Ce formalisme implique la résolution d'un problème aux valeurs propres généralisé, à partir duquel ces dernières et les vecteurs propres sont utilisés pour construire les matrices nécessaires au calcul de E^*. La mise en œuvre numérique tire parti de la quadrature de Gauss-Legendre pour résoudre l'équation d'intégrale de ligne, améliorant ainsi considérablement l'efficacité de calcul sans compromettre la précision. Cette méthode permet une évaluation extrêmement rapide des modules E^*. Des études de convergence sont fournies pour démontrer la performance du modèle en termes de vitesse et de précision. Les résultats confirment l'efficacité de la quadrature de Gauss-Legendre dans l'obtention d'une convergence rapide et d'une haute précision dans les calculs. L'exactitude et l'applicabilité du modèle sont validées à travers diverses études de cas couvrant différentes orientations cristallographiques et propriétés des matériaux (Fig. 2). Ces études aident à comprendre le comportement du modèle dans

des conditions variées et garantissent sa fiabilité dans la prédiction des propriétés des matériaux.

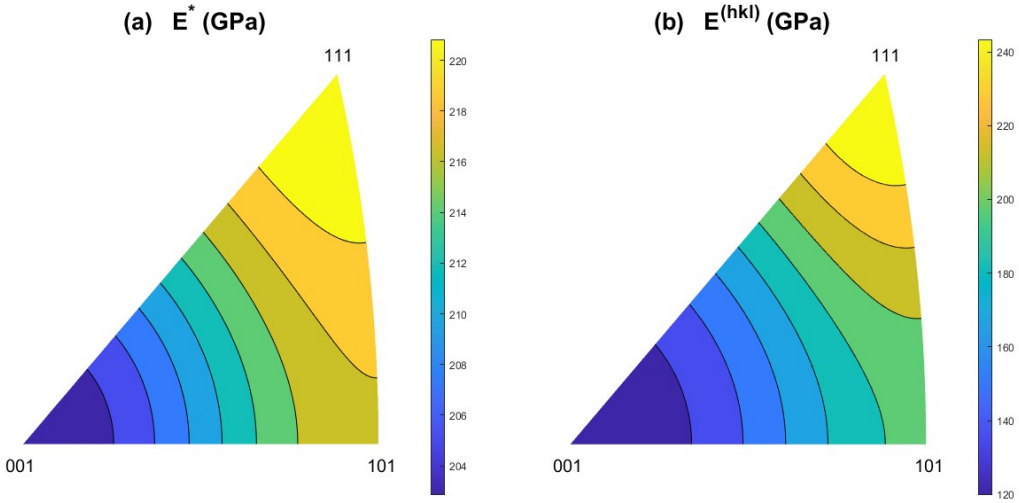

Figure 2: Contour IPF le long de la direction d'indentation de (a) E^* en utilisant le model de Vlassak et Nix et (b) du module de Young directionnel le long de l'axe d'indentation $E^{(hkl)}$. Les constantes élastiques cubique du Ni de Yamamoto, 1950 ont été utilisées: $C_{11} = 244\,\text{GPa}$, $C_{12} = 158\,\text{GPa}$ et $C_{44} = 102\,\text{GPa}$.

Le quatrième chapitre introduit l'inférence bayésienne comme un outil statistique robuste pour estimer les paramètres des matériaux, en particulier les constantes élastiques monocristallines (SEC), en intégrant les connaissances préalables avec les données expérimentales. Le chapitre souligne les avantages des méthodes bayésiennes pour traiter les incertitudes inhérentes aux mesures expérimentales et présente une méthodologie détaillée pour appliquer l'inférence bayésienne aux données de nanoindentation couplées au modèle de Vlassak et Nix (Vlassak *et al.*, 1993; Vlassak *et al.*, 1994; Vlassak *et al.*, 2003). L'inférence Bayésienne utilise le théorème de Bayes pour mettre à jour les estimations de probabilité des paramètres matériaux à mesure que de nouvelles données deviennent disponibles et emploie des fonctions de vraisemblance pour quantifier l'accord entre les données observées et les prédictions du modèle. Le chapitre se concentre sur le raffinement de l'estimation des constantes élastiques à partir des données de nanoindentation. Le modèle de Vlassak et Nix (Vlassak *et al.*, 1993; Vlassak *et al.*, 1994; Vlassak *et al.*, 2003) est intégré avec des méthodes statistiques bayésiennes pour estimer les SEC des matériaux cubiques. Les incertitudes associées aux estimations des SEC sont ensuite quantifiées, fournissant une compréhension plus complète des propriétés des matériaux. La mise en oeuvre de notre méthode bayésienne originale

pour l'identification des constantes élastiques cubiques est détaillée. Celle-ci inclut l'utilisation de rapport de modules de nanoindentation, ce qui permet de faire varier 2 paramètres au lieu de 3. De plus, ces paramètres peuvent être choisis comme le facteur d'anisotropie élastique A et le coefficient de Poisson directionnel $\nu_{<100>}$ qui ont le grand avantage d'être adimensionels et d'avoir des bornes indépendantes des matériaux considérés qui sont données par les conditions de stabilité élastique. Ce chapitre prépare le terrain pour les résultats ultérieurs en établissant les fondations théoriques et computationnelles. Il souligne le rôle de l'inférence bayésienne dans l'amélioration de la précision des estimations des SEC.

Le chapitre final présente une analyse complète des propriétés élastiques du nickel de haute pureté et de l'Inconel 718 en utilisant les expériences de nanoindentation et l'inférence bayésienne pour extraire le facteur d'anisotropie élastique A et le coefficient de Poisson directionnel $\nu_{<100>}$. Le chapitre est structuré autour de différents ensembles de données expérimentales et méthodologiques, c'est à dire les cartographies de nanoindentation à haute vitesse (HSNM) avec des pointes Berkovich et les tests de nanoindentation sphérique. La présentation des résultats expérimentaux commence par une analyse des figures de pole inverses et des cartes de E^* obtenus par HSNM. Les distributions 2D du score R^2 et la distribution de probabilité postérieure (Fig.3) sont ensuite comparées. A partir de ces dernières, nous établissons les distributions marginales postérieures de chaque paramètre et discutons comment déterminer les constantes élastiques retenues au final. Nous évaluons ensuite les implications des résultats, les perspectives sur la validité du modèle de Vlassak et Nix (Vlassak *et al.*, 1993; Vlassak *et al.*, 1994; Vlassak *et al.*, 2003) et le potentiel de la combinaison des expériences de nanoindentation avec l'inférence statistique.

Pour conclure, nous avons développé un protocole d'inférence Bayésienne qui prend en compte les rapports des modules d'indentation anisotropes et ne fait varier que A et $\nu_{<100>}$. Cette approche présente de nombreux avantages : le temps de calcul est considérablement réduit, l'utilisation des rapports des modules d'indentation augmente le nombre de données et réduit l'influence des paramètres de calibration et les incertitudes expérimentales. De plus, les limites de $\nu_{<100>}$ et la limite inférieure de A sont connues et indépendantes du matériau, tandis que la limite supérieure de A peut être facilement conjecturée, contrairement aux plages des constantes C_{ij}, qui sont beaucoup

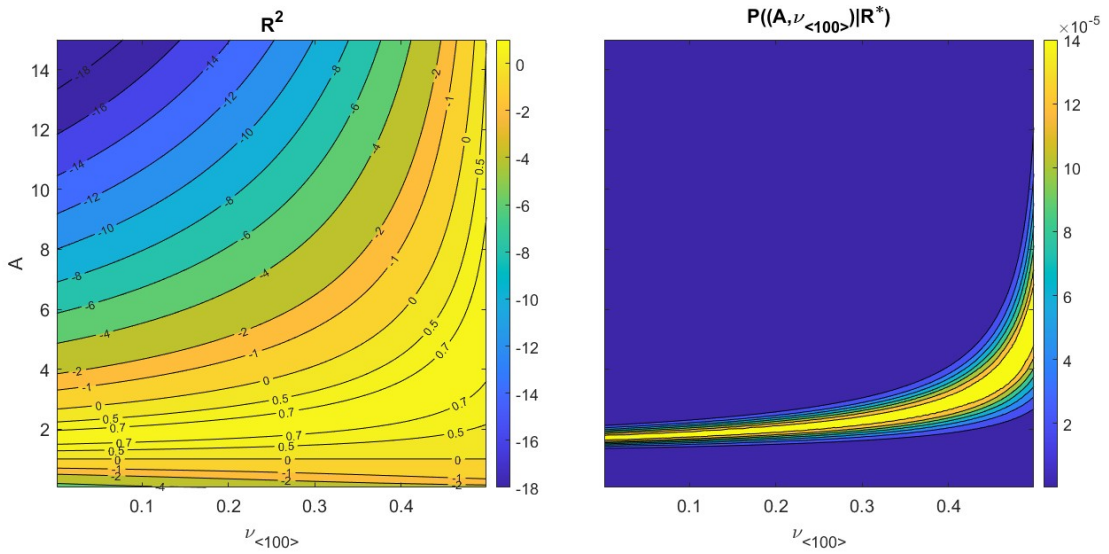

Figure 3: Distribution 2D du score R^2 et de la probabilité postérieur $P\left(\left(A, \nu_{\langle 100\rangle}\right)|R^*\right)$ pour $\sigma_{E^*} = 50\,\text{GPa}$ en fonction de A et $\nu_{\langle 100\rangle}$ pour l'IN718.

plus difficiles à estimer a priori, en particulier pour des matériaux mal connus.

Ref.	A	$\nu_{\langle 100\rangle}$	$E_{\langle 100\rangle}$	C_{11}	C_{12}	C_{44}
Present study	2.7	0.38	108	202	124	106
Martin *et al.*, 2014	2.7	0.41	114	260	179	110
Schröder *et al.*, 2023	2.4	0.35	124	201	109	110
Haldipur, 2006	2.0	0.36	141	242	139	104

Table 1: Valeurs de A, $\nu_{\langle 100\rangle}$ et $E_{\langle 100\rangle}$ (en GPa) retenues après les simultions d'inférence Bayésienne pour l'Inconel 718 et leur conversion en valeurs de C_{11}, C_{12} et C_{44} (en GPa) (présente étude). Comparaisons avec les valeurs de la littérature (données sous forme de C_{11}, C_{12} et C_{44} et converties en termes de A, $\nu_{\langle 100\rangle}$ et $E_{\langle 100\rangle}$

En outre, l'efficacité de la méthode permet une variation continue de l'incertitude considérée dans les modules expérimentaux, ce qui conduit à des résultats stabilisés de l'inférence bayésienne. Le choix des valeurs finalement retenues est ainsi simplifié, convergeant vers l'unicité des constantes élastiques monocristallines. Cette méthode a été appliquée au nickel de haute pureté, utilisé comme matériau de référence connu, et à l'Inconel 718, un matériau moins connu. Les constantes élastiques prédites s'alignent bien avec les données de la littérature. Les résultats de cette recherche ont été publiés dans la revue Acta Materialia.

Contents

Introduction **1**

Chapter 1 Literature Review **4**

1.1 Introduction 4

1.2 Effects of elastic anisotropy on materials mechanical behavior 5

Generalized Hooke's law and cubic symmetry 5

Elastic constant averages of a polycrystal with cubic symmetry 7

Effect of elastic anisotropy on incompatibility stresses at grain boundaries . . 9

1.3 Measurement of single-crystal elastic constants by traditional methods 13

Ultrasonic waves 13

Supersonic pulse echo 14

First obstacle: Single-phase polycrystalline materials 15

Second obstacle: Multiphase polycrystalline materials 16

1.4 Characterization by nanoindentation 17

1.4.1 Nanoindentation protocols 18

Method of Oliver & Pharr 18

Method of Field & Swain 21

Continuous Stiffness Measurement (CSM) 24

Method of Pathak & Kalidindi 24

1.4.2 Analytical methods to calculate the anisotropic modulus E^* 28

Substituting E^* with the directional Young's modulus $E^{(hkl)}$ 28

Vlassak and Nix's micromechanical model 29

1.4.3 Nanoindentation as an emergent method to estimate single-crystal elastic constants . . . 32
1.5 Identification of material parameters by Bayesian inference . . . 36
1.6 Conclusion . . . 41

Chapter 2 Experimental Procedure **43**
2.1 Introduction . . . 43
2.2 Material's choice . . . 44
2.3 Sample preparation . . . 45
2.3.1 High Purity Ni . . . 45
2.3.2 Inconel718 . . . 46
2.4 Microstructure characterization . . . 47
2.5 Spherical nanoindentation measurements in Sinus mode (Ni at LEM3) . . . 48
2.5.1 Spherical indenter calibration . . . 49
Calibration of the indenter using the projected area of contact function . . . 50
Calibration of the indenter using Kalidindi's method . . . 51
2.5.2 Sinus mode measurements . . . 53
2.6 High speed nanoindentation mapping (Ni and IN718 at ICA) . . . 56
2.7 Conclusion . . . 58

Chapter 3 Numerical implementation of Vlassak & Nix model and applications **60**
3.1 Introduction . . . 60
3.2 Matrix Formalism . . . 61
3.3 Use of the Vlassak and Nix model for non-circular contact area . . . 63
3.4 Utilization of Gauss-Legendre Quadrature for Time Efficiency Enhancement . . . 64
3.5 Comparisons of Orientation Dependence of E^* and $E^{(hkl)}$ . . . 67
3.6 Case Studies and Model Validation . . . 69
3.6.1 The case of Cubic Elastic Symmetry . . . 70
3.6.2 Influence of Shear Moduli on E^* . . . 71

3.6.3 Dependence of E^* on A, $\nu_{\langle 100 \rangle}$ and $E_{\langle 100 \rangle}$ . . . 74
3.7 Conclusion . . . 77

Chapter 4 Bayesian Inference **78**

4.1 Introduction . . . 78
4.2 Integration of Vlassak and Nix Model with Bayesian Inference . . . 79
4.3 Bayesian Inference Workflow . . . 83
4.4 Theoretical study with artificial data . . . 85
4.5 Case study: Impact of A, $\nu_{\langle 100 \rangle}$ and $E_{\langle 100 \rangle}$ on the ratios of E^* . . . 90
4.6 Conclusion . . . 93

Chapter 5 Results & Discussion **95**

5.1 Introduction . . . 95
5.2 Pre-processing of Experimental Data . . . 96
5.3 Results from the correlative mechanical microscopy . . . 97
5.4 Results from Bayesian inference simulations . . . 100
5.4.1 High speed nanoindentation mapping (ICA) . . . 100
5.4.2 Ni Spherical (LEM3) . . . 107
5.5 Discussion . . . 110
5.6 Conclusion . . . 114

Conclusion **116**

Introduction

Estimating the elastic constants for materials is a real challenge, especially when it comes to multiphase materials. For single phase materials, scientist used techniques such as supersonic pulse echo (De Klerk *et al.*, 1955; Reynolds, 1952) or a combination of X-ray and thermal diffuse scattering (Vintaikin, 1966). For multiphase materials, these techniques, if used on their own, can only result in the macroscopic elastic constants of the materials (Fréour *et al.*, 2002) and can't single out a specific phase's elastic constants. Nanoindentation, also known as instrumented indentation testing, is an experimental technique used to measure the local response of materials in order to derive its local properties. Oliver et al. (Oliver *et al.*, 1992) first developed a global framework to obtain the local hardness as well as the local indentation modulus from nanoindentation experiments. Pathak et al. (Pathak *et al.*, 2015) took it further by developing a framework for spherical nanoindentation which permitted the accurate extraction of local stress-strain curves. This technique is useful in the case of anisotropic single-phase materials or multiphase materials. In the first case, we can accurately capture the anisotropy of said materials while in the second one, nanoindentation allows us, if the indenter is small enough, to single out the phases that interests us and derive its properties. Vlassak et al. (Vlassak *et al.*, 1993; Vlassak *et al.*, 1994) created a model that accurately predicted the indentation modulus for nanoindentation experiments for any indenter of circular contact area, as well as other indenters after applying a small correcting factor (~ 1.06 for a Berkovich indenter). Some claim that even though this model is accurate, it is very computationally expensive (Everaerts *et al.*, 2019; Seehaus *et al.*, 2023). But we will show that by using efficient integration techniques, this process can be accelerated (less than 1 second for a

given orientation). Scientists also tackled more complex problems such as estimating the elastic constants of a phase by using nanoindentation experiments. J. Everaerts et al. (Everaerts *et al.*, 2019) used the indentation modulus obtained as well as electron backscatter diffraction (EBSD) orientation data in order to do it. M. Mejri et al. (Mejri *et al.*, 2022) coupled it with the Density Functional Theory to achieve their goal. M. Seehaus (Seehaus *et al.*, 2023), on the other hand, used nanoindentation experiments and Vlassak and Nix's model and correlating it to EBSD data in order to obtain an "Indentation Based Stiffness Tensor". All the mentioned works permitted the estimation of a single set of elastic constants, and didn't take into account the variability of the experimental data that is needed to nuance the obtained constants. That's why Dr. Kalidindi's team (Castillo *et al.*, 2019; Venkatraman *et al.*, 2022) developed a framework in which nanoindentation experiments, finite element simulations (FEM), and Bayesian Inference came together in order to obtain the elastic constants of a phase while quantifying their uncertainties by keeping track of the means and standard deviations at each step. Bayesian inference integrates prior beliefs and information into the analysis and update those beliefs at every step while keeping track of the uncertainties. The protocol presented in this paper uses nanoindentation experiments, the Vlassak and Nix model, as well as Bayesian inference to statistically estimate the elastic constants the cubic materials/phases. As you will see, using Vlassak's model instead of FEM greatly decreases the time needed to converge into a solution. We will first present the experimental methodology, followed by a detailed technical description of Vlassak's model, cubic materials symmetry, and Bayesian Inference. Then we will present our findings and discuss them by comparing them to results obtained in the literature. High purity Nickel as well as Inconel 718 were chosen as showcase materials for this study. The elastic constants of Nickel are well documented, while Inconel 718 will be a chance for us to apply our protocol on a less known material. Spherical and Berkovic indenters were used for this study.

Chapter 1

Literature Review

1.1 Introduction

Characterizing the elastic properties of materials, particularly the single-crystal elastic constants (SECs), is a significant challenge in materials science, especially for multiphase polycrystalline aggregates. Elastic anisotropy, which refers to the variation in elastic properties depending on crystallographic orientation, plays a critical role in determining the mechanical behavior of materials. Traditionally, methods such as ultrasonic pulse echo and X-ray diffraction have been employed to estimate these constants for single-phase materials. However, these techniques struggle to isolate the elastic properties of individual phases in multiphase materials.

Nanoindentation, also known as instrumented indentation testing, has emerged as a powerful technique for measuring the local mechanical properties of materials. By applying a controlled force to an indenter and measuring the resulting displacement, or a controlled displacement and measuring the resulting force, nanoindentation can be used to extract key mechanical properties such as hardness and elastic modulus. The method has been particularly useful for studying the elastic anisotropy of single-phase materials, as well as multiphase materials where traditional macroscopic testing methods are insufficient. Recent advancements in the field, including the use of the micromechanical model of Vlassak and Nix (Vlassak *et al.*, 1993; Vlassak *et al.*, 1994; Vlassak *et al.*, 2003), have enabled more accurate predictions of the indentation modulus for materials with cubic symmetry, and have reduced the computational load traditionally associated with these

calculations.

A key focus of recent research has been the integration of nanoindentation with Bayesian inference, which allows for the incorporation of prior knowledge and the quantification of uncertainties in SEC estimations. By utilizing statistical approaches, it becomes possible to account for experimental variability and improve the robustness of the derived constants. This thesis builds upon these advancements, presenting a novel approach to estimating the elastic constants of cubic materials through a combination of nanoindentation experiments, application of the Vlassak and Nix model and Bayesian inference. High-purity nickel, a well-characterized material, is used to validate the methodology, while Inconel 718 serves as a more complex case study.

This chapter reviews the effects of elastic anisotropy on mechanical behavior, traditional methods for measuring elastic constants, and the emerging role of nanoindentation and Bayesian inference in characterizing single-crystal elastic constants. Through this review, we will establish the groundwork for the experimental procedures and numerical techniques presented in subsequent chapters.

1.2 Effects of elastic anisotropy on materials mechanical behavior

Generalized Hooke's law and cubic symmetry

Crystals are not intrinsically isotropic, at least not with respect to their elastic properties. Elastic anisotropy can be defined as the orientation dependence of the elastic moduli of the crystal and the velocity of sound through it. All known crystals are elastically anisotropic to some extent. The elastic properties of a crystal can be described either by the tensor of compliance constants S_{ijkl}, or by the tensor of elastic constants C_{ijkl} ($\boldsymbol{S}$ and $\boldsymbol{C}$ are tensors of order 4). The generalized Hooke's law elastic gives the linear relationship between strain and stress through the elastic constant tensor C_{ijkl}:

$$\sigma_{ij} = C_{ijkl}\varepsilon_{kl} \tag{1.1}$$

ε_{ij} and σ_{ij} being symmetric matrices, their representation can be reduced to a vector of dimension 6. The change of representation also applies to the matrix of elastic constants. The first pair of indices corresponds to the index of σ and the second pair corresponds to the index of ε:

$$\begin{array}{rcccccccc} & ij \text{ or } kl & 11 & 22 & 33 & 23,\ 32 & 31,\ 13 & 12,\ 21 & \\ C_{ijkl} \to C_{IJ} \text{ with } ij \to I \text{ and } kl \to J & & \downarrow & \downarrow & \downarrow & \downarrow & \downarrow & \downarrow & (1.2) \\ & I \text{ or } J & 1 & 2 & 3 & 4 & 5 & 6 & \end{array}$$

This is called Voigt's reduced notation. Using this reduced notation, Hooke's law can be written as follows:

$$\sigma = \begin{bmatrix} \sigma_1 \\ \sigma_2 \\ \sigma_3 \\ \sigma_4 \\ \sigma_5 \\ \sigma_6 \end{bmatrix} = \begin{bmatrix} C_{11} & C_{12} & C_{13} & C_{14} & C_{15} & C_{16} \\ C_{21} & C_{22} & C_{23} & C_{24} & C_{25} & C_{26} \\ C_{31} & C_{32} & C_{33} & C_{34} & C_{35} & C_{36} \\ C_{41} & C_{42} & C_{43} & C_{44} & C_{45} & C_{46} \\ C_{51} & C_{52} & C_{53} & C_{54} & C_{55} & C_{56} \\ C_{61} & C_{62} & C_{63} & C_{64} & C_{65} & C_{66} \end{bmatrix} \begin{bmatrix} \varepsilon_1 \\ \varepsilon_2 \\ \varepsilon_3 \\ \varepsilon_4 \\ \varepsilon_5 \\ \varepsilon_6 \end{bmatrix} \tag{1.3}$$

The matrix $\boldsymbol{C}$ is therefore a 6 x 6 matrix and it is a symmetric matrix (i.e. $C_{ij} = C_{ji}$). Thus, to describe the three-dimensional elastic behavior of a single crystal, 21 constants are needed. The greater the degree of symmetry of the crystal, the fewer constants are needed to describe its properties. For example, to calculate the elastic properties in isotropic crystals, which have the highest degree of symmetry, two constants λ and μ (called Lamé constants) are sufficient. For cubic crystals, 3 constants are required $C_{11},\ C_{12},\ C_{44}$, which are written in matrix form as:

$$\boldsymbol{C} = \begin{bmatrix} C_{11} & C_{12} & C_{12} & 0 & 0 & 0 \\ C_{12} & C_{11} & C_{12} & 0 & 0 & 0 \\ C_{12} & C_{12} & C_{11} & 0 & 0 & 0 \\ 0 & 0 & 0 & C_{44} & 0 & 0 \\ 0 & 0 & 0 & 0 & C_{44} & 0 \\ 0 & 0 & 0 & 0 & 0 & C_{44} \end{bmatrix} \tag{1.4}$$

Together, these three elastic constants can be used to quantify the anisotropy of any crystal of cubic symmetry. This anisotropy is calculated using what we call the anisotropy factor A (or Zener ratio) given by:

$$A = \frac{\mu''}{\mu'} = \frac{2C_{44}}{C_{11} - C_{12}} \tag{1.5}$$

A is defined as the ratio of $\mu'' = C_{44}$ over $\mu' = \frac{C_{11} - C_{12}}{2}$, the $\{001\}\langle 100\rangle$ and $\{001\}\langle 110\rangle$ shear resistances of the crystal (e.g., see deWit, 2008), respectively. $A = 1$ in the case of an isotropic material, and higher values of A indicates increasing anisotropy.

Elastic constant averages of a polycrystal with cubic symmetry

The elastic behavior of polycrystalline materials with cubic symmetry has been thoroughly examined during the first half of the 20th century. Voigt (Voigt, 1928), Reuss (Reuss *et al.*, 1929), and Hill (Hill, 1952) came up with the foundational models that provided us with essential insight into the relationship of the macroscopic elastic properties of polycrystalline aggregates and the properties of their individual crystals. The simplest model for calculating the elastic properties of a polycrystalline material is to take into account only the texture. This model, in which we ignore the interactions between grains, consists of performing an average over the space of crystallographic orientations, weighted by the orientation density function (ODF), of the elastic stiffnesses (Voigt, 1928) or of the elastic compliances (Reuss *et al.*, 1929). Voigt's model is an overestimation and offers an upper boundary to the elastic anisotropy of cubic materials, Reuss's model is underestimation and offers a lower boundary of the same elastic anisotropy, while Hill's model (Hill, 1952) bridges the gap between them by averaging their results and therefore provides a more accurate prediction. Despite their age, these three models remain the backbone of the elastic anisotropy for cubic materials.

Voigt's model was made under the assumption that strain is uniform throughout the whole polycrystalline material, meaning that every grain deforms in the same manner when the material is subjected to stress. It is used to estimate the upper bound of the elastic moduli as a maximum possible value. For a non-textured polycrystal with cubic symmetry (i.e. with isotropic elastic

properties), the effective shear modulus as per the Voigt model is given by:

$$G_V = \frac{2}{5}\mu^{'} + \frac{3}{5}\mu^{''} = \frac{C_{11} - C_{12} + 3C_{44}}{5} \tag{1.6}$$

Reuss's model, on the other hand, was made under the assumption that that stress is uniform throughout the polycrystalline aggregate, meaning the the stress is the same in every grain when the material is under an applied load. It provides a lower bound estimate of the elastic moduli as a minimum possible value. For a non-textured polycrystal with cubic symmetry, the effective shear modulus as per the Reuss model is given by:

$$\begin{aligned} \frac{5}{G_R} &= \frac{2}{5}\mu^{'} + \frac{3}{5}\mu^{''} \\ G_R &= \frac{5C_{44}(C_{11} - C_{12})}{3(C_{11} - C_{12}) + 4C_{44}} \end{aligned} \tag{1.7}$$

Besides, for the special case of a cubic polycrystal, the Voigt and Reuss averages lead to the same bulk modulus defined as:

$$K = \frac{C_{11} + 2C_{12}}{3} \tag{1.8}$$

For cubic symmetry only, it is noteworthy that this effective polycrystal bulk modulus K is also equal to the single crystal bulk modulus (deWit, 2008). Finally, the Hill average is defined as the arithmetic mean of the Voigt and Reuss averages (Hill, 1952; deWit, 2008):

$$G_{VRH} = \frac{1}{2}(G_V + G_R) \tag{1.9}$$

Hill's model is now extensively used to predict the elastic properties of polycrystalline aggregates as it uses both Voigt's and Reus's models to provide a more accurate estimate. Voigt, Reuss, and Hill have developped models that laid a robust foundation for understanding the isotropic elastic behavior of cubic materials. Besides providing upper and lower bounds, the latter also provides a more accurate average prediction.

Effect of elastic anisotropy on incompatibility stresses at grain boundaries

In polycrystals, the interactions between adjacent grains of different orientations which deform anisotropically give rise to incompatibility stresses. These incompatibility stresses add to the applied macroscopic stresses to satisfy strain compatibility at interfaces like grain boundaries.

J. Gemperlova et al. (Gemperlova *et al.*, 1989) are among the first to explore the calculation and effects of incompatibility stresses in bicrystals composed of two semi-infinite crystals, considering both elastic anisotropy and plastic deformation. Their study investigates various specific cases, particularly cubic bicrystals with (100) and (110) rotation axes, which are commonly used in experiments. The authors detail how grain boundaries influence mechanical properties through additional stresses induced by the requirement of strain compatibility at these boundaries. These incompatibility stresses are evaluated as functions of the grain boundary geometrical parameters and the orientation of the loading axis. It emphasizes that grain boundaries significantly affect the mechanical properties of polycrystalline materials. This effect stems from the crystalline elastic anisotropy and the anisotropy of plastic deformation of individual grains. The authors present a model for calculating these stresses in the form of a linear system to be resolved, accounting for elastic anisotropy due to crystal symmetry and various geometrical parameters that define the grain boundary type and loading direction. They have demonstrated that incompatibility stresses can activate secondary slip systems near grain boundaries, affecting the overall mechanical behavior of the bicrystal.

Similarly, T. Richeton and co-workers (Richeton *et al.*, 2013; Richeton *et al.*, 2015) have developped explicit analytical formulas of incompatibility stresses in an infinite bicrystal with a planar boundary made up of crystals I and II. The problem is equivalent to that of a 2-phase laminated material (see Fig. 1.1). The unit vector normal to the interface $\boldsymbol{n}$ is assumed to be oriented from crystal I to crystal II along the $\boldsymbol{e_2}$ direction. The volume fractions of crystals I and II are denoted f^I and f^{II} respectively. This bi-crystal or periodic laminate is assumed to have deformed under homogeneous loading in stress $\boldsymbol{\Sigma}$ and in temperature variation ΔT. The stresses in each crystal could be calculated analytically from the stress equilibrium and strain compatibility equations, and the assumptions of piecewise uniform plasticity and homogeneous temperature. They can be

written in the following explicit form:

$$\boldsymbol{\sigma^I} = \boldsymbol{\Sigma} + f^{II}\boldsymbol{G} : [\![\boldsymbol{\varepsilon^\star}]\!] \text{ and } \boldsymbol{\sigma^{II}} = \boldsymbol{\Sigma} - f^{I}\boldsymbol{G} : [\![\boldsymbol{\varepsilon^\star}]\!], \tag{1.10}$$

$$\text{with } [\![\boldsymbol{\varepsilon^\star}]\!] = [\![\boldsymbol{s}]\!] : \boldsymbol{\Sigma} + [\![\boldsymbol{\varepsilon^p}]\!] + [\![\boldsymbol{\alpha^T}]\!]\Delta T, \tag{1.11}$$

where $\boldsymbol{s}$ is the elastic compliance tensor, $\boldsymbol{\alpha^T}$ the thermal expansion tensor and $\boldsymbol{\varepsilon^p}$ the plastic strain tensor. The non-zero components of the symmetrical tensor $\boldsymbol{G}$ are given by:

$$\begin{aligned}
G_{11} &= \left(\tilde{s}_{35}^2 - \tilde{s}_{33}\tilde{s}_{55}\right)/D \ , \quad G_{13} = G_{31} = \left(\tilde{s}_{13}\tilde{s}_{55} - \tilde{s}_{15}\tilde{s}_{35}\right)/D \ , \\
G_{33} &= \left(\tilde{s}_{15}^2 - \tilde{s}_{11}\tilde{s}_{55}\right)/D \ , \quad G_{15} = G_{51} = \left(\tilde{s}_{15}\tilde{s}_{33} - \tilde{s}_{13}\tilde{s}_{35}\right)/D \ , \\
G_{55} &= \left(\tilde{s}_{13}^2 - \tilde{s}_{11}\tilde{s}_{33}\right)/D \ , \quad G_{35} = G_{53} = \left(\tilde{s}_{35}\tilde{s}_{11} - \tilde{s}_{13}\tilde{s}_{15}\right)/D \ ,
\end{aligned} \tag{1.12}$$

$$\text{with } D = \tilde{s}_{11}\tilde{s}_{35}^2 + \tilde{s}_{33}\tilde{s}_{15}^2 + \tilde{s}_{55}\tilde{s}_{13}^2 - \tilde{s}_{11}\tilde{s}_{33}\tilde{s}_{55} - 2\tilde{s}_{13}\tilde{s}_{15}\tilde{s}_{35}.$$

$$\text{and } \tilde{\boldsymbol{s}} = f^{II}\boldsymbol{s^I} + f^{I}\boldsymbol{s^{II}}, \tag{1.13}$$

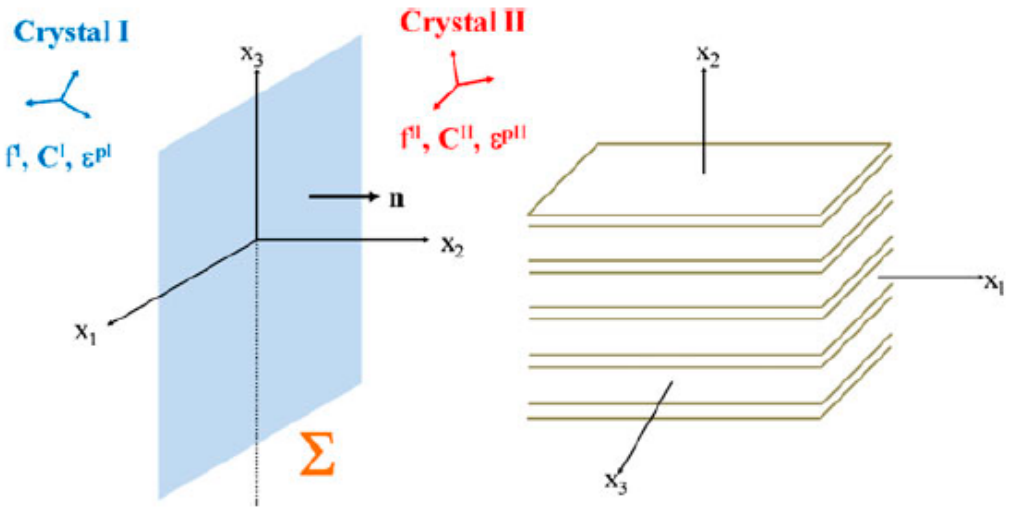

Figure 1.1: On the left: an infinite bicrystal with a planar boundary.
On the right: A periodic layered structure. From (Richeton *et al.*, 2015)

These formulas match those originally presented by Gemperlova et al. (Gemperlova *et al.*,

1989) in the form of a linear system with $f^I = f^{II}$ and without the thermal terms. They are also checked by finite element simulations (Richeton *et al.*, 2013) and used to study the onset of plasticity in a bi-crystalline Ni micropillar where the grain boundary plane is inclined with respect to the compression axis and the crystal volume fractions are non-equal (Tiba *et al.*, 2015, see Fig. 1.2). The experiment consists in stepwise microcompression tests with a flat punch nanoindenter to analyze the slip trace evolution in a SEM. The study compares the model's prediction with those obtained from the classic macroscopic Schmid's law, finding that the model based on incompatibility stresses aligns exactly with experimental observations regarding the most stressed crystal and active slip systems at the difference of the macroscopic Schmid's law. It is concluded that elastic anisotropy plays a crucial role in the activation of slip systems. The study also emphasizes the significant effects of crystal volume fraction and plasticity in neighboring crystals, while the grain boundary inclination has a limited impact.

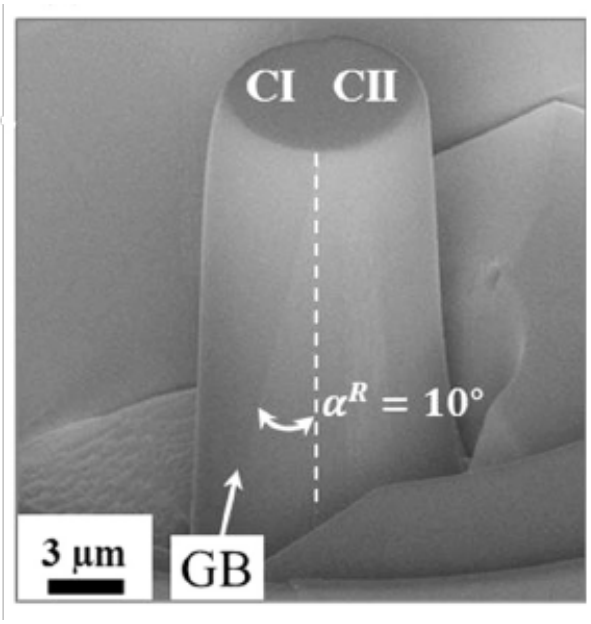

Figure 1.2: SEM picture of the BCMP showcasing the two crystals (CI and CII) as well as the grain boundary after FIB milling. From (Tiba *et al.*, 2015)

The effect of elastic anisotropy on the mechanical behavior of polycrystals can also be studied from mean-field models. As an example, S. Lhadi et al.(Lhadi *et al.*, 2018) investigate the elasto-viscoplastic behavior of near-β Titanium alloys using an advanced elasto-viscoplastic self-consistent (EVPSC) model. This work allows for a comprehensive analysis of the coupled effects of β-phase

elastic and plastic anisotropies on the local and overall mechanical responses. The authors utilize different sets of single-crystal elastic constants (SEC) from the literature that are associated to widely different Zener ratios (cf. Eq. 1.5) to model the elastic behavior and assess the impact of crystallographic texture and grain morphology during uniaxial and tension-compression tests.

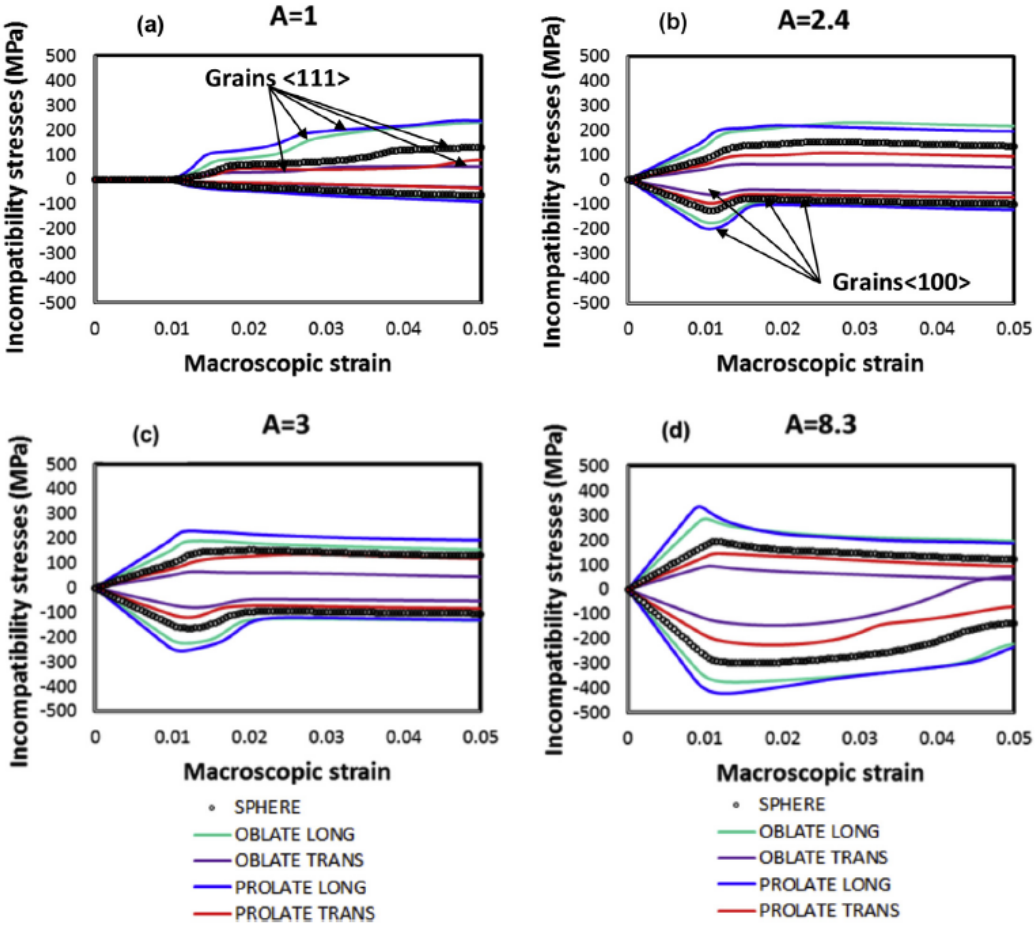

Figure 1.3: Incompatibility stresses in $<\ 100\ >$ and $<\ 111\ >$ oriented grains calculated for various grain geometries and anisotropy coefficients A, from (Lhadi *et al.*, 2018)

The results of the simulations indicate that while different SEC sets produce similar effective macroscopic responses, they lead to significantly varied local incompatibility stresses. The highest local incompatibility stresses are observed in $<\ 111\ >$ oriented grains at the end of the elastic regime during uniaxial tensile loading. The morphology of the β-grains, specifically their aspect ratios, is found to have a negligible effect on the overall mechanical response but a substantial influence on the local incompatibility stresses. The β-phase elastic anisotropy also significantly affects the yield surfaces of β-forged textured polycrystals, highlighting the complex interplay

between elastic and plastic anisotropies in determining the mechanical behavior of these materials. The EVPSC model proves efficient in capturing the nuanced effects of β-phase elastic anisotropy and grain morphology on the mechanical performance of these alloys.

In conclusion, these different studies underscore the importance of considering incompatibility stresses than can arise from elastic anisotropy when trying to predict the mechanical behavior of polycrystalline materials. In turn, they highlight the need to be able to measure accurately the single-crystal elastic constants (SEC) in order to well-predict the polycrystal's behavior.

1.3 Measurement of single-crystal elastic constants by traditional methods

Estimating the single crystal elastic constants (SEC) of crystalline materials poses significant challenges, particularly for multiphase polycrystalline materials. Traditional methods for characterizing SEC involve experiments on large single crystals using classical techniques such as ultrasonic wave velocities or supersonic pulse echo.

Ultrasonic waves

Mc Skimin (McSkimin, 1953) demonstrated that the speed of ultrasonic waves traveling through a material is directly related to its elastic properties. By analyzing wave velocities in different crystallographic directions, he was able to determine the complete set of elastic constants for a crystal (Fig. 1.4). The accuracy and reliability of ultrasonic wave velocity measurements have made them a preferred method in many research and industrial applications at the time. However, the application of these classical methods to polycrystalline materials presents significant challenges. Polycrystalline materials lack the large single crystals required for direct ultrasonic measurements, necessitating the development of alternative approaches. Additionally, the presence of multiple phases in polycrystalline materials complicates the estimation of SEC, as interactions between different phases must be considered. These challenges have driven the development of inverse approaches and advanced micromechanical models to accurately estimate SEC in polycrystalline

materials.

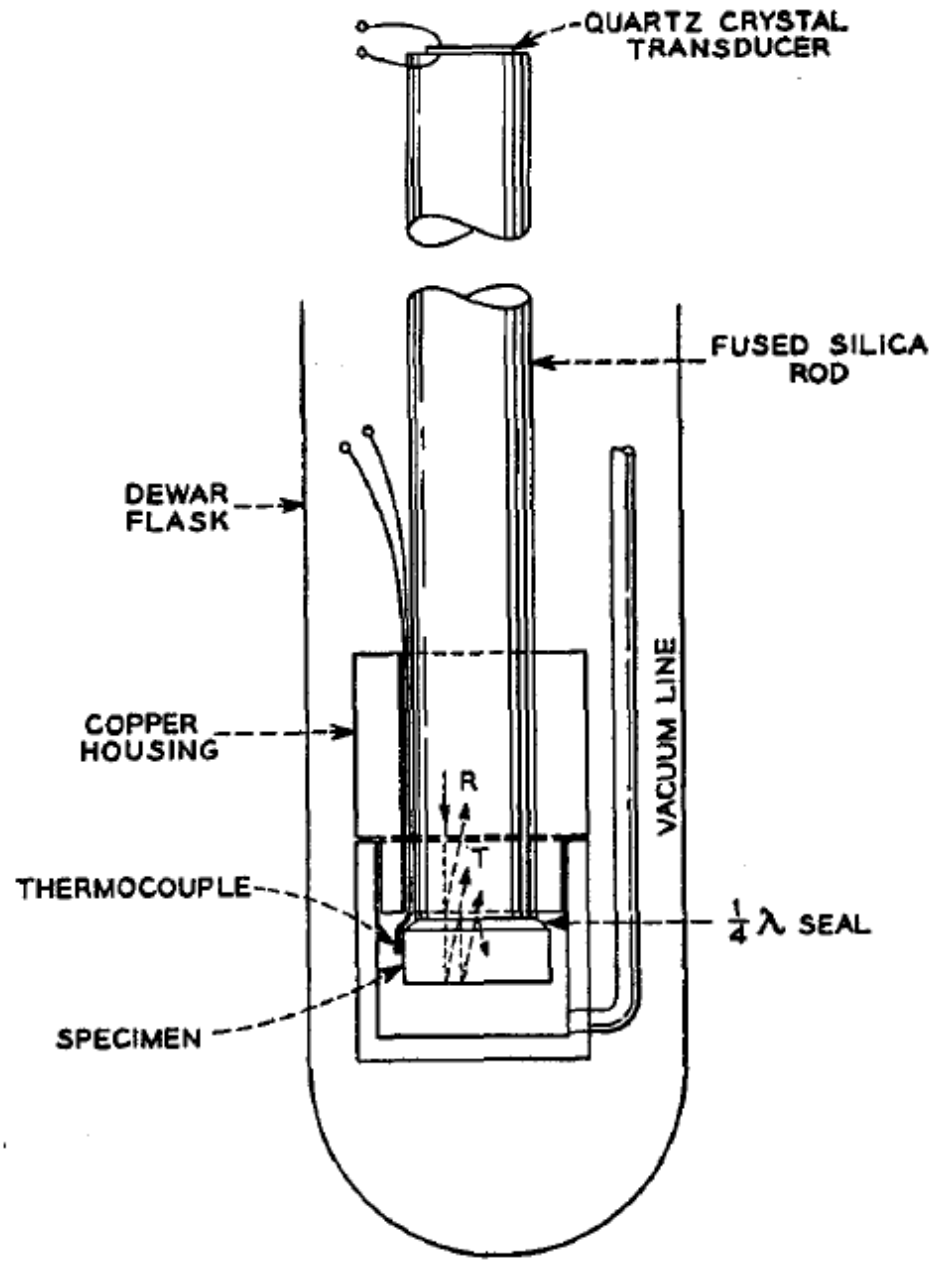

Figure 1.4: Apparatus used to measure elastic constants using ultrasonic waves. From (McSkimin, 1953)

Supersonic pulse echo

J. De Klerk et al. (De Klerk *et al.*, 1955) used a technique called the supersonic pulse echo method (Fig. 1.5), which significantly improved the accuracy of measuring elastic constants. This technique involves using high-frequency sound pulses that reflect within the crystal, with the time

delay between these echoes being used to calculate the elastic constants. The pulse echo method allowed for more precise measurements by reducing the uncertainties associated with wave travel paths, which was a limitation in earlier techniques.

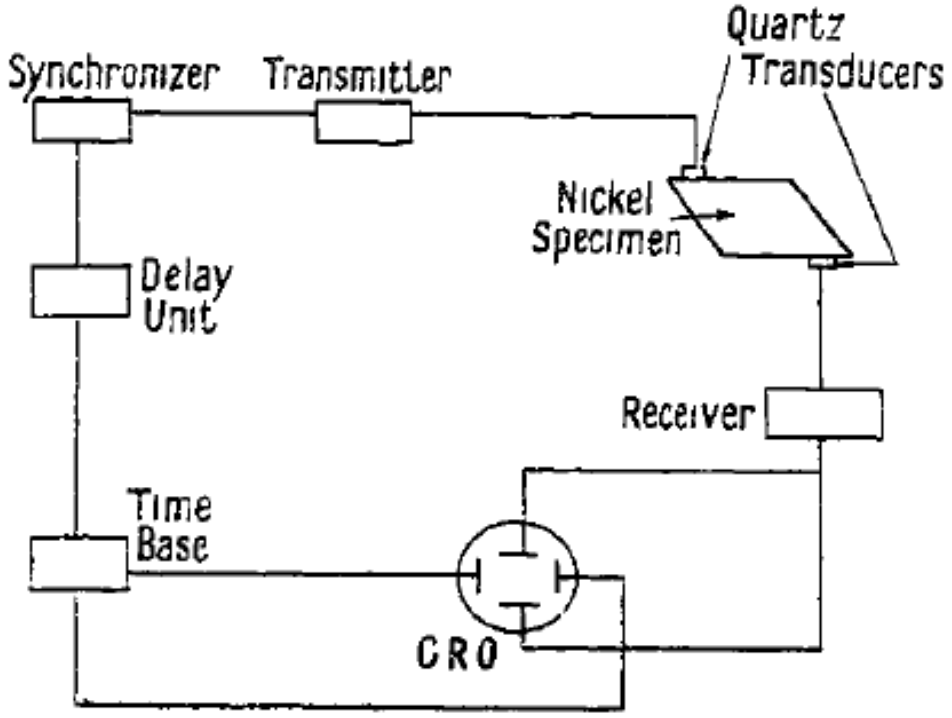

Figure 1.5: Block diagram of the apparatus used to measure elastic constants using supersonic pulse echo. From (De Klerk *et al.*, 1955)

The pulse echo method proved particularly useful for materials where large single crystals could be obtained, offering a robust mean of determining the SEC with greater precision. The ability to obtain high-resolution data on the elastic properties of single crystals made this method a valuable tool in material science research. It provided insights into the intrinsic properties of materials, contributing to the understanding of their mechanical behavior under different conditions. However, despite its advantages, the pulse echo method also faces limitations when applied to polycrystalline materials.

First obstacle: Single-phase polycrystalline materials

For single-phase polycrystalline materials, direct measurement techniques are often not feasible due to the lack of large single crystals. Instead, inverse approaches are employed, relying on

micromechanical models to identify SEC from macroscopic elastic constants. These approaches use the overall elastic response of the polycrystalline material to back-calculate the SEC, leveraging the relationship between microstructural properties and macroscopic behavior.

S. Matthies et al. (Matthies *et al.*, 2001) utilized diffraction data to derive the elastic constants of polycrystalline materials. By analyzing diffraction patterns, they applied the self-consistent model to back-calculate the single crystal elastic constants from the measured macroscopic elastic properties of the polycrystalline aggregate. This method provided a viable solution for estimating SEC in cases where direct measurements were not possible.

J.R. Cho et al. (Cho *et al.*, 2002) used the same diffraction technique but incorporated additional micromechanical models to better handle complex materials. Cho's work not only included the use of the elastic self-consistent model and diffraction data, but also introduced corrections for texture and anisotropy effects. These advancements significantly improved the accuracy of the SEC estimates for various polycrystalline materials, making the inverse approach more reliable and widely applicable. Their work demonstrated the importance of considering material texture and anisotropy.

Later, D. Delbergue et al. (Delbergue *et al.*, 2019) integrated advanced diffraction methods and computational models to the inverse approach. They employed high-resolution neutron diffraction to gather detailed strain data, which was then used in conjunction with improved micromechanical models to derive SEC with higher precision. By obtaining high-resolution strain data, they were able to achieve a more detailed understanding of the material's elastic response. This data, combined with their micromechanical models, allowed for more accurate SEC estimations. These models allowed for the simulation of material behavior under various conditions, providing insights that were not easily obtainable through experiments alone. The integration of these techniques provided a comprehensive framework for understanding the elastic properties of complex materials.

Second obstacle: Multiphase polycrystalline materials

Estimating SECs becomes even more complicated when dealing with multiphase polycrystalline materials. Producing single crystals with the exact chemical composition as a specific phase within

a multiphase alloy is often impractical, if not impossible. Furthermore, inverse approaches for these materials require the development of more sophisticated micromechanical models to account for phase interactions. These interactions can significantly influence the overall elastic behavior of the material, necessitating the consideration of multiple factors in the estimation process.

S. Fréour et al.'s (Fréour *et al.*, 2002; Fréour *et al.*, 2005) developed micromechanical models that incorporated phase interaction effects. Their models accounted for the effects of different phases on the overall elastic behavior of multiphase polycrystalline materials, which is essential for accurately estimating SEC in materials with complex microstructures. By considering phase interactions, their models provided a more realistic representation of the material's behavior, enhancing the accuracy of SEC estimations.

S.L. Raghunathan et al. (Raghunathan *et al.*, 2007) introduced additional parameters into the micromechanical models to better simulate the behavior of real-world materials. This included considerations for grain boundary effects and the interaction between different crystalline phases under various loading conditions. Their models provided a more comprehensive framework for estimating SEC in multiphase materials, addressing some of the limitations of earlier models and offering more accurate predictions of material behavior under complex conditions.

1.4 Characterization by nanoindentation

Nanoindentation is a relatively recent technique used to measure the mechanical properties of materials at the micro and nano scales. It involves pressing a hard, sharp indenter into the surface of a material and measuring the resulting indentation load-displacement curve to extract properties such as the hardness and the elastic modulus.

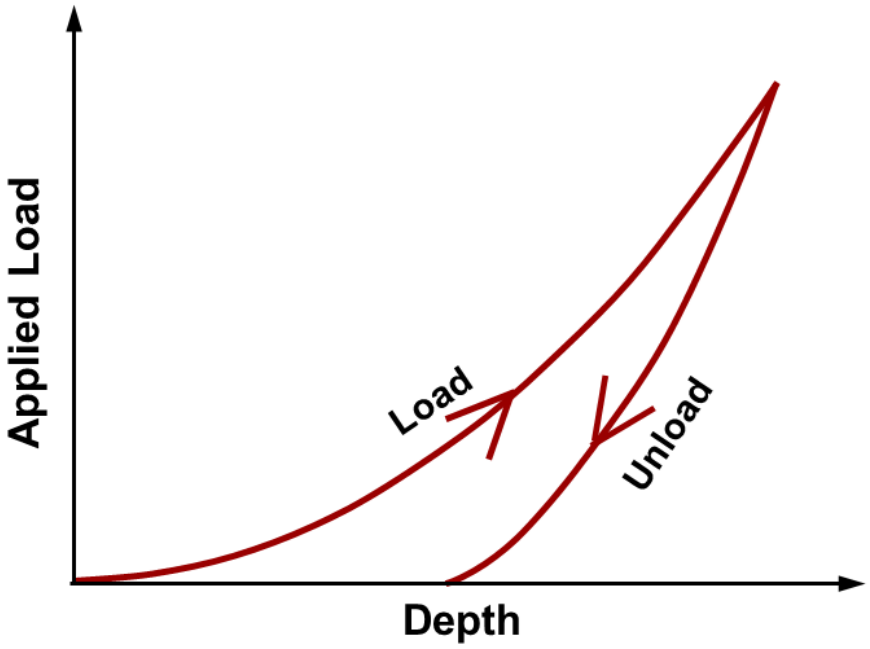

Figure 1.6: Typical Nanoindentation Curve Showcasing The Loading And Unloading Parts

The development and refinement of nanoindentation protocols that are going to be presented next have significantly improved the accuracy and reliability of these measurements. Each of these protocols offers distinct advantages and disadvantages, making them suitable for different applications. Accurate calibration of the contact radius against the contact depth is also going to be discussed as it is essential for precise measurements, and various methods are employed to achieve this.

1.4.1 Nanoindentation protocols

Method of Oliver & Pharr

Oliver & Pharr (Oliver *et al.*, 1992; Oliver *et al.*, 2004) have developped a nanoindentation protocol to extract the material's properties from the unloading part of nanoindentation Force-Depth curves. Their protocol is, to this day, the most popular protocol for analyzing nanoindentation curves. Up until then, a popular belief in the community was that the unloading part of the curve was linear (Doerner *et al.*, 1986). Oliver & Pharr realized that it was almost never linear and that the

unloading curve rather followed a power law:

$$F = \alpha \left(h - h_f\right)^m \tag{1.14}$$

where F is the force applied on the material's surface, h is the indentation depth, h_f is the residual depth of the indentation imprint (see figure 1.8), and α and m are fitting constants. m falls in the range $1.2 \leq m \leq 1.6$ depending on the indenter's shape (i.e.: $m = 1$ for a flat punch indenter, $m = 1.5$ for a paraboloid of revolution such as a spherical indenter, and $m = 2$ for conical indenters).

In their study, Oliver & Phar have defined three fundamental depths : h_m the maximum indentation depth, h_c the contact depth, and h_s the sink in depth:

$$h_m = h_c + h_s \tag{1.15}$$

$$h_s = \varepsilon \frac{F_m}{S} \tag{1.16}$$

$$h_c = h_m - \varepsilon \frac{F_m}{S} \tag{1.17}$$

where ε is a constant ($\varepsilon = 1$ for a flat punch, $\varepsilon = 0.75$ for a paraboloid of revolution, and $\varepsilon = 0.72$ for conical indenters), F_m is the maximum force of indentation, and S is the contact stiffness that can be calculated as the slope of the initial part of the unloading curve assuming that only the elastic part of the deformation is recovered during the unloading. These depths are illustrated in figure 1.7:

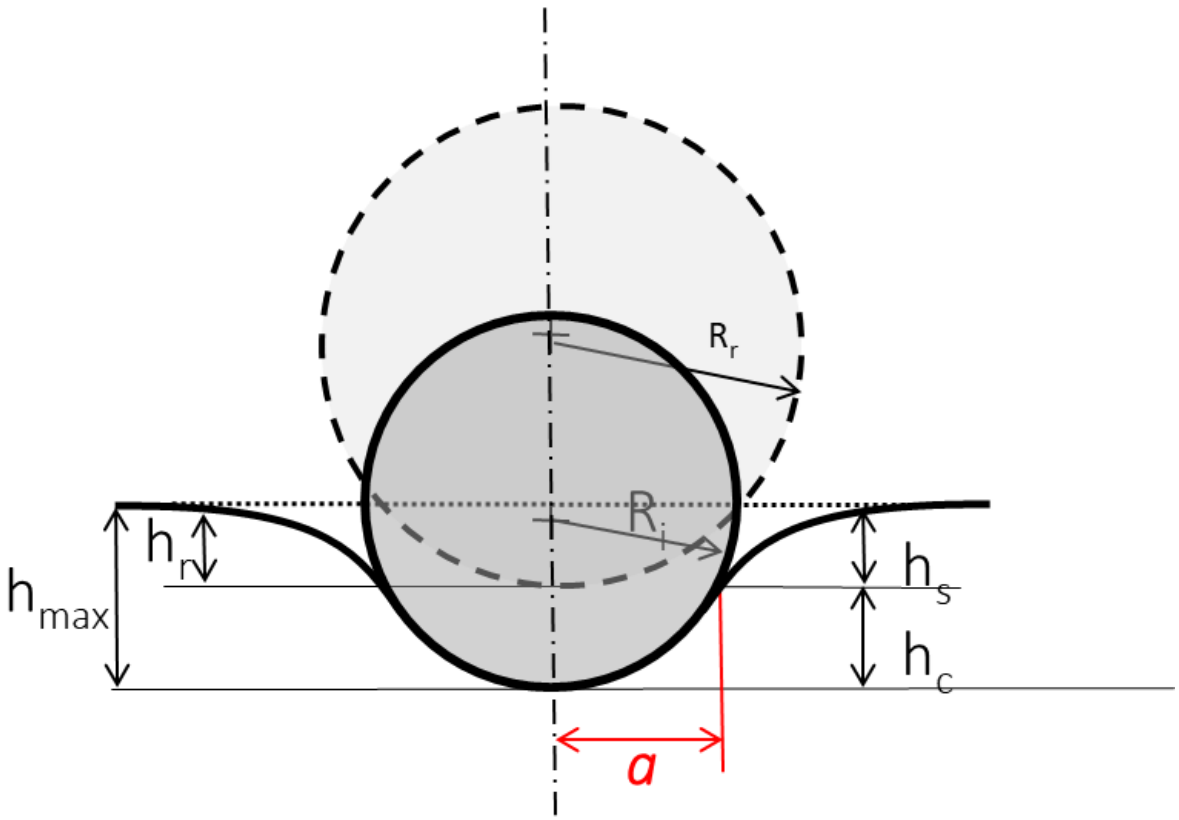

Figure 1.7: Schematic of Indentation Parameters Illustrating Maximum Indentation Depth h_m, Residual Depth h_r, Contact Depth h_c, and Contact Radius a

S is actually obtained by fitting the parameters α and m from the unloading curve according to Eq. 1.14 between 40% and 98% of F_m and then by making an analytical derivation of this expression:

$$S = \frac{dF}{dh}_{h=h_m} = m\alpha \left(h_m - h_f\right)^{m-1} \tag{1.18}$$

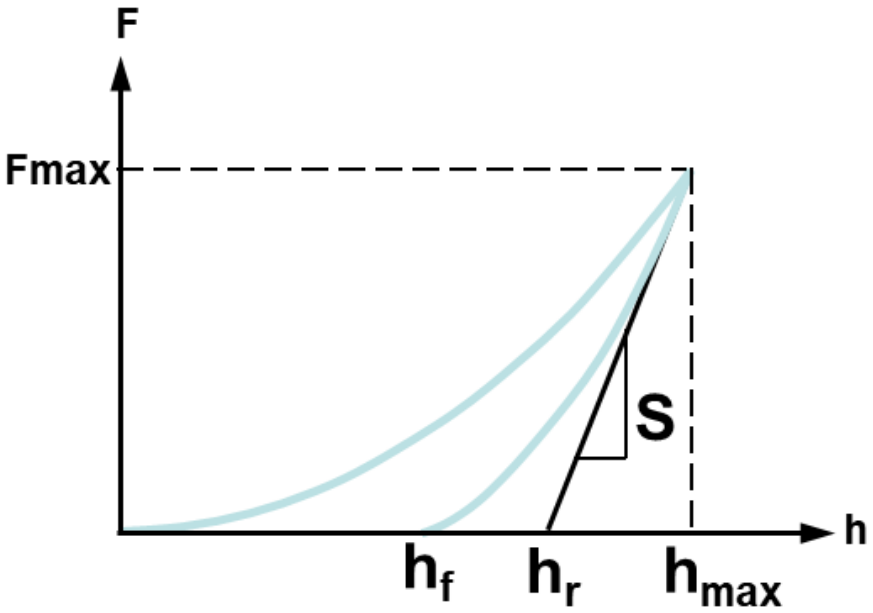

Figure 1.8: Indentation Load-Depth curve illustrating the experimental stiffness calculation (S=$\frac{dF}{dh}$), as well as the fundamental depths.

The effective modulus E_{eff} (or reduced modulus E_r as denoted in the papers of Oliver & Pharr (Oliver *et al.*, 1992; Oliver *et al.*, 2004)) is then calculated as (Sneddon, 1965):

$$E_{eff} = \frac{1}{\beta}\frac{\sqrt{\pi}}{2}\frac{S}{\sqrt{A_p}} \tag{1.19}$$

This equation is valid for any indentation that falls in the elastic and elastic-plastic contact. A_p is the projected area of contact under the indenter and is calibrated as a function of h_c, and β is a constant that was first introduced by King (King, 1987) to account for the indenter's shape. According to King, this constant is for example equal to 1 in the case of an axisymmetric indenter (such as a spherical indenter or a flat punch), and 1.034 for a Berkovich indenter.

Method of Field & Swain

Oliver & Pharr's protocol involved a singular loading and unloading of the sample and therefore was only able to extract one set of properties per experiment at one depth, which is the maximum indentation depth h_m. Field & Swain (Field *et al.*, 1993; Field *et al.*, 1995) recognized the oppor-

tunity and developed a spherical nanoindentation protocol consisting of partial unloading cycles to 50% of the cycle's maximum force. Their protocol used Hertz's theory (Hertz, 1896) to analyze each unloading segment. Not only did this protocol achieve the measurement of the material properties at different depths using only one experiment, it was also able to distinguish the transition from the purely elastic regime (at low forces) into the elastic-plastic regime (at higher forces). To be able to use Hertz theory, they assumed that the contact radius between the indenter and the sample's surface is smaller than the indenter's radius.

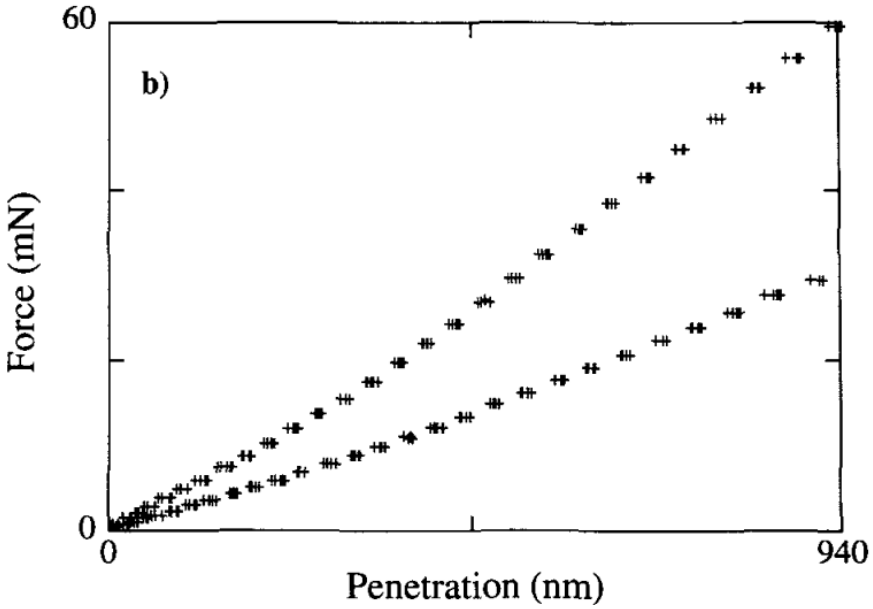

Figure 1.9: The multiple partial unloadings from Field & Swain's experimental procedure. From(Field *et al.*, 1995)

For a friction-less and elastic contact between two isotropic and axisymmetric surfaces, the indentation load can be described by (Hertz, 1896):

$$F_m = \frac{4}{3} E_{eff} \sqrt{R h_e^3} \tag{1.20}$$

where h_e is the elastic indentation depth given by:

$$h_e = h_m - h_f \tag{1.21}$$

F_m and h_m are not the experiment's maximum force and depth, but rather the cycle of interest's maximum force and depth. The spherical radius of contact a can be defined geometrically as a function of the contact depth h_c and the indenter's radius R_i (Fischer-Cripps *et al.*, 2004):

$$a = \sqrt{2R_i h_c - h_c^2} \tag{1.22}$$

Then, from the expression of the deflection of the original free surface, it can be easily shown that the contact depth is half of the total elastic displacement for a spherical indenter (Fischer-Cripps *et al.*, 2004):

$$h_c = \frac{h_e}{2} \tag{1.23}$$

Equation 1.20 can be rewritten as:

$$E_{eff} = \frac{3}{4}\frac{F_m}{a h_e} = \frac{3}{4}\frac{F_m}{a(h_m - h_f)} \tag{1.24}$$

Since h_c (and therefore h_f) cannot be measured experimentally using their multiple unloading approach, they proposed an analytical approach. By considering two points (F_m, h_m) and (F_s, h_s) on a cycle's unloading between which the deformation is supposed to be fully elastic, the ratio of Equation 1.20 applied to both these points allows us to deduce h_f for that cycle:

$$\frac{h_m - h_f}{h_s - h_f} = \left(\frac{F_m}{F_s}\right)^{\frac{2}{3}} \tag{1.25}$$

$$h_f = \frac{h_s \left(\frac{F_m}{F_s}\right)^{\frac{2}{3}} - h_m}{\left(\frac{F_m}{F_s}\right)^{\frac{2}{3}} - 1} \tag{1.26}$$

The first limitation of this method is that it only applies to spherical indenters. In addition, its use of Hertz theory to analyze the unloading segments by neglecting the assumption that the indentation depth has to be way smaller than the contact radius a. However, at high indentation

depths, this is no longer the case and the obtained properties at these depths are no longer accurate.

Continuous Stiffness Measurement (CSM)

Before moving to the next protocol, let's highlight a significant advancement in nanoindentation data acquisition that is Continuous Stiffness Measurement (CSM). It is a novel indentation mode that provides continuous data on material properties such as hardness and elastic modulus during the indentation process. Unlike traditional methods where measurements are made at discrete points, CSM allows for real-time data acquisition as the indenter penetrates the material. This method involves superimposing a small, oscillating load on the primary indentation load, enabling the continuous calculation of mechanical properties as a function of depth. Moreover, CSM addresses the limitations of traditional nanoindentation by minimizing errors related to thermal drift and ensuring that data is captured throughout the entire indentation process. This continuous feedback loop between load application and measurement ensures a high resolution of the material's mechanical properties across different depths, making CSM a powerful tool in the characterization of advanced materials, including thin films, coatings, and small volumes of material where traditional methods may not provide sufficient detail.

Method of Pathak & Kalidindi

Nanoindentation has evolved as a powerful technique for mechanical characterization at small scales. The Kalidindi's indentation protocol, a significant development in this field, has leveraged advancements in nanoindentation hardware to provide detailed and reliable mechanical properties of materials. It addresses several challenges in mechanical characterization through nanoindentation. The protocol utilizes the Hertzian theory of contact to extract indentation stress-strain curves, capturing both elastic and elastic-plastic responses of materials across various scales. This method stands out by producing consistent and reproducible measurements.

A critical aspect of the Kalidindi protocol (Kalidindi *et al.*, 2008; Pathak *et al.*, 2015) is its handling of the initial contact point in nanoindentation tests. The protocol employs a zero-point

correction to accurately determine the load-displacement segment corresponding to purely elastic deformation (see Fig. 1.10). This correction mitigates errors caused by surface roughness and oxide layers, which can lead to deviations in the initial segment of the curve and erroneous elastic property values. This is also important for a better estimation of the contact radius along the nanoindentation experiment, leading to robust and consistent results.

Recent advances in nanoindentation hardware have significantly enhanced the implementation and accuracy of the Kalidindi's protocol. Modern nanoindenters are equipped with Continuous Stiffness Measurement (CSM) capabilities. CSM superimposes high-rate sinusoidal loading-unloading cycles during indentation, allowing for real-time measurement of stiffness and continuous assessment of the contact area. This technology eliminates the need for manual unloading segments, streamlining the data acquisition process and improving the fidelity of the stress-strain curves obtained.

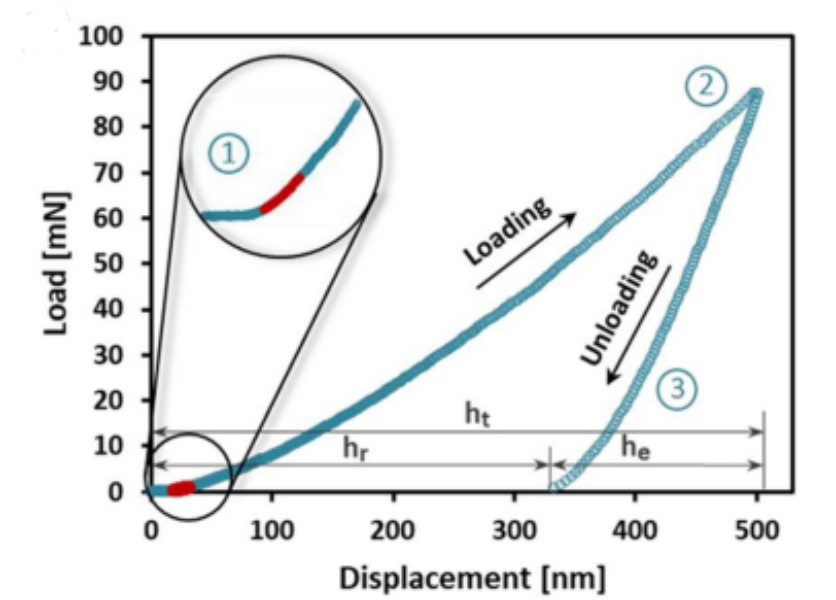

Figure 1.10: Experimental CSM indentation Load-Depth curve showcasing the initial elastic segment. From (Millan-Espitia *et al.*, 2021)

The protocol begins with the application of the Hertz's theory (Hertz, 1896) for frictionless contact between two isotropic elastic solids. For spherical indentation, the Hertz contact equations describe the relationship between the indentation load F and the elastic indentation depth h_e as well as the relationship between the contact radius a and h_e as follows:

$$F = \frac{4}{3} E_{eff} {R_{eff}}^{1/2} {h_e}^{3/2} \tag{1.27}$$

$$a = \sqrt{R_{eff} h_e} \tag{1.28}$$

R_{eff} is the effective radius of the indenter and sample's surface given by:

$$\frac{1}{R_{eff}} = \frac{1}{R_s} + \frac{1}{R_i} \tag{1.29}$$

where R_i and R_s denote the indenter's and surface radii, respectively. The effective modulus satisfies the following general relation for an isotropic elastic material:

$$\frac{1}{E_{eff}} = \frac{1 - \nu_s^2}{E_s} + \frac{1 - \nu_i^2}{E_i} \tag{1.30}$$

Here, E_s is the isotropic Young modulus of the sample, ν_s the sample Poisson's ratio while ν_i and E_i are the Poisson's ratio and the Young modulus of the isotropic indenter, respectively. Besides, for a spherical indenter, $\beta = 1$ in the equation of the effective modulus (Eq. 1.19) and the contact depth can be estimated as $A_p = \pi a^2$, so that the following relation holds at each cycle in the CSM mode:

$$E_{eff} = \frac{S}{2a} \tag{1.31}$$

The zero-point correction identifies an effective point for the initial contact other than the one usually detected by the machine and from which the nanoindentation curve follows Hertzian mechanics of contact. For spherical nanoindentation this relationship can be written as:

$$S = \frac{dF}{dh_e} = \frac{3F}{2h_e} = \frac{3(\tilde{F} - F^*)}{2(\tilde{h_e} - h^*)} \tag{1.32}$$

where S is the continuously measured stiffness in CSM mode, $\tilde{F}$ and $\tilde{h_e}$ are the measured indentation load and depth, and F^* and h^* are the zero-points corrections to the measured indentation load and depth. Eq. 1.32 can be rearranged as:

$$\tilde{F} - \frac{2}{3}S\tilde{h_e} = F^* - \frac{2}{3}S\tilde{h^*} \tag{1.33}$$

Hence, by plotting $\tilde{F} - \frac{2}{3}S\tilde{h_e}$ as a function of S in the elastic regime, the values of F^* and h^* can be deduced from a simple linear regression of the experimental data.

Next, Hertz's theory can be recast into a linear relationship in order to build an indentation stress-strain curve:

$$\sigma_{ind} = \frac{F}{\pi a^2} = E_{eff}\varepsilon_{ind} \tag{1.34}$$

where σ_{ind} and ε_{ind} are defined as the indentation stress and indentation strain, respectively. The contact radius a is needed to estimate the indentation stress and can be obtained through Eq.1.22. The expression of the indentation strain is then deduced from Eqs.1.27, 1.28 and 1.34 as:

$$\varepsilon_{ind} = \frac{4}{3\pi}\frac{h_e}{a} \approx \frac{h_e}{2.4a} \tag{1.35}$$

These definitions of indentation stress and indentation elastic strain can be interpreted as seeing the indentation test as equivalent to the compression of a cylinder of radius a and height $2.4a$, which corresponds roughly to the primary deformation zone in a spherical indentation test.

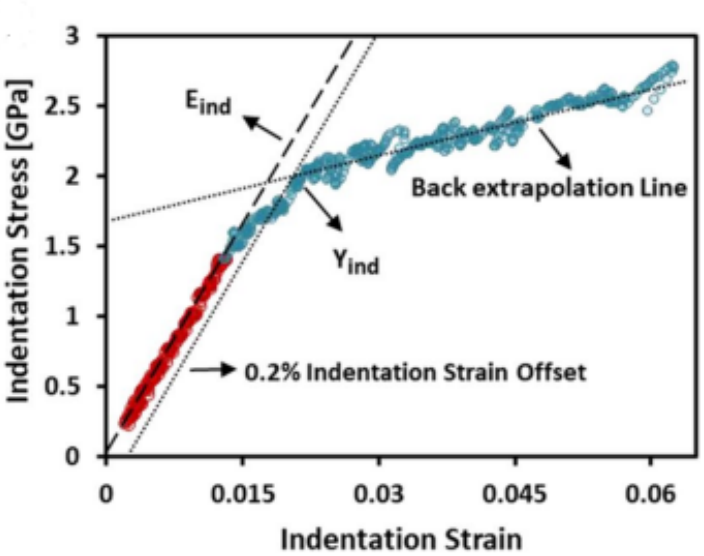

Figure 1.11: Experimental indentation stress strain curve obtained from processing the experimental curve in Figure 1.10. From (Millan-Espitia *et al.*, 2021)

This protocol allows then to identify the transition between the purely elastic regime and the elastic-plastic regime. From this transition, it is accordingly possible to estimate the yield stress σ_Y which is the indentation stress at 0.2% offset plastic strain (see Fig. 1.11).

The Kalidindi's indentation protocol, enhanced by advancements in nanoindentation hardware, represents a significant advancement in the field of mechanical characterization. The protocol has a systematic approach to handling initial contact. It does not only improves the accuracy and repeatability of mechanical property measurements but also broadens the scope of nanoindentation applications in materials research.

1.4.2 Analytical methods to calculate the anisotropic modulus E^*

For an elastically anisotropic material, the effective modulus E_{eff} is a combination of the indenter's and indented surface's properties according to the following relationship (Timoshenko *et al.*, 1951):

$$\frac{1}{E_{eff}} = \frac{1}{E^*} + \frac{1-\nu_i^2}{E_i} \tag{1.36}$$

where E^* is denoted hereafter the anisotropic indentation modulus. We will now explore the analytical methods developed to calculate the anisotropic modulus E^*, focusing on the challenges posed by the material's anisotropy. Several researchers have endeavored to derive these relationships through various theoretical approaches, each aiming to accurately capture the material's inherent anisotropic characteristics. In the following section, we will delve into two analytical methods, discussing their theoretical foundations and implications for predicting E^* in anisotropic materials.

Substituting E^* with the directional Young's modulus $E^{(hkl)}$

Some authors (e.g., Kang *et al.*, 2012; Everaerts *et al.*, 2019; Mejri *et al.*, 2022; Seehaus *et al.*, 2023) have chosen the option to replace directly the anisotropic modulus E^* in Eq.1.36 or the isotropic Young modulus E_S in Eq.1.30 by the grain's directional Young's modulus $E^{(hkl)}$ that can

be expressed as a function of the direction $\boldsymbol{n}$ as follows (Cazzani *et al.*, 2003):

$$\frac{1}{E^{(hkl)}(\boldsymbol{n})} = S_{ijkl} n_i n_j n_k n_l \tag{1.37}$$

where S_{ijkl} denotes the fourth-rank compliance tensor ($S_{ijkl} = {C_{ijkl}}^{-1}$) and $\boldsymbol{n}$ is a unit-vector. For cubic symmetry materials, $E^{(hkl)}$ can also be computed from the classical formula:

$$E^{(hkl)} = \frac{1}{S_{11} + (2S_{12} - 2S_{11} + S_{44})A^{(hkl)}} \tag{1.38}$$

with:

$$A^{(hkl)} = \frac{h^2k^2 + k^2l^2 + l^2h^2}{(h^2 + k^2 + l^2)^2} \tag{1.39}$$

where h, k, and l are Miller's indices. However, this approach overlooks the anisotropic effects arising from the multiaxial mechanical loading conditions inherent to nanoindentation testing. Indeed, a nanoindentation test is not uniaxial but enforces complex multiaxial stress/strain fields beneath the tip, even in elasticity (Gerberich *et al.*, 1996; Li *et al.*, 2011; Caer *et al.*, 2013; Habiyaremye *et al.*, 2024). Such an approach ignores thus the contributions from other directions than the indentation direction. Therefore, $E^{(hkl)}$, being specific to an uniaxial test, fails to account for the full range of anisotropic effects. Because of the multiaxiality of the nanoindentation test, the anisotropy displayed by E^* is actually much more reduced than the anisotropy of the directional Young's modulus $E^{(hkl)}$. As a matter of fact, for Ni, $E^{(hkl)}$ can double from one orientation to the other while E^* varies at most by 10% (Li *et al.*, 2011).

Vlassak and Nix's micromechanical model

Vlassak and Nix (Vlassak *et al.*, 1993; Vlassak *et al.*, 1994; Vlassak *et al.*, 2003) developed a semi-analytical micromechanical model which can evaluate E^* for a given crystallographic orientation and a set of elastic constants. In their model, it is assumed that the indenter geometry corresponds to a circular flat punch and that the pressure distribution under this flat punch follows the same distribution as the one of an isotropic material given by Sneddon (Sneddon, 1965; Vlassak *et al.*, 1993). Then, using the surface Green's function derived by Barnett and Lothe (Barnett *et al.*,

1975) within the Stroh formalism (Stroh, 1958), which provides the displacement to a unit point load applied perpendicular to the boundary of a half space, Vlassak and Nix (Vlassak *et al.*, 1993; Vlassak *et al.*, 1994; Vlassak *et al.*, 2003) have shown that E^* can be evaluated as:

$$E^* = 4\pi \left(\int_0^{2\pi} n_i B_{ij}^{-1}(\omega) n_j \, d\omega \right)^{-1} \tag{1.40}$$

where $\boldsymbol{n}$ is the unit normal to the indentation surface in the crystal's coordinate system which is related to the Euler angles of a given orientation. $\boldsymbol{B}$ is a symmetric matrix that depends on the anisotropic elastic tensor $\boldsymbol{C}$. $\boldsymbol{B}$ was originally expressed as a line integral within the Stroh integral formalism (Vlassak *et al.*, 1993; Vlassak *et al.*, 1994; Vlassak *et al.*, 2003):

$$B_{ij} = \frac{1}{2\pi} \int_0^{2\pi} \left((mm)_{ij} - (mn)_{ik} (nn)_{kp}^{-1} (nm)_{pj} \right) \, d\omega \tag{1.41}$$

where the tensor $\boldsymbol{C}$ is included in the notation $(mn)_{jk} = m_i C_{ijkl} n_l$. The vector $\boldsymbol{m}$ is obtained as $\boldsymbol{m} = \boldsymbol{n} \wedge \boldsymbol{t}$ where $\boldsymbol{t}$ is an arbitrary unit vector in the plane perpendicular to $\boldsymbol{n}$. It makes an angle ω with a fixed datum of the plane perpendicular to $\boldsymbol{n}$. ω corresponds to the angle that varies from 0 to 2π in the line integral of Eq. 1.40.

Unlike the previous method that relied solely on replacing E^* by $E^{(hkl)}$, the Vlassak and Nix micromechanical model is designed to account for the anisotropic nature of materials and the complex loading conditions under the indenter leading to a more accurate representation of the obtained E^* modulus. This model can be implemented numerically as in (Li *et al.*, 2011; Aspinall *et al.*, 2022) for instance and done in the present thesis for cubic and transversely anisotropic materials (see further Chapter 3).

In order to avoid a complex numerical implementation, Vlassak and Nix (Vlassak *et al.*, 1994) also provided an empirical equation to estimate E^* for solids with cubic crystal symmetry directly from the isotropic Young's modulus E_s and Poisson's ratio ν_s of the specimen:

$$E^* = \beta^{(hkl)} \left(\frac{E_s}{1 - \nu_s} \right)_{isotropic} \tag{1.42}$$

where the coefficient $\beta^{(hkl)}$ writes:

$$\beta^{(hkl)} = a + c\,(A - A_0)^B \tag{1.43}$$

A denotes the Zener ratio or elastic anisotropy coefficient for cubic crystals:

$$A = \frac{2C_{44}}{C_{11} - C_{12}} \tag{1.44}$$

The constants a, c, B and A_0 depend on the orientation of the indented surface and can be determined from Figure 1.12 which is the table provided by Vlassak and Nix in (Vlassak *et al.*, 1994). This table gives the constants a, c, B and A_0 for the three cube surfaces (100), (110) and (111) from the knowledge of $\nu_{\langle 100\rangle}$. $\nu_{\langle 100\rangle}$ corresponds to the Poisson's ratio of a uniaxial test along a $\langle 100\rangle$ crystallographic direction and can be obtained as:

$$\nu_{\langle 100\rangle} = -\frac{S_{12}}{S_{11}} = \frac{C_{12}}{C_{11} + C_{12}} \tag{1.45}$$

Then, from the value of the Zener ratio A (Eq. 1.44), the coefficient $\beta^{(hkl)}$ can be determined and E^* can finally be calculated according to Eq. 1.42. This method has however clear limits in the fact that it applies only to cubic crystals and to the particular (100), (110) and (111) orientations.

$$M_{(hkl)} = \beta_{(hkl)}\left(\frac{E}{1-\nu^2}\right)_{\text{isotropic}}, \quad \text{where } \beta_{(hkl)} = a + c(A - A_0)^B$$

	$\nu_{\langle 100\rangle}$	a	c	A_0	B	Range
(100)	0.20	1.409	−0.409	0	0.2367	$0.6 < A < 8$
	0.25	1.338	−0.338	0	0.2604	$0.6 < A < 8$
	0.30	1.277	−0.276	0	0.2845	$0.6 < A < 8$
	0.35	1.231	−0.231	0	0.3006	$0.6 < A < 8$
	0.40	1.198	−0.198	0	0.3022	$0.6 < A < 8$
	0.45	1.219	−0.219	0	0.2341	$0.6 < A < 8$
(110)	0.20	0.741	0.230	−0.893	0.1768	$0.8 < A < 6$
	0.25	0.730	0.245	−0.858	0.1512	$0.8 < A < 8$
	0.30	0.732	0.234	−1.338	0.1565	$0.8 < A < 8$
	0.35	0.724	0.229	−2.312	0.1549	$0.8 < A < 8$
	0.40	0.701	0.232	−4.548	0.1490	$1.0 < A < 8$
	0.45	0.682	0.260	−5.950	0.1052	$1.0 < A < 8$
(111)	0.20	0.751	0.259	0.172	0.2132	$0.8 < A < 6$
	0.25	0.725	0.278	0.062	0.1910	$0.8 < A < 6$
	0.30	0.741	0.258	−0.002	0.1901	$0.8 < A < 6$
	0.35	0.753	0.243	−0.081	0.1825	$0.8 < A < 6$
	0.40	0.741	0.254	−0.120	0.1524	$0.8 < A < 8$
	0.45	0.750	0.236	−0.472	0.1508	$0.8 < A < 8$

Figure 1.12: Table from (Vlassak *et al.*, 1994) to evaluate the parameters a, c, B and A_0 from $\nu_{\langle 100\rangle}$ for indentation on crystallographic surfaces (100), (110) and (111). This table also gives a framework of the anisotropy coefficient A in each case.

1.4.3 Nanoindentation as an emergent method to estimate single-crystal elastic constants

Nanoindentation has emerged as an important technique for the investigation of the local grain properties of materials. Its ability to perform localized measurements turned scientists' attention into trying to develop protocols combining nanoindentation and other characterization and modelling tools in order to study the elastic anistropy of materials and extract its SECs. It is very useful as sometimes, materials can have complex microstructures with multiple phases that render traditional testing techniques obsolete. By capturing the mechanical response of multiple grains of different orientations, nanoindentation is able to single-out and extrapolate the SECs of each individual phase. We are going to dive into how some of these researchers tackled the problem in their studies.

Relying on the robust nanoindentation protocol developed for spherical indentation (Kalidindi *et al.*, 2008; Pathak *et al.*, 2015), Weaver et al. (Weaver *et al.*, 2016) measured the indentation

modulus E^* for different grain orientations in a commercially pure Ti for two spherical indenter sizes (16 and 100 mm radii). α-Ti having a transversely isotropic symmetry, they plotted E^* as a function of the crystal c-axis declination angle (see Fig.1.13). They checked that measurements with 16 and 100 mm radii are highly consistent with each other. In addition, they performed crystal elasticity finite element simulations of spherical indentation (see Fig. 1.14), using a set of SEC taken from literature, to determine the variation of E^* with the c-axis declination angle. Their results showed that the simulations and experiments were in fairly good agreement with the most deviation occurring for fully inclined and declined orientations, which would suggest to slightly modify the set of SECs used. However, such tuning was not explored in their study.

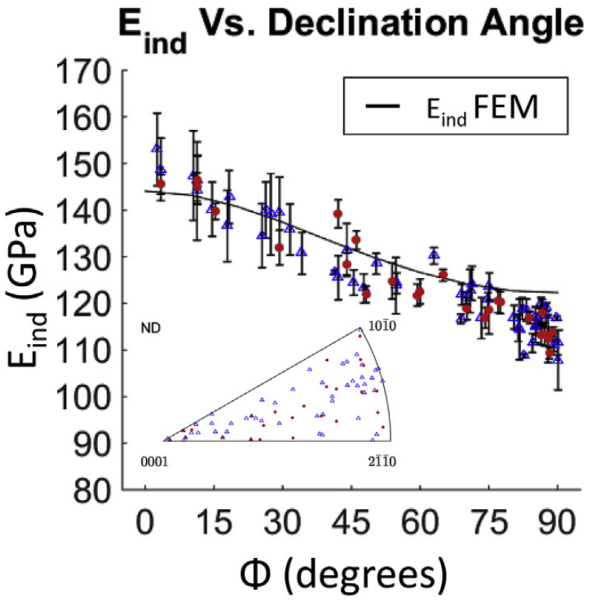

Figure 1.13: Indentation modulus (E_{ind} or E^* versus declination angle ϕ measured from 16 mm radius (blue) and 100 mm radius (red) indenters on CP-Ti. Comparison with FE prediction using SEC from literature Approximately, 25 grains (35 tests) and 50 grains (74 tests) were coonsidered for the 100 and 16 mm radius indenters, respectively. From (Weaver *et al.*, 2016)

.

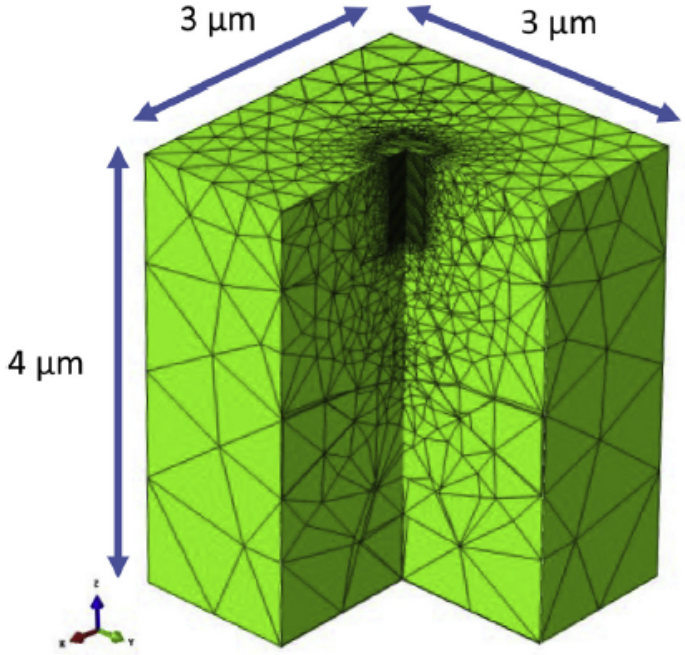

Figure 1.14: 3D FE model of the single crystal indenter specimen used. From (Weaver *et al.*, 2016)
.

Castillo et al. (Castillo *et al.*, 2019) presented a novel Bayesian framework (see further Section 1.5) for estimating SECs from spherical indentation stress-strain measurements. The primary aim of their study was to improve the accuracy and efficiency of determining the elastic stiffness parameters of single crystals by leveraging Bayesian inference and finite element (FE) simulations. In the first step, the authors created a reduced-order model using Bayesian inference to capture the relationship between indentation properties, crystal orientations and elastic stiffness parameters. The reduced-order model was built by systematically selecting a subset of high-value simulations from a large database, initially focusing on the boundaries of the parameter space and refining the model through sequential design strategies. This approach ensured that the model was both robust and accurate, efficiently exploring the multi-dimensional parameter space with fewer simulations. The model was then validated using cross-validation techniques to ensure its reliability.

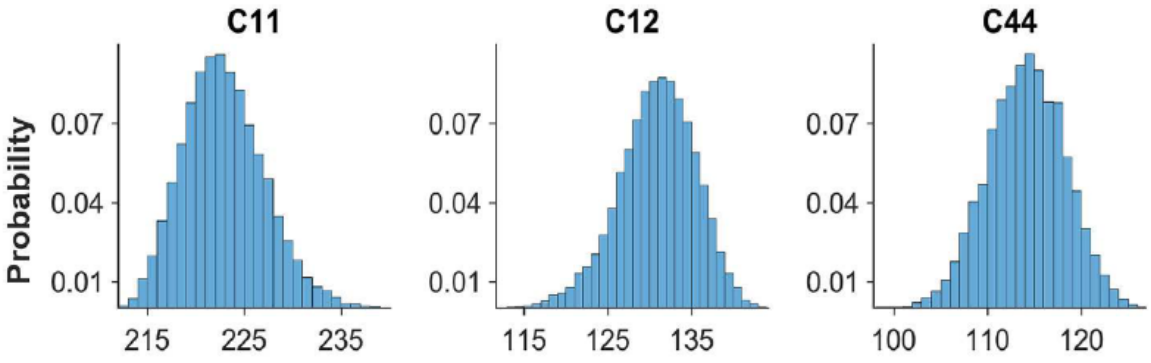

	C11	C12	C44
Mean (GPa)	222.88	130.88	114.13
STDEV	4.15	4.55	4.11

Figure 1.15: Posterior distributions of Fe 3% Si SECs. From(Castillo *et al.*, 2019)

The second step involved using Markov Chain Monte Carlo (MCMC) sampling to estimate the posterior distribution of the intrinsic material parameters based on experimentally measured indentation moduli from individual grains of different lattice orientations. This step involved calibrating the experimental data to the reduced-order model established in the first step. By employing this two-step Bayesian framework, the authors demonstrated its application to cubic polycrystalline Fe-3% Si (see Figure 1.15) and hexagonal polycrystalline commercially pure titanium (CP-Ti). The results showed good agreement with literature values.

Everaerts et al. (Everaerts *et al.*, 2019) developed a protocol to extract SECs from nanoindentation experiments on cubic materials which was applied to a polycrystallline nickel-based superalloy (RR1000). Their approach involves using electron backscatter diffraction (EBSD) to locate grains with specific crystallographic orientations (<100>, <110>, and <111>) relative to the sample surface. The reduced moduli of grains close to these orientations were measured through nanoindentation using a Berkovich tip. By combining the measured average reduced moduli and the reduced moduli computed by replacing directly the isotropic Young modulus E_S in Eq.1.30 by the directional Young's modulus $E^{(hkl)}$ obtained from the Euler angles of each grain in a least-squares optimization, the three independent cubic stiffness coefficients (C_{11}, C_{12}, and C_{44}) were calculated. A lower elastic anisotropy compared to existing data on similar alloys was observed. This result is

actually expected when using the directional Young's modulus $E^{(hkl)}$ as explained in Section 1.4.2. As a conclusion, Everaerts et al.(Everaerts *et al.*, 2019) suggested that their approach could be improved by implementing the model of Vlassak and Nix (Vlassak *et al.*, 1993; Vlassak *et al.*, 1994; Vlassak *et al.*, 2003) to estimate the reduced moduli and get more accurate results.

In conclusion, nanoindentation has proven to be an important technique in the investigation of local grain properties, allowing researchers to perform precise localized measurements that traditional methods often fail to achieve. It is able to isolate and extrapolate the single elastic constants (SECs) of individual phases within complex, multiphase materials. By analyzing the mechanical responses of multiple grains with different orientations, researchers have developed comprehensive protocols that combine nanoindentation with other analytical tools to study material anisotropy effectively.

1.5 Identification of material parameters by Bayesian inference

Bayesian inference, rooted in Bayes' theorem, is a sophisticated statistical method that offers the benefit of incorporating prior knowledge and beliefs into the analysis. It also effectively handles uncertainties present in observations, resulting in model parameters that reflect these uncertainties, thus providing a probabilistic framework. This allows for a more detailed understanding and interpretation of estimations, going beyond traditional methods that lack context (D'Agostini, 2003). A simplified version of Bayes theorem (Bayes, 1763) can be given by:

$$P\left(A|B\right) = \frac{P\left(B|A\right)P(A)}{P(B)} \tag{1.46}$$

where $P\left(A|B\right)$ is called the posterior probability. It is the probability that the hypothesis A is true given that the evidence B has occurred. $P\left(B|A\right)$ is called the likelihood. It is the probability of observing the evidence B given that the hypothesis A is true. $P(A)$ is the prior belief which is the probability of A being true before observing B. $P(B)$ is the probability of observing the

evidence B. $P(B)$ can be calculated by integrating over all possible values of A:

$$P(B) = \int_A P\left(B|A\right)\, dA \tag{1.47}$$

$P(B)$ is also often discarded as a normalization factor (Castillo *et al.*, 2019; Rappel *et al.*, 2018; Purohit *et al.*, 2021), but for some non-trivial models, $P(B)$ can be extremely difficult to estimate in a closed-form way.

Purohit et al. (Purohit *et al.*, 2021) investigated the SEC of a near-β titanium alloy using Bayesian inference (Bayes, 1763) combined with high-energy X-ray diffraction (HE-XRD) and micromechanical models. Their work primarily aimed to address discrepancies in the reported SEC of the β phase by employing a Bayesian framework to account for uncertainties and biases in experimental data and modeling parameters. The authors utilized HE-XRD data to monitor lattice strain evolution under in situ loading and applied an elastic self-consistent homogenization scheme to estimate the specimen and grain deformation behavior.

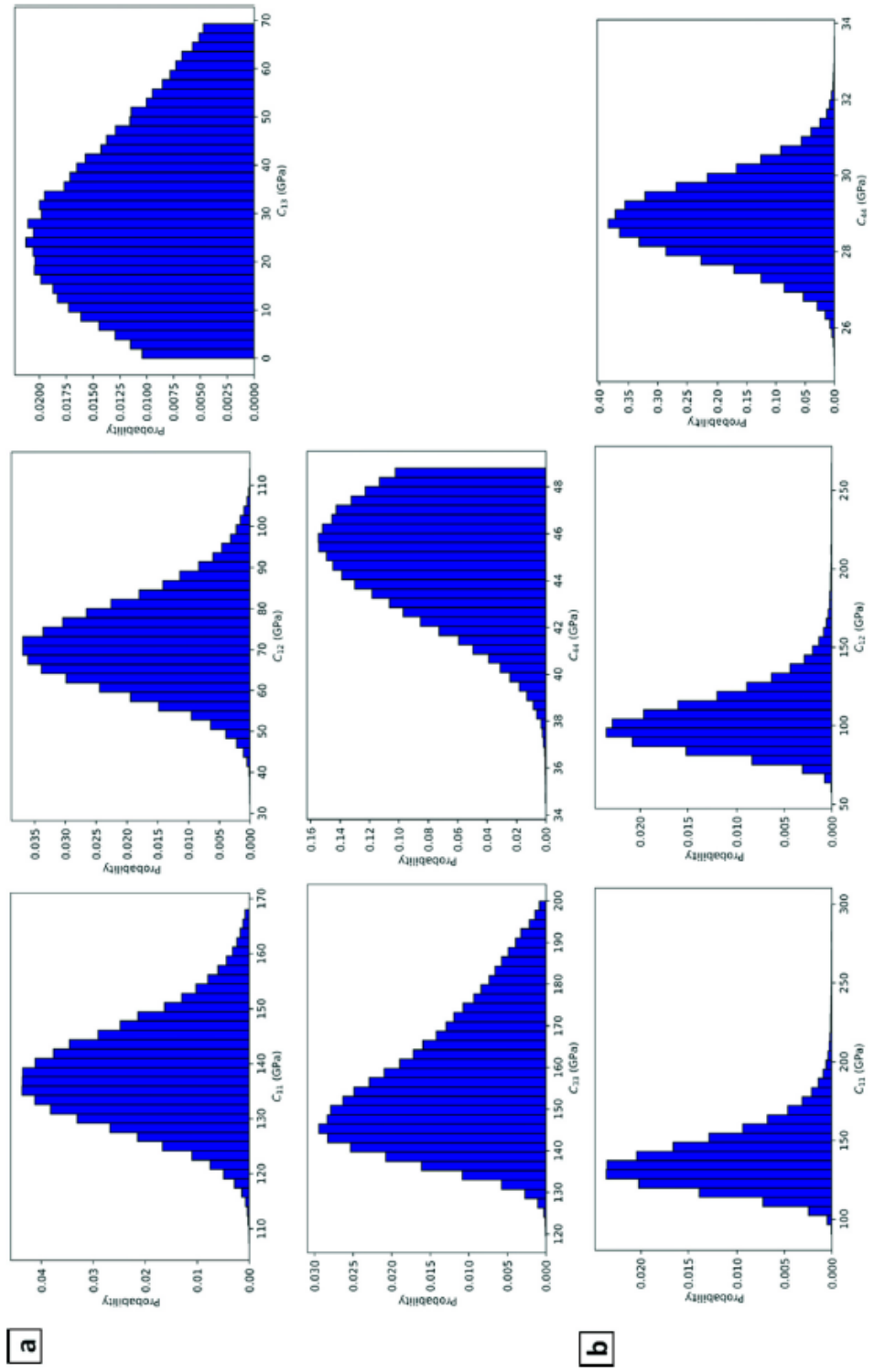

Figure 1.16: Probability distributions obtained for (a) the 5 SECs of the α phase and (b) the 3 SECs of the β phase. From (Purohit *et al.*, 2021)

Their results highlighted the importance of grain aspect ratio, often neglected in previous studies, in influencing the identified SEC. Through Bayesian inference, they deriveded the 5 SECs

of the α phase and the 3 SECs of the β phase of the studied near-β titanium alloy (see Figure 1.16). The Bayesian framework also provided a robust uncertainty quantification by keeping track of statistical means and standard deviations across the whole simulation. This variability of the obtained SEC values underscores the need for standardized methods and comprehensive datasets to get better SEC estimates.

Fernandez-Zelaia et al. (Fernandez-Zelaia *et al.*, 2018) developed a novel method for inferring the intrinsic post-elastic material constitutive properties from instrumented spherical indentation tests. FE simulations of the indentation process were used to inform and train a Gaussian Process (GP) surrogate model. The surrogate model was used within a Bayesian approach to efficiently estimate the unknown intrinsic constitutive model parameters. Results for perfectly plastic and power law hardening parametric constitutive models were obtained (see Figure 1.17). The proposed method produced initial yield estimates that agree well with experimental uniaxial tests. However, it was observed that discriminating between the hardening parameters was difficult and this was attributed to difficulty in producing sufficiently large strains during indentation.

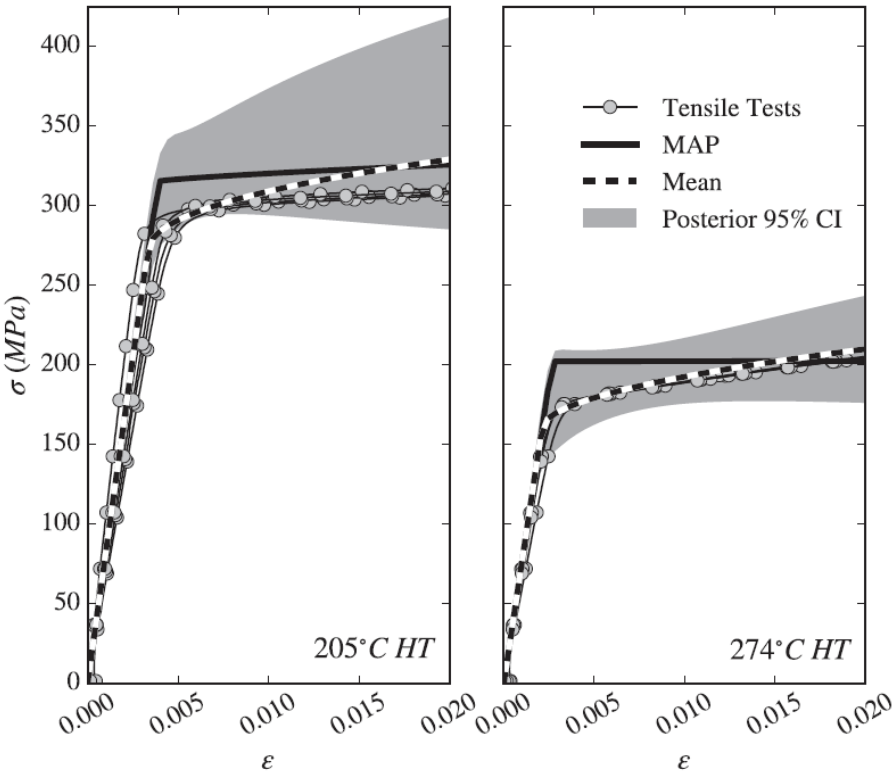

Figure 1.17: Tensile stress-strain curve estimates for Al-6061 with power law hardening assumption. Predictions from indentation inverse analysis and experimental uniaxial tensile tests. From (Fernandez-Zelaia *et al.*, 2018)

Recently, Venkatraman et al. (Venkatraman *et al.*, 2022) developed a comprehensive three-step Bayesian framework to estimate the intrinsic single crystal properties for the building of crystal plasticity models. The study focused on α+β Titanium alloys, particularly Ti-6Al-4V, for which the experimental work was already done by other members of their team (Millan-Espitia *et al.*, 2022). The first step in the framework involved developing a Gaussian Process Regression (GPR) surrogate model to predict the indentation yield strength from finite element (FE) simulations. This surrogate model was established using a sequential design of experiments strategy, optimizing the number of simulations required to achieve high accuracy. The second step employed Markov Chain Monte Carlo (MCMC) sampling to estimate the feasible configurations of intrinsic material parameters, providing rigorous uncertainty estimates for these properties. This step also helped in approximating the model evidence necessary for Bayesian model selection. In the final step, the study used Bayesian model selection to evaluate the model form probabilities for two specific crystal plasticity models. These models were calibrated using the estimated parameters. The

Bayesian framework facilitated the fusion of these models, combining their predictive capabilities to improve accuracy. This approach, even though computationally expensive, not only enhanced the understanding of the mechanical responses of α+β Titanium alloys but also demonstrated the potential applicability of the framework to other material systems and their respective CP models.

To sum up, the integration of Bayesian inference with computational models and advanced characterization techniques like HE-XRD or instrumented nanoindentation has significantly enhanced the reliability of intrinsic single crystal material parameter estimations. These approaches not only provide more accurate elastic constants but also offer deeper insights into the material's behavior under various conditions, paving the way for further advancements in materials science.

1.6 Conclusion

The characterization of single-crystal elastic constants (SECs) in multiphase polycrystalline materials presents significant challenges due to the complexity of their microstructures and the impracticality of obtaining large single crystals. Traditional experimental techniques, such as those utilizing ultrasonic wave velocities, while accurate for single crystals, are not feasible for polycrystalline materials. Techniques like the supersonic pulse echo method or X-ray diffraction have improved precision but still face limitations in polycrystalline contexts. The limitations of these traditional methods become even more apparent when applied to complex, multiphase materials. These methods often yield only macroscopic elastic constants and fail to distinguish the properties of individual phases. This necessitates the development of more localized and advanced techniques.

Nanoindentation has emerged as a powerful tool for addressing these challenges, offering precise, localized measurements of elastic properties. Its utility is particularly pronounced when analyzing anisotropic materials, where directional dependencies of elastic moduli can be captured. The development of semi-analytical micromechanical models, such as the one proposed by Vlassak and Nix, has provided a framework for interpreting nanoindentation results in anisotropic materials, facilitating the calculation of indentation moduli across various crystallographic orientations.

Furthermore, Bayesian inference has become a valuable tool in this context, enabling the incorporation of prior knowledge and the quantification of uncertainties in SEC estimations. By

integrating nanoindentation data with Bayesian inference, researchers can now derive more robust and statistically sound estimates of elastic constants, accounting for variability in experimental data and prior assumptions.

The combination of these methodologies—instrumented nanoindentation, the Vlassak and Nix model, and Bayesian inference—should provide a comprehensive and efficient framework for determining the elastic properties of materials, even in cases where traditional methods fall short. This chapter has reviewed the current state of knowledge in these areas and laid the foundation for the subsequent experimental and numerical works, which will further explore the practical application of these techniques in the study of materials such as high-purity Nickel and Inconel 718.

Chapter 2

Experimental Procedure

2.1 Introduction

This chapter outlines the experimental procedures employed to accurately determine the single-crystal elastic constants (SECs) of cubic materials using nanoindentation. Given the complex nature of material behavior, particularly in anisotropic and multiphase materials, careful consideration must be given to every stage of the experimental process to ensure reliable and reproducible results.

The choice of materials plays a pivotal role in the study. High-purity Nickel (99.99%) has been selected as a reference material due to its well-documented mechanical properties, providing a benchmark for the validation of the nanoindentation protocol. Inconel 718, a more complex material with a less established SEC profile, serves as a target material, allowing us to explore the robustness of the developed methodologies on a less-known alloy.

The preparation of the samples is critical to the success of the nanoindentation experiments. This chapter details the surface preparation techniques that were employed to minimize surface roughness and ensure optimal conditions for accurate indentation measurements. Electron Backscatter Diffraction (EBSD) was utilized to characterize the crystallographic orientation of the grains, which is crucial to correlate the measured elastic properties to the local crystallographic orientations.

Additionally, the calibration of the spherical indenter is discussed in depth, highlighting its

importance for the accuracy of the measurements. The nanoindentation experiments were performed using sinus mode to obtain the force-displacement curves, and specific parameters were carefully chosen to optimize the extraction of the elastic properties. Lastly, this chapter details the high-speed nanoindentation mapping performed at ICA on Nickel and Inconel 718 to explore the spatial distribution of mechanical properties at the microstructural level.

By providing a clear and detailed description of the experimental methodology, this chapter establishes a solid foundation for the accurate determination of SECs and serves as a critical component of the overall research framework presented in this thesis.

2.2 Material's choice

The materials chosen for this study were selected to encompass a variety of materials with cubic crystallographic symmetry. Materials with large grains are targeted in order to perform multiple tests per grain without being affected by the grain boundaries. High purity Nickel (99.99%) (Ni) provided by GoodFellow was chosen as the reference material because its properties (SECs here) are well documented (Honda *et al.*, 1937; Bozorth *et al.*, 1949; Bozorth *et al.*, 1951; Neighbours *et al.*, 1952; Levy *et al.*, 1953; De Klerk *et al.*, 1955; Shirakawa *et al.*, 1958; De Klerk, 1959; Alers *et al.*, 1960; Sakurai *et al.*, 1964; Epstein *et al.*, 1965; Vintaikin, 1966; Salama *et al.*, 1969; Shirakawa *et al.*, 1969). Inconel 718 (IN718) on the other hand, is a relatively new and less known material (Haldipur, 2006; Martin *et al.*, 2014; Schröder *et al.*, 2023) and will serve as our target material. IN718 was supplied as a rolled plate in solid solution state and its chemical composition was Ni-18.5Cr-18.3Fe-5.0(Nb+Ta)-3.0Mo-1.0Ti-0.6Al-0.03C (wt.%). The sample preparation as well as the EBSD and parts of the indentation experiments on the Ni were performed at the LEM3 laboratory in Metz, France, while all of the above for the IN718 sample were performed at Institut Clement Ader (ICA) in the UMR CNRS 5312 laboratory in Albi, France.

2.3 Sample preparation

Sample surface preparation is an essential and vital step in nanoindention testing as it ensures the accuracy and repeatability of said tests resulting in consistent results. Both materials underwent quasi-similar mechanical polishing procedures in order to ensure a flat, parallel, and minimally work-hardened surface.

2.3.1 High Purity Ni

For the Ni sample, a heat treatment was initially performed at 900 °C for two hours to eliminate any residual stresses resulting from the casting process. This thermal process is essential for stabilizing the material's internal structure, creating a more homogeneous state, and preparing it for further stages of processing. By reducing the effects of residual stresses, this heat treatment contributes to both dimensional stability and the material's overall integrity.

Following this, the samples were subjected to a detailed mechanical polishing process aimed at achieving an extremely smooth surface. The polishing procedure begins with a series of abrasive papers of progressively finer grit sizes, which ensure a controlled and gradual smoothing of the surface. The first stage uses $P\#1200$ abrasive paper, which has a particle size of $15\,\mu$m, to remove larger surface irregularities and other initial imperfections. After this initial pass, $P\#2000$ abrasive paper is employed, followed by $P\#4000$ abrasive paper with a finer particle size of $5\,\mu$m, each successive step refining the surface to a smoother finish.

After completing the abrasive paper stages, a second polishing step is carried out using diamond solutions. The application of diamond suspensions down to a particle size of $3\,\mu$m (DiaPro Mol) further enhances the smoothness of the surface, effectively minimizing surface roughness and creating a more polished base.

The final step in the polishing sequence involves the application of a colloidal silica solution, or oxide polishing suspension (OPS), with particles as fine as $0.25\,\mu$m. This last stage is crucial, as it removes any remaining minor scratches and leaves the surface in a near-perfectly smooth, mirror-like state. This level of finish is necessary for advanced characterization techniques, such

as electron backscatter diffraction (EBSD) and nanoindentation testing, where surface quality is paramount. To ensure consistency, each polishing step was repeated as needed, thus achieving a homogeneous surface condition across all samples.

Finally, an electropolishing stage was introduced to further refine the surface. This step utilized an electrolytic solution composed of sulfuric acid and methanol, which serves to dissolve small amounts of material from the surface, thereby eliminating any final irregularities. Electropolishing is essential to achieving an exceptionally smooth, flat surface free from residual imperfections, preparing the samples for high-precision material testing and analysis.

2.3.2 Inconel718

As for the In718 sample, to promote grain growth and achieve a uniform recrystallization with minimal grain orientation spread, a short heat treatment was administered. The sample was held at 1080 °C for 5 minutes, followed by a rapid water quenching. This specific heat treatment step favors grain boundary mobility, allowing the grains to grow and recrystallize in a manner that minimizes directional grain orientation, which can otherwise affect mechanical properties and the material's response to subsequent tests.

Following this, a two-stage aging treatment was applied to precipitate strengthening phases within the alloy matrix. The first stage consisted of an 8-hour hold at 720 °C with a cooling rate of 50 °C per hour, and then a second stage at 620 °C for an additional 8 hours, followed by furnace cooling. This thermal treatment sequence was designed to precipitate L12-γ'-Ni3(Ti,Al) and DO22-γ"-Ni3Nb phases within the γ-Ni matrix. These fine precipitates enhance the alloy's strength and thermal stability. However, it must be underlined that their distribution and size are too narrow and small to be evaluated individually by nanoindentation techniques, as the scale of the phases is beyond the resolution of conventional nanoindentation methods.

For surface preparation, mechanical polishing was employed to ensure that the sample achieved a high degree of flatness and parallelism, critical for precise mechanical testing. A precision jig was used with abrasive paper down to a P#4000 grit size, which effectively minimized surface work-hardening and ensured consistency in the polished surface. Subsequent manual polishing

involved diamond particles, beginning with a particle size of 3 µm and progressing down to 0.25 µm. This step aimed to minimize surface scratches that could interfere with measurements or introduce inaccuracies during testing.

The surface finish was further refined with a mechanical polishing stage lasting 20 minutes, followed by vibratory polishing for an additional 3 hours using a colloidal silica solution containing 0.05 µm particles. This final polishing sequence was crucial, as it provided an ultra-smooth surface finish required for high-precision characterization. Special attention was given to thorough surface cleaning after each stage to prevent particle contamination, ensuring that the surface was pristine and free from any residues that could impact the material's characterization.

2.4 Microstructure characterization

The microstructure of our samples was characterized using Electron Backscatter Diffraction (EBSD) imaging through a Scanning Electron Microscope (SEM). This technique enables the acquisition of detailed maps revealing the local orientation of the polycrystalline microstructure of the samples. For Ni, EBSD characterizations were performed with a step size of 5 μm and a field of view of 3.9 $\times$ 4.8 mm using a JEOL JSM 6490 scanning electron microscope equipped with a tungsten filament and an Oxford Instruments Symmetry S2 EBSD acquisition system. EBSD data were post-treated and plotted using MTex (Hielscher *et al.*, 2008). The maps yielded by this technique were used to choose candidate grains for the spherical nanoindentation tests on high-purity Ni. The average grain diameter of the testing zone was 203 μm, as shown in Figure 2.1.

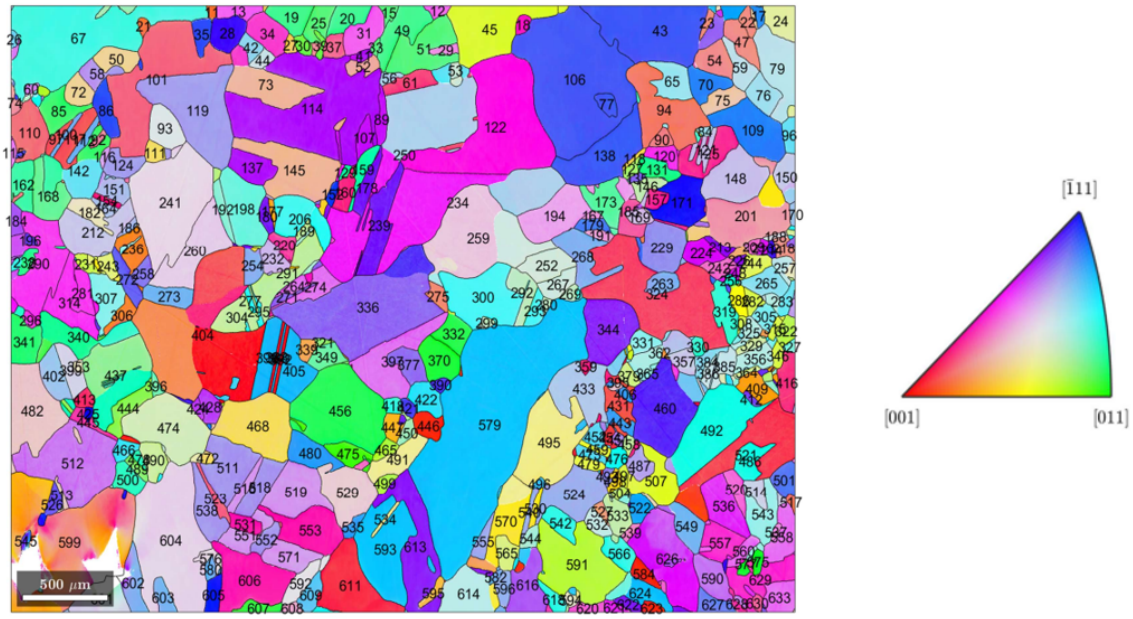

Figure 2.1: EBSD map and inverse pole figure of the high-purity Ni sample along the indentation direction (for the indentation measurements at LEM3)

For the IN718 material, EBSD characterizations were performed with a step size of 0.4 μm and a field of view of 1.0 $\times$ 1.0 mm using a JEOL JSM 7100F scanning electron microscope that is also equipped with a Symmetry S2 EBSD detector (Oxford Instruments). EBSD data were post-treated and plotted using MTex (Hielscher *et al.*, 2008) and the open source Pymicro library [1]for further correlative mechanical microscopy (Marano *et al.*, 2024; Proudhon *et al.*, 2024).

2.5 Spherical nanoindentation measurements in Sinus mode (Ni at LEM3)

The UNHT nanoindenter (Fig.2.2) manufactured by Anton Paar (Austria) was used to perform spherical nanoindentation tests on high-purity Ni. It was chosen to perform the indendations in Sinus mode, a dynamic testing mode in which the sample is loaded with a cyclically applied increasing load, in order to better evaluate the indentation modulus from statistical data. This mode allows indeed the characterization of the indentation modulus as a function of depth (Fischer-Cripps *et al.*, 2004) and the possibility to reach stabilized values.

[1]`https://github.com/heprom/pymicro`

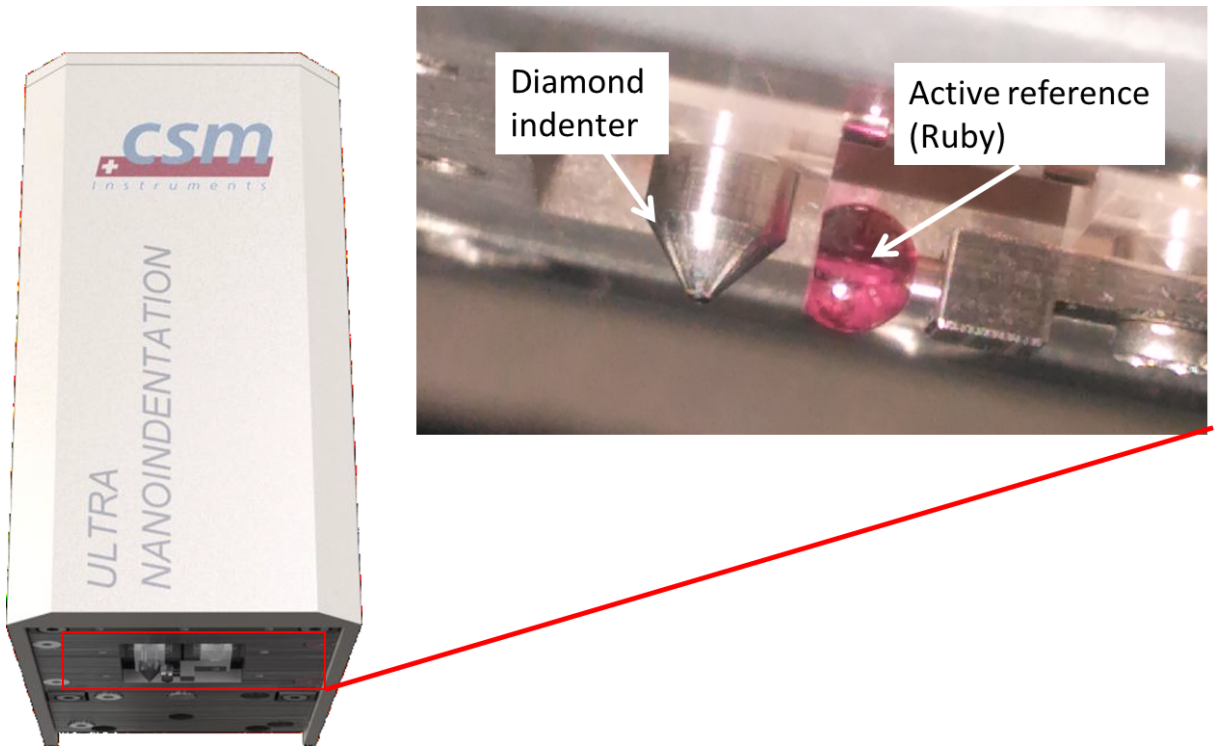

Figure 2.2: UNHT module manufatured by Anton Paar
used for the spherical nanoindentation measurements

2.5.1 Spherical indenter calibration

Calibrating a spherical indenter is essential to ensure accurate measurements during nanoindentation testing, especially in determining accurate properties like the indentation modulus. Spherical indentation involves applying a known load through an indenter with spherical tip onto the surface of our sample, generating an elastic-plastic deformation. Proper calibration ensures that the forces and displacements recorded during the indentation are accurate, which is critical in converting the data into meaningful mechanical properties. Inaccuracies in calibration can lead to significant deviations in the results, affecting the interpretation of material behavior under stress. Additionally, the calibration can be used to account for geometric imperfections. Manufacturing deviations in the size of the indenter's tip are common and can introduce errors in the contact area calculation, which is essential for precise material property determination, as even minor deviations can lead to incorrect measurements. In this subsection, two methods used for calibrating our spherical indenter are going to be presented: the first one is purely based on the geometry of the indenter and

the contact parameters discussed earlier, while the second one uses Kalidindi's method presented in Section 1.4.1.

Calibration of the indenter using the projected area of contact function

The projected area of contact A_p can be easily deduced using the geometry of the indent when in contact (see Figure 1.7). It depends on the indenter's radius R and the contact depth h_c and is given by (cf. Eq.1.22):

$$A_p = \pi a^2 = -\pi {h_c}^2 + 2\pi R h_c \tag{2.1}$$

The first step consists of doing a series of measurements on a known material at different maximal forces, and therefore different maximal depths. The material has to be homogeneous and elastically isotropic and must have a known Young's modulus and Poisson's ratio (or a known anisotropic modulus). For the calibration of our spherical indenter, fused silica has been chosen as the calibration material because it fulfills these two conditions. Its anisotropic modulus was given by the manufacturer as $E^* = 75.1 \pm 0.3 GPa$.

Different measurements were performed on the fused silica up until the maximum force that the nanoindentation machine is capable of, which is 100 mN. For each measurement, A_p and h_c were kept track of.

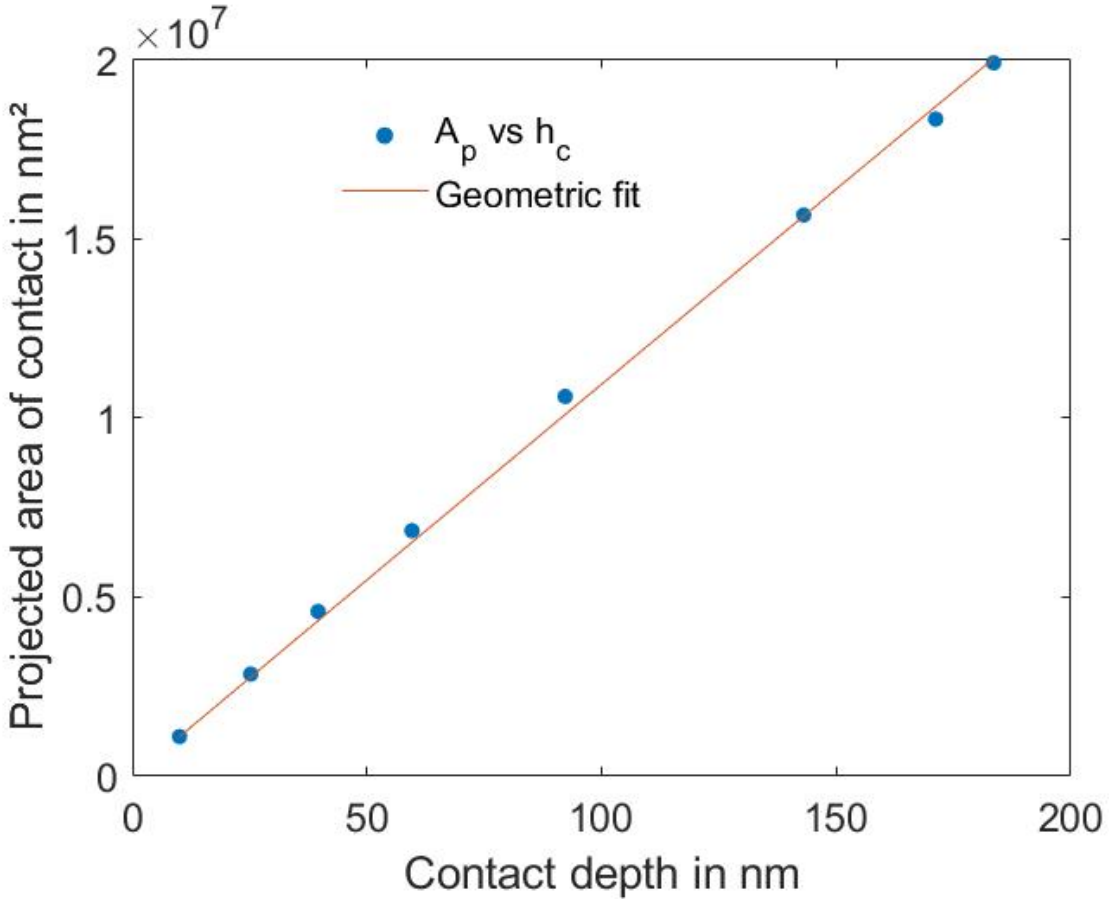

Figure 2.3: Projected contact area (A_p) as a function of contact depth (h_c) with a geometric fit

An expression for A_p as a function of h_c is obtained by performing a second degree polynomial fit as : $A_p = -\pi {h_c}^2 + 109803.29 h_c$ and a value of R can then be deduced from it. The radius obtained for our spherical indenter using this method is $R = 17.5\,\mu$m.

Calibration of the indenter using Kalidindi's method

Pathak et al. (Kalidindi *et al.*, 2008; Pathak *et al.*, 2015) have developed a method to determine an effective zero-point (h^*, F^*) that can be assimilated to the actual point of contact from which they start their analysis of the loading part of the nanoindentation curve. Using this method (see also Section 1.4.1), we are able to determine the anisotropic elastic modulus E^* for a known spherical indenter's radius, or find the spherical indenter's radius for a known E^*. To do so, a linear fit is done on the elastic part of the nanoindentation curve following the Hertz's model (Hertz, 1896, see also Eq. 1.20):

$$h_e - h^* = k\,(F - F^*)^{\frac{2}{3}} \tag{2.2}$$

$$k = \left[\frac{3}{4}\frac{1}{E_{eff}}\frac{1}{\sqrt{R_{eff}}}\right]^{\frac{2}{3}} \tag{2.3}$$

Here, P and h_e are the measured experimental load and elastic displacement. E_{eff} is the effective indentation modulus, R_{eff} is the indenter's effective radius and k is the slope of the linear fit. Actually, multiple linear fits between h_e and $(F - F^*)^{\frac{2}{3}}$ are performed for a set of different values of F^*. The value of F^* that yields the lowest residual error in the least-squares fit is kept and the values of h^* and k are then obtained from the corresponding linear fit. The value of R_{eff} is then deduced from the value of k and the knowledge of E_{eff} according to Eq. 2.3.

By applying this method on the same spherical indenter and the same fused silica, the radius found is $R = 18\,\mu$m, which is very similar to the radius obtained using the projected area of contact function calibration ($R = 17.5\,\mu$m).

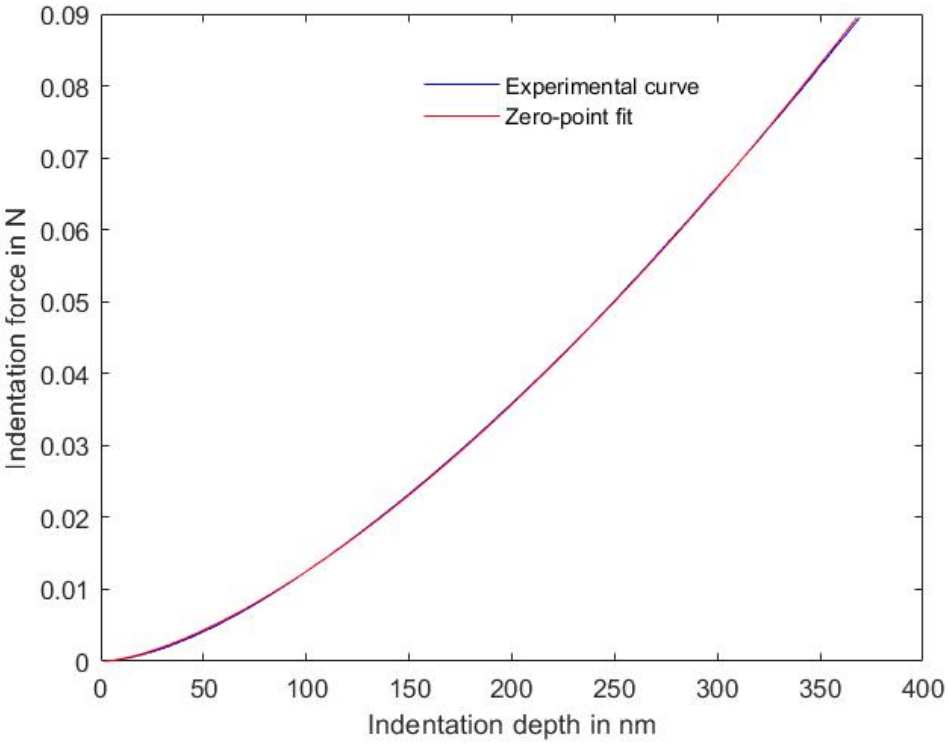

Figure 2.4: Experimental loading part of a nanoindentation experiment on fused silica (in blue) compared to the curve obtained using the fit in Eq.2.2 (in red)

Fig.2.4 shows the close overlap between the experimental nanoindentation curve obtained on the fused silica and the one derived from the fit of Hertz's model, indicating an excellent agreement. It validates the zero-point correction applied to the experimental data and highlights the reliability of the radius value obtained using this method.

2.5.2 Sinus mode measurements

For nanoindentation tests in Sinus mode, an oscillating force $F(t)$ was applied :

$$F(t) = F_0 \sin(\omega t) \tag{2.4}$$

where F_0 represents the force amplitude. Tests were performed at constant value of $\dot{F}_0/F_0$. Four indents shaped as a 2×2 matrix were made on each grain. The minimum distance between indents was set as 30 μm. The parameters of the tests are given in Table 2.1.

The Sinus mode was chosen in order to better evaluate the indentation modulus from statistical

Maximum force F_{max}	60 mN
Maximum amplitude at F_{max}	6 mN
Constant Strain rate $\dot{F}_0/F_0$	$0.05\,s^{-1}$
Oscillating frequency ω	5 Hz

Table 2.1: Experimental parameters used for the nanoindentation tests performed in Sinus mode with a spherical on high-purity Ni.

data as it allows the possibility to reach a stabilized modulus as a function of the depth. The different steps to measure the anisotropic indentation modulus E^* from this dynamic mechanical testing is sketched in Fig. 2.5 and explained in the following. Under the assumption of small amplitude oscillations, the oscillating force $F(t)$ (Eq. 2.4) generates an oscillating penetration depth $h(t)$ with a phase shift angle δ in a linear approximation (Cheng *et al.*, 2006):

$$h(t) = h_0 \sin(\omega t + \delta) \tag{2.5}$$

where h_0 is the displacement amplitude. The stiffness S of the sample at each cycle is then related to δ as follows (VanLandingham, 2003):

$$S = \frac{F_0}{h_0}\cos\delta + m\omega^2 - K_i \tag{2.6}$$

m is the mass of the indenting module and K_i is the dynamic stiffness of the instrument. The values of the parameters m and K_i were obtained through a specific calibration procedure where the tip oscillates in the air. The indentation contact depth h_c at (F_0, h_0) can then be computed using Eq.1.17 with $\varepsilon = 0.75$ for a spherical indenter (Oliver *et al.*, 2004):

$$h_c = h_0 - 0.75\frac{F_0}{S} \tag{2.7}$$

Next, the contact radius a of the projected area of contact $A_P = \pi a^2$ can be deduced from Eq.1.22 as:

$$a = \sqrt{2Rh_c - h_c^2} \tag{2.8}$$

The effective (or reduced) indentation modulus E_{eff} is thus obtained from Eq. 1.19 with $\beta = 1$

for an axis-symmetric indenter:

$$E_{eff} = \frac{\sqrt{\pi}}{2}\frac{S}{\sqrt{A_P}} = \frac{S}{2a} \tag{2.9}$$

Finally, the value of E^* is deduced from Eq.1.36 as:

$$E^* = \frac{1}{\dfrac{1}{E_{eff}} - \dfrac{1-\nu_i^2}{E_i}} \tag{2.10}$$

where $\nu_i = 0.07$ and $E_i = 1141\,\text{GPa}$ denote the Poisson's ratio and the Young's modulus of the isotropic diamond indenter, respectively.

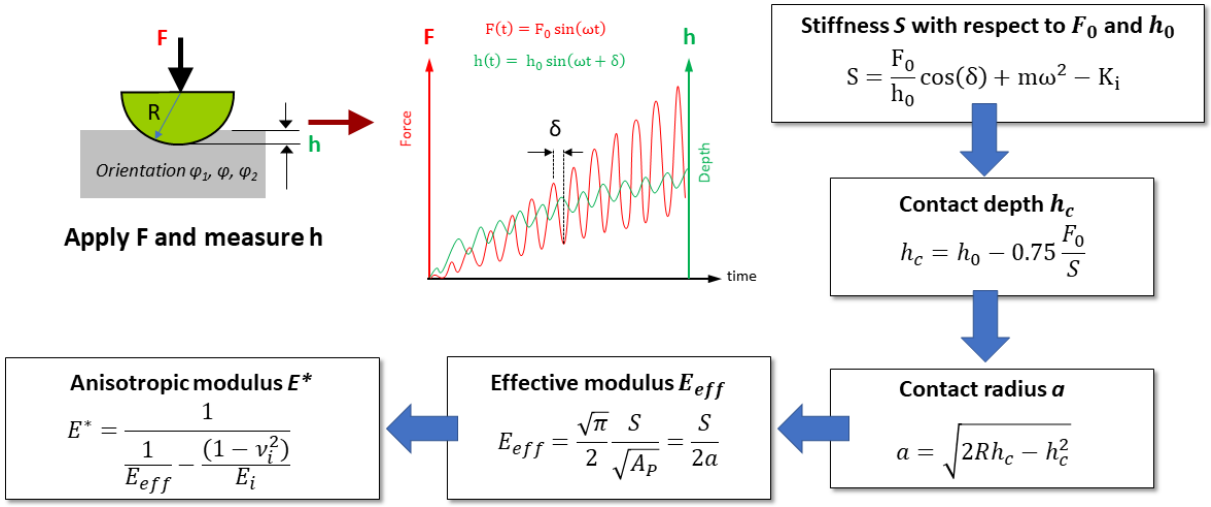

Figure 2.5: Experimental protocol to obtain E^* using a spherical tip and the Sinus mode.

As a result, a variation of E^* with respect to the penetration depth h is obtained. E^* tends to a stabilized behavior as depth increases as it can be observed in Fig. 2.6. Sliding averages over depth range of 10 nm were first applied on the E^* values. The average of E^* between $h = 200\,\text{nm}$ and $h = 300\,\text{nm}$ was then computed and kept as the value for the forthcoming analyses.

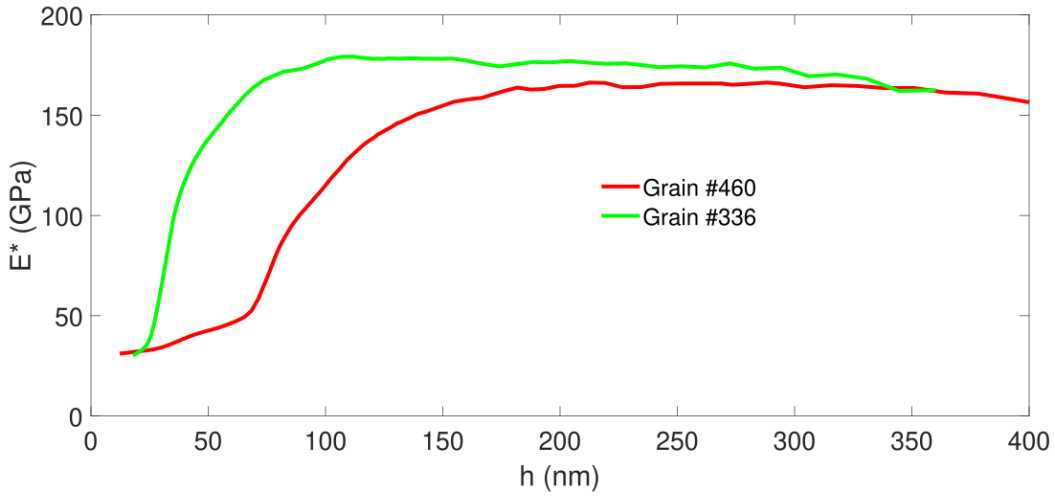

Figure 2.6: Examples of variation of E^* with the depth h for two different Ni grains using the Sinus mode of the UNHT nanoindenter.

2.6 High speed nanoindentation mapping (Ni and IN718 at ICA)

High speed nanoindentation mapping (HSNM) was performed with a diamond-type Berkovich tip on both materials using a customed FTI04 and a NMT04 nanoindentation system both from Femtotools^{AG} for the pure Ni and the IN718 samples, respectively. Tests were conducted in continuous stiffness measurement (CSM) mode which is similar to the Sinus mode. However, much higher frequencies can be applied with the systems of Femtotools^{AG}. Moreover, tests can be performed in displacement control allowing for similar indentation depths from indent to indent, regardless of the local mechanical response. Hence, at ICA, the samples were loaded with a cyclically applied increasing penetration depth. These dynamic tests have to be performed below the first resonance mode of the system. Based on the different resonance frequencies of the systems, the CSM frequency was adapted to both the system and sample. A 20 mN load cell with a position noise floor ± 0.05 nm and a load noise of $\pm 0.05\,\mu$N (MEMS sensor) was used. The Berkovich tip was calibrating using a fused silica with isotropic elastic properties and known indentation modulus in displacement-controlled mode. For the fused silica, the values of the reduced (or effective) modulus E_{eff} stabilized for contact depth h_c ranging from 20 to 300 nm.

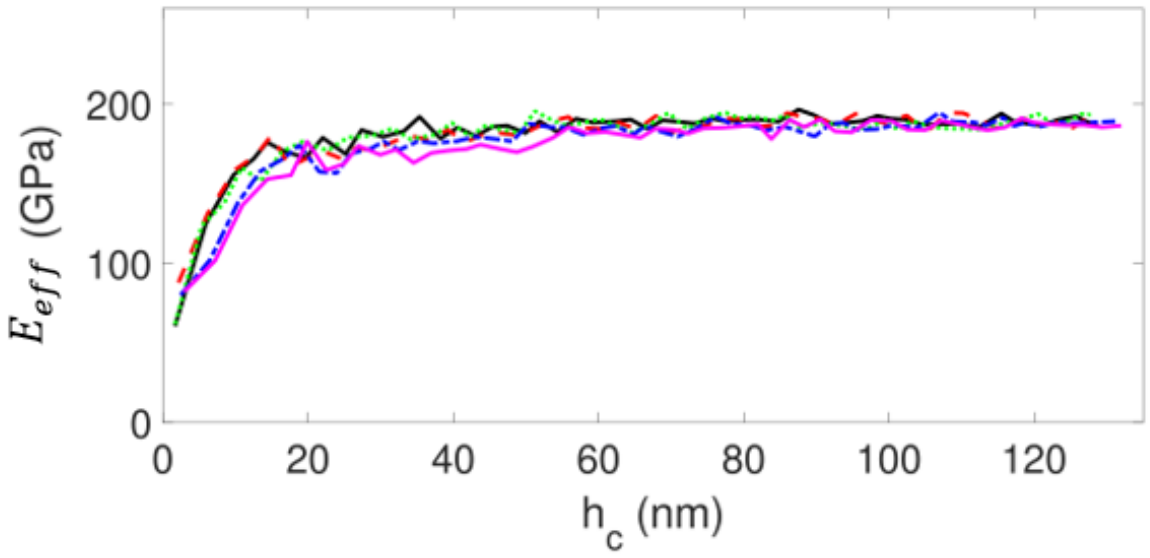

Figure 2.7: Examples of variation of the reduced modulus E_{eff} with the contact depth h_c for 5 indents in a same grain of the IN718 sample.

The different steps to measure the anisotropic indentation modulus E^* in CSM mode is explained briefly in the following. The displacement of the tip $h(t)$ oscillates at the CSM frequency f_{CSM}. Under the assumption of small amplitude oscillations, this generates an oscillating force $F(t)$ with a phase shift angle δ in a linear approximation (Cheng *et al.*, 2006). The stiffness S of the sample at each cycle can then be related to δ foillowing Eq. 2.6 (VanLandingham, 2003). Besides, the reduced modulus E_{eff} is related to S according to Eq.1.19 with $\beta = 1.034$ for a Berkovich tip. As a result, a variation of E_{eff} with respect to h_c is obtained. E_{eff} tends to a stabilized behavior as depth increases, as it can be observed in Fig. 2.6. A single value of E_{eff} was then evaluated for each measurement point using the average value for contact depth between 80 and 120 nm. At the end, the values of E^* were deduced from Eq.2.10.

For the high-purity Ni, a map of 400×250 indents was made with a step size of 10 μm. For the IN718 sample, a map of 300×300 indents was made with a step size of 2 μm. The nanoindentation parameters for each map are reported in Table 2.2. Based on the noise floor for displacement and force channels, a linear regression between 1 and 30 μN was used from the force vs. displacement curve to estimate the contact point for each measurement point as the interception between the regression line and the abscissa.

After performing the high speed nanoindentation mapping, correlative mechanical microscopy

Table 2.2: Nanoindentation parameters in CSM and displacement control mode

	Ni	IN718
Array size (indents)	400 × 250	300 × 300
Step size (µm)	10.0	2.0
CSM frequency (Hz)	50	200
Max depth (nm)	120	120
Load rate ($nm.s^{-1}$)	100	90
Displacement amplitude (nm)	const. 3	const. 5
Approach wait (s)	0.2	0.1
Unload time (s)	0.02	0.02
Trigger force (µN)	10	20
Frame stiffness ($N.m^{-1}$)	24372.0	10624.3

analyses were conducted using both EBSD measurement and nanoindentation response (see ref. (Texier *et al.*, 2024) for more details). Non-rigid registration of the EBSD maps was performed in order to affect orientation information for each nanoindentation measurement. Grains were segmented and labelled. Grain erosion was carried out in such a way as to take into account only nanoindentation tests carried out more than 4 μm away from a grain boundary. A sampling mask was also applied on the IN718 data to remove indents located in carbides, identified both on backscattered electron images and indendation maps (high hardness and stiffness). Average values per grain of E^* along with standard deviations were subsequently computed. In total, 158 and 176 grains were available for the high-purity Ni and the Inconel 718 samples, respectively. However, for the Bayesian simulations, only large grains having a standard deviation on E^* lower than 12 GPa were kept. The purpose of this approach was to increase even more the robustness of the input data by ensuring that average values of E^* result mostly from indents far way from grain boundaries. Considering the difference of grain size and step size between the two samples (see Table 2.2), grains with equivalent diameter greater than 100 μm and 6 μm were selected for the Ni and IN718 samples, resulting in reduced numbers of 57 and 69 grains, respectively.

2.7 Conclusion

In this chapter, we have detailed the experimental methodology to characterize the sample microstructures by EBSD and perform nanoindentation tests in Sinus or CSM mode. The selection

of materials, notably high-purity Nickel and Inconel 718, is made strategically to ensure that both a well-characterized and a more complex, less-documented material are studied. This approach allows us to validate the protocol against established reference data while exploring its application to materials with more intricate microstructures.

Sample preparation is a crucial aspect of this methodology, with emphasis placed on achieving optimal surface conditions for accurate indentation. The use of Electron Backscatter Diffraction (EBSD) provides essential crystallographic orientation data, ensuring that the indentation measurements can be directly correlated to specific grain orientations. This step is pivotal for moving from local grain properties to the estimation of SECs.

The calibration of the spherical and Berkovich indenters and the careful selection of experimental parameters are equally critical to the reliability of the results. By conducting nanoindentation in Sinus or CSM mode, we are able to obtain high-quality force-displacement curves that form the basis for further analysis. Additionally, the high-speed nanoindentation mapping enables a comprehensive examination of the spatial distribution of mechanical properties, especially for the more complex microstructure of Inconel 718.

In summary, this chapter has laid the groundwork for the subsequent numerical and analytical analysis by providing a robust and thoroughly executed experimental protocol. The methodologies described here ensure the reliability of the nanoindentation results, which will be integrated with analytical models and Bayesian inference simulations in the chapters that follow.

Chapter 3

Numerical implementation of Vlassak & Nix model and applications

3.1 Introduction

The study of anisotropic elastic properties is essential for materials used in high-performance applications, where the direction-dependent behavior of materials significantly influences their mechanical performance. We have witnessed how nanoindentation has become an invaluable tool for probing these properties. The Vlassak and Nix micromechanical model allows to estimate the anisotropic modulus E^* across various crystallographic orientations, leveraging an approach built on the surface Green's function and Stroh formalism.

To enhance computational efficiency, the numerical implementation incorporates Gauss-Legendre quadrature, allowing for rapid and accurate integrals evaluation. This chapter develops the theoretical framework, detailing how the model employs eigenvalues and eigenvectors related to the Stroh sextic equation to determine E^* efficiently. Through practical case studies, we validate the model and explore how variations in material parameters, such as shear resistances and elastic anisotropy coefficient, impact the indentation modulus. This approach not only refines the computational time but also provides a robust foundation for interpreting anisotropic behavior in experimental applications, advancing the study of directional mechanical properties in nanoindentation.

3.2 Matrix Formalism

We have explained in Chapter I that Vlassak and Nix (Vlassak *et al.*, 1993; Vlassak *et al.*, 1994; Vlassak *et al.*, 2003) developed a comprehensive theory that enables the evaluation of the anisotropic modulus E^* for a given crystallographic orientation, provided that the elastic constants of the material are known. This theory is grounded in the surface Green's function method, originally derived by Barnett and Lothe (Barnett *et al.*, 1975) within the Stroh formalism (Stroh, 1958), which provides an efficient mathematical framework for addressing anisotropic elastic problems. The formalism is particularly useful in the analysis of dislocations and elastic interactions within anisotropic materials, and it is this flexibility that Vlassak and Nix leveraged to compute E^* in anisotropic crystals.

Their model assumes that the indenter geometry corresponds to a circular flat punch, a simplifying assumption that still allows for accurate computation of E^* under various crystallographic orientations. Within this framework, Vlassak and Nix (Vlassak *et al.*, 1993; Vlassak *et al.*, 1994; Vlassak *et al.*, 2003) demonstrated that the indentation modulus E^* could be expressed from:

$$E^* = 4\pi \left(\int_0^{2\pi} n_i B_{ij}^{-1}(\omega) n_j \, d\omega \right)^{-1} \tag{3.1}$$

In equation 3.1, the matrix $\boldsymbol{B}$, which depends on the stiffness tensor $\boldsymbol{C}$, was originally expressed as a line integral (Vlassak *et al.*, 1993; Vlassak *et al.*, 1994; Vlassak *et al.*, 2003) through Eq.1.41. The matrix $\boldsymbol{B}$ can, however, be computed more efficiently by employing the Stroh matrix (also known as the sextic matrix) formalism. This method provides a more streamlined approach to evaluating the elastic properties of anisotropic materials, particularly when combined with modern computational techniques. The Stroh matrix formalism is widely regarded as one of the most effective methods for solving problems related to anisotropic elasticity, and it has been further developed and applied in numerous studies (Stroh, 1958; Bacon *et al.*, 1980; Ting, 1992; Yin *et al.*, 2010; Li *et al.*, 2011).

The first step in this formalism involves solving an eigenvalue problem for the matrix $\boldsymbol{N}$, which is constructed from the elastic constants and the crystallographic orientation. Specifically, the eigenvalue problem is expressed as:

$$\boldsymbol{N}\boldsymbol{\xi}^{\boldsymbol{\alpha}} = p_\alpha \boldsymbol{\xi}^{\boldsymbol{\alpha}} \tag{3.2}$$

In this equation, p_α denotes the six eigenvalues of the matrix $\boldsymbol{N}$. The matrix $\boldsymbol{N}$ itself is a 6×6 matrix, constructed from the stiffness tensor $\boldsymbol{C}$ and related to the orientation of the material through the vector $\boldsymbol{n}$ which is the unit normal to the indentation surface in the crystal's coordinate system and the vector $\boldsymbol{m} = \boldsymbol{n} \wedge \boldsymbol{t}$ with $\boldsymbol{t}$ being an arbitrary unit vector in the plane perpendicular to $\boldsymbol{n}$. It is recalled that $\boldsymbol{C}$ is included in the notation $(mn)_{jk} = m_i C_{ijkl} n_l$. The explicit form of $\boldsymbol{N}$ is given by:

$$\boldsymbol{N} = -\begin{bmatrix} (\boldsymbol{nn})^{-1}(\boldsymbol{nm}) & (\boldsymbol{nn})^{-1} \\ (\boldsymbol{mn})(\boldsymbol{nn})^{-1}(\boldsymbol{nm}) - (\boldsymbol{mm}) & (\boldsymbol{mn})(\boldsymbol{nn})^{-1} \end{bmatrix} \tag{3.3}$$

The matrix $\boldsymbol{N}$ contains the elastic information of the system and is responsible for capturing the anisotropic nature of the material. The six eigenvalues p_α appear as three pairs of complex conjugate numbers (Stroh, 1958; Bacon *et al.*, 1980; Ting, 1992; Yin *et al.*, 2010). By convention, these are labeled such that $p_{i+3} = \overline{p}_i$ and the imaginary part of p_i is positive, i.e., $\mathrm{Im}(p_i) > 0$ for $i =$ 1 to 3. This convention ensures that the eigenvalues are correctly ordered for further calculations. The eigenvectors associated with each eigenvalue are denoted by $\boldsymbol{\xi}^{\boldsymbol{\alpha}}$, and each eigenvector is split into two 3×1 column vectors as:

$$\boldsymbol{\xi}^{\boldsymbol{\alpha}} = \begin{bmatrix} \boldsymbol{A}^{\boldsymbol{\alpha}} \\ \boldsymbol{L}^{\boldsymbol{\alpha}} \end{bmatrix} \tag{3.4}$$

Here, $\boldsymbol{A}^{\boldsymbol{\alpha}}$ and $\boldsymbol{L}^{\boldsymbol{\alpha}}$ represent the components of the eigenvector that are related to the displacement and traction fields, respectively (Ting, 1992). The vectors $\boldsymbol{A}^{\boldsymbol{\alpha}}$ and $\boldsymbol{L}^{\boldsymbol{\alpha}}$ must satisfy a normalization condition, given by:

$$\sum_{i=1}^{3} A_i^\alpha L_i^\beta + A_i^\beta L_i^\alpha = \delta_{\alpha\beta} \tag{3.5}$$

This normalization ensures that the eigenvectors form a complete and orthonormal basis for the solution of the elastic problem. The matrix $\boldsymbol{B}$, which is central to the computation of E^*, can

then be constructed using the following relation:

$$B_{ij} = 2i \sum_{\alpha=1}^{3} L_{i\alpha} L_{j\alpha} \tag{3.6}$$

The matrix $\boldsymbol{B}$ (cf. Eq. 1.40) is thus expressed in terms of the eigenvalues and eigenvectors of the matrix $\boldsymbol{N}$, making the computation of E^* more efficient than evaluating the line integral of Eq.1.41.

3.3 Use of the Vlassak and Nix model for non-circular contact area

The framework used by Vlassak and Nix is rigorously valid for a circular contact area, a condition that holds true for spherical indenters in high-symmetry surfaces like (111) or (100) planes in cubic crystals (Vlassak *et al.*, 1993; Vlassak *et al.*, 1994; Vlassak *et al.*, 2003). For other orientations, the contact area tends to deviate from circular to elliptic due to the anisotropic response of the material to the indenter. The deviation of the contact area from perfect circularity introduces minor variations in the calculated E^* values. These variations, while present, remain small compared to the typical experimental scatter observed in nanoindentation tests. As a result, Eq. 1.40 remains an excellent approximation for evaluating E^*, even in cases where the contact area is slightly elliptical. The robustness of this approximation is a significant advantage, as it allows for a wide range of surface orientations to be probed without the need for complex geometric corrections. The ability to use a spherical indenter across different material orientations with minimal error makes this approach versatile in experimental practice.

For indenters with non-spherical geometries, such as the commonly used Berkovich tip, the situation becomes more complex. The triangular shape of the Berkovich tip introduces a dependency of E^* on the orientation of the indenter with respect to the surface being tested. This orientation sensitivity arises because the Berkovich tip lacks the rotational symmetry of a spherical indenter, resulting in an uneven stress distribution at the contact interface. Vlassak and Nix (Vlassak *et al.*, 1994) investigated this effect and showed that while the variations in E^* with orientation are

measurable, they are generally small and fall within the experimental scatter. Therefore, these variations can be reasonably neglected in many practical situations, particularly when dealing with large datasets where statistical averaging can mitigate orientation effects. However, Vlassak and Nix also observed that, on average, the indentation modulus obtained using a Berkovich tip is approximately 6 % higher than that obtained with an axisymmetric indenter (Vlassak *et al.*, 1994). This systematic difference arises from the geometry of the tip itself, which generates a slightly higher stress concentration at the contact point. To account for this known difference, a corrective factor of 1.06 is applied in this work to the values of E^* obtained with a Berkovich tip. This adjustment aligns with the approach used by Aspinall et al. (Aspinall *et al.*, 2022), ensuring consistency between the results obtained with different indenter geometries. The use of such corrective factors is common in the field of nanoindentation, where slight discrepancies between theoretical models and experimental data can be addressed by empirical adjustments. By applying the 1.06 factor, we ensure that the values of E^* obtained in this study are directly comparable to those obtained using spherical indenters or in other studies that use a similar correction.

3.4 Utilization of Gauss-Legendre Quadrature for Time Efficiency Enhancement

A Gauss-Legendre quadrature method (Abramowitz *et al.*, 1968; Winckel, 2004) has been chosen to solve the line integral in Eq.1.40 in order to obtain a high degree of precision and computational efficiency. The convergence behavior of the computational model for calculating the anisotropic modulus E^* using Gauss-Legendre quadrature is now examined. The primary objective is to determine the number of iterations required for the model to stabilize at an accurate estimate of E^* across different crystallographic orientations, represented here by two distinct crystallographic orientations. This convergence analysis not only helps in assessing the efficiency of the Gauss-Legendre quadrature method but also ensures that the code performs reliably within acceptable error margins for various orientations.

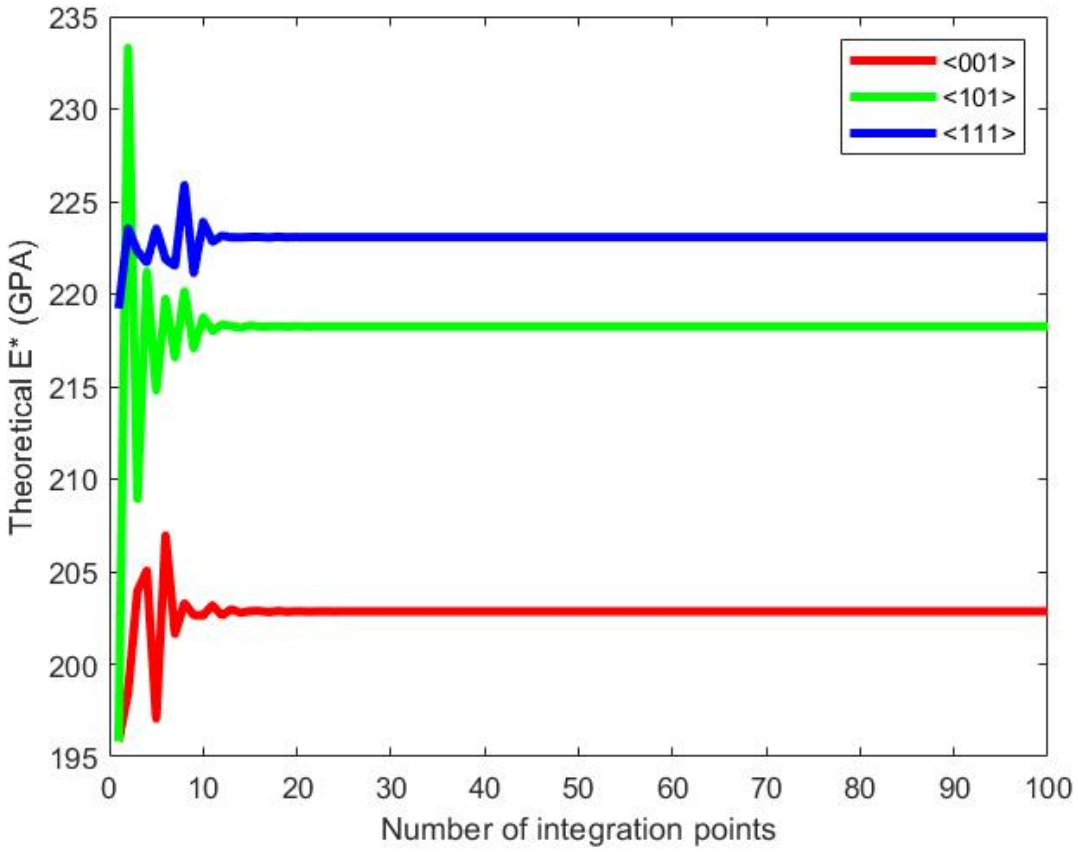

Figure 3.1: Evolution of the value of E^* with the number of integration points of the Gauss-Legendre quadrature method for the principal oriantations $< 001 >$, $< 101 >$, and $< 111 >$.

Figure 3.1 shows the very rapid stabilization of the theoretical E^* for the principal orientations $< 001 >$, $< 101 >$, and $< 111 >$ when increasing the number of integration points. In all the cases, the modulus values exhibit a rapid convergence within fifteen integration points, indicating that the Gauss-Legendre quadrature method efficiently approximates the integral, with a computation time of less than one second per modulus. Notably, the $< 111 >$ orientation converges to a value around 223 GPa, while the $< 101 >$ orientation stabilizes near 218 GPa, and the $< 001 >$ orientation tends to 202 GPa. This disparity between the grains reflects the impact of crystallographic orientation on the computed modulus, aligning with the anisotropic nature of the material. The swift convergence observed here suggests that Gauss-Legendre quadrature is effective in reducing computational time while maintaining precision.

To quantify the accuracy of the method, Figures 3.2 and 3.3 presents the variation of the relative error with the number of integration points, considering a reference value of E^* at 100 integration

points. The error also quickly approaches zero within the first 15 integration points, highlighting the method's precision. all orientations exhibit a rapid reduction in error, with values becoming negligible after approximately ten integration points. This pattern underscores the robustness of the Gauss-Legendre quadrature approach, as it enables the model to reach a steady state without requiring extensive computational effort. The minimization of error further validates the choice of this quadrature technique.

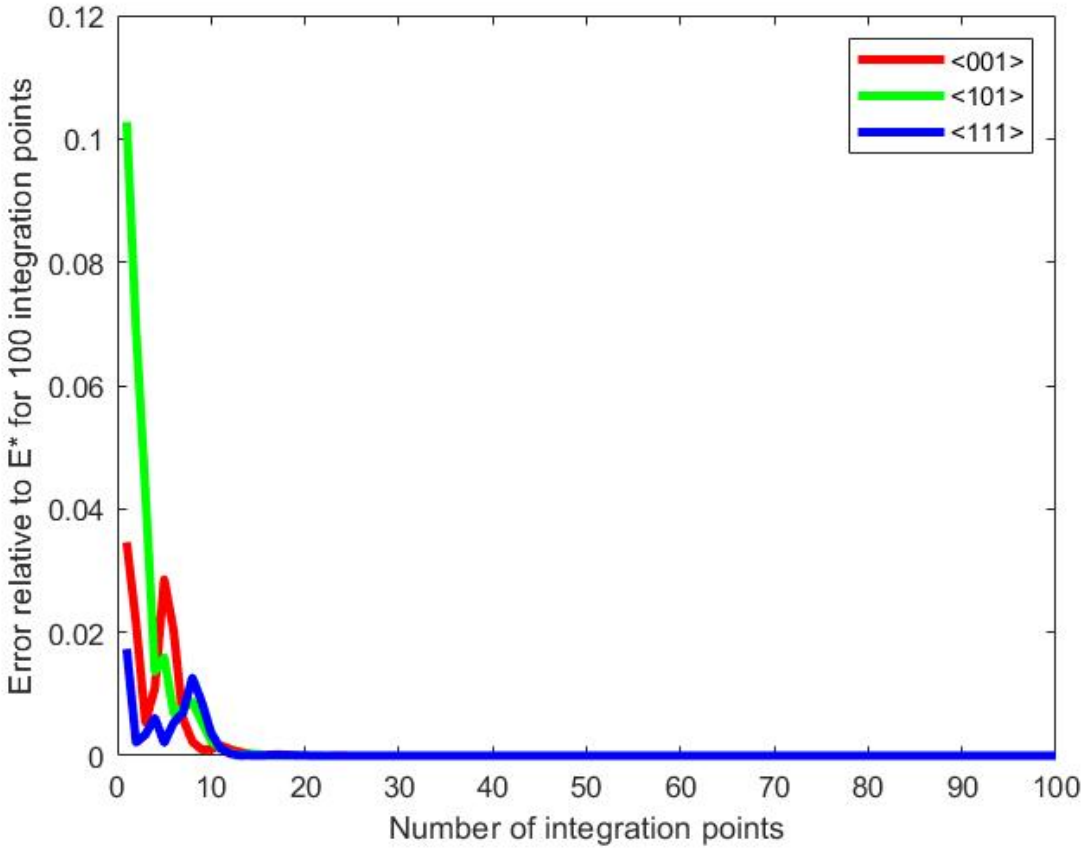

Figure 3.2: Relative error made on the evaluation of E^* with the number of integration points. The reference value is considered at 100 integration points.

Hence, by utilizing only 15 integration points, the Gauss-Legendre quadrature method achieves an impressive accuracy of 10^{-4}, ensuring that even the smallest discrepancies in the calculation are minimized. This level of precision is particularly important when dealing with complex cases, as small variations can significantly impact the resulting modulus values. Finally, it is emphasized that the computation of E^* with 15 integration points, and in combination with the matrix formalism, is achieved in a negligible time, well below one second ($\ll 1\,\mathrm{s}$).

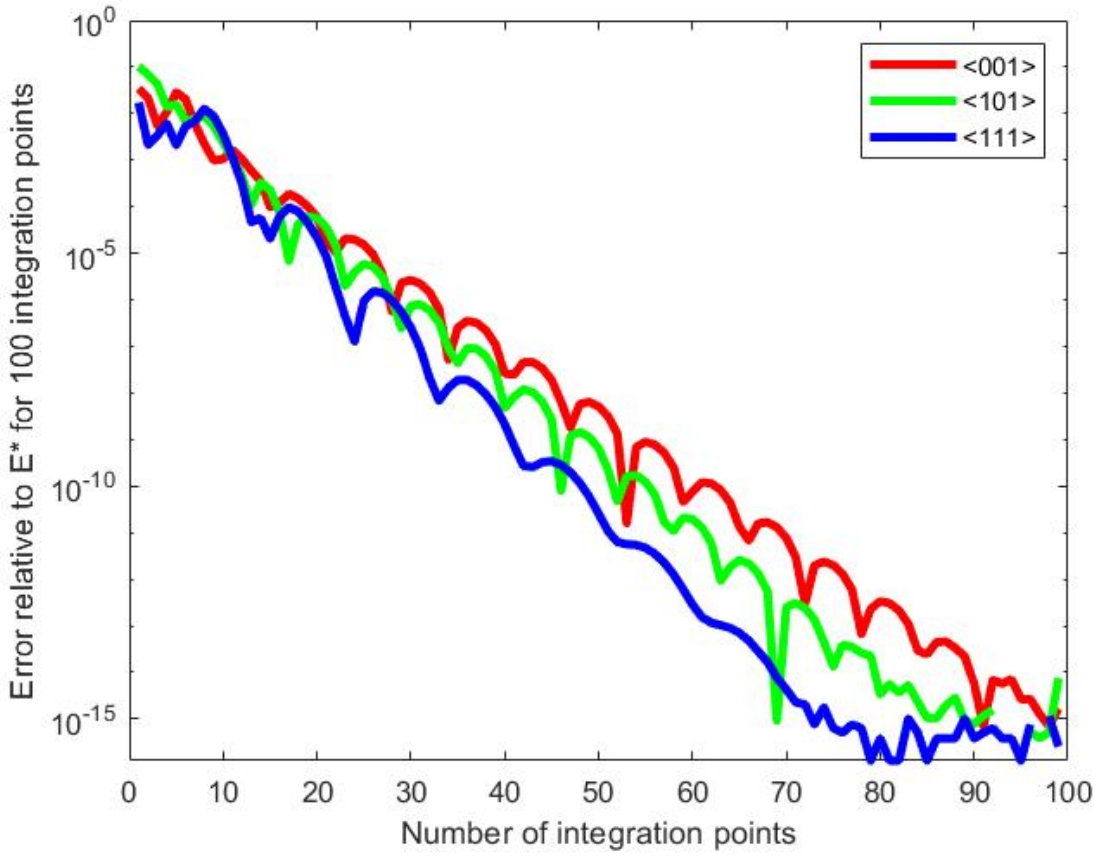

Figure 3.3: Relative error in the logarithmic scale made on the evaluation of E^* with the number of integration points. The reference value is considered at 100 integration points.

3.5 Comparisons of Orientation Dependence of E^* and $E^{(hkl)}$

Using the Vlassak and Nix model, alongside elastic constants from the literature, it is possible to generate an inverse pole figure (IPF) of the theoretical E^*. This IPF serves as a valuable tool for visualizing the directional dependence of the elastic properties and helps in selecting optimal orientations for nanoindentation experiments. By plotting the IPF, we can identify regions of the crystal lattice that exhibit distinct mechanical responses, which allows for a more comprehensive understanding of the material's anisotropy. This approach is particularly useful when attempting to cover a wide range of crystallographic orientations in a systematic manner, ensuring that the full spectrum of anisotropic behavior is captured.

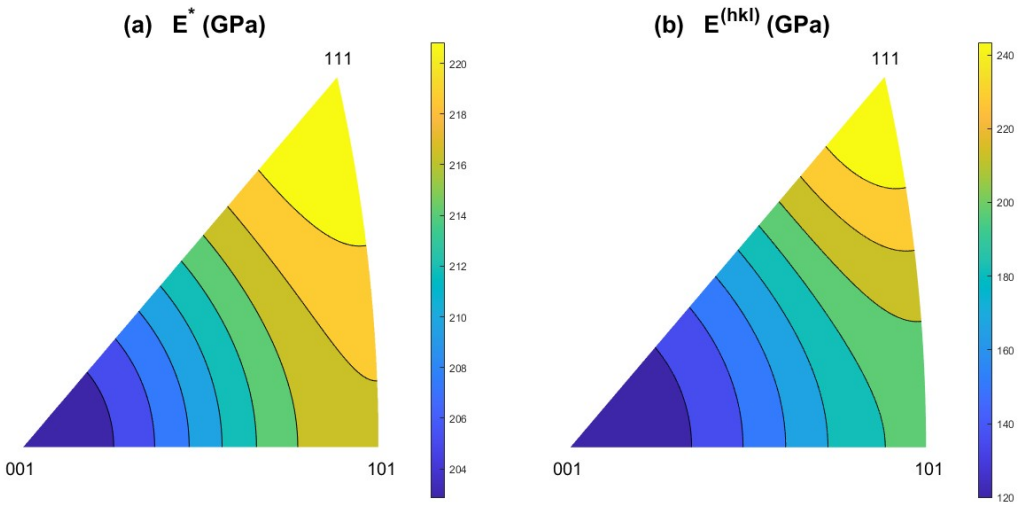

Figure 3.4: IPF contour along the indentation direction of (a) E^* using the Vlassak and Nix model and (b) of the directional Young's modulus along the indentation axis $E^{(hkl)}$. The Ni cubic elastic constants of Yamamoto, 1950 were used: $C_{11} = 244\,\text{GPa}$, $C_{12} = 158\,\text{GPa}$ and $C_{44} = 102\,\text{GPa}$.

Additionally, the IPF of the directional Young's modulus $E^{(hkl)}$ (cf. Eq. 1.37) along the indentation axis is plotted to highlight the differences between $E^{(hkl)}$ and E^*. It is important to note that these two quantities, while related, describe different aspects of the material's elastic response. In some studies, confusion between $E^{(hkl)}$ and E^* has led to misinterpretations of experimental data. The most striking observation from the IPF comparison is the narrower range of values exhibited by E^* compared to $E^{(hkl)}$. For high-purity Nickel, while the maximum value of $E^{(hkl)}$ can exceed twice the minimum value, indicating a significant degree of anisotropy, the corresponding range for E^* is much smaller, with the maximum value being only about 10% higher than the minimum. This restricted range of E^* is a reflection of how the effective modulus integrates over the contact area, averaging out much of the anisotropy that is more pronounced in the directional Young's modulus.

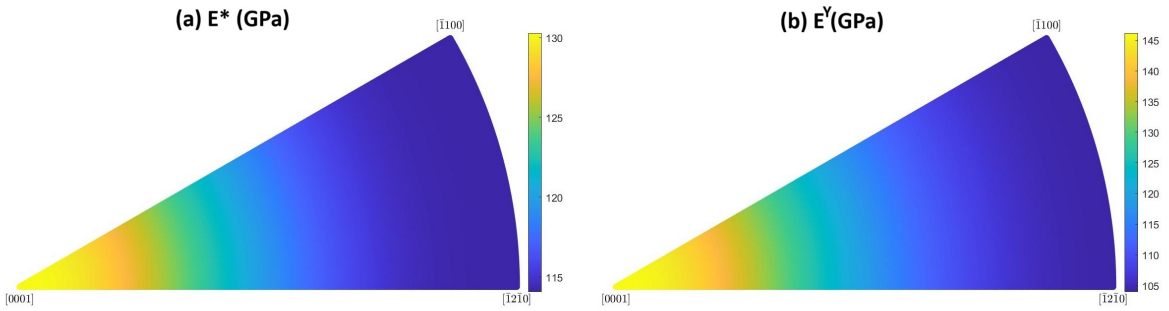

Figure 3.5: IPF contour along the indentation direction of (a) E^* using the Vlassak and Nix model adapted for HCP symmetry and (b) of the directional Young's modulus along the indentation axis $E^{(hkl)}$. The HCP elastic constants used are: $C_{11} = 160\,\text{GPa}$, $C_{12} = 90\,\text{GPa}$, $C_{13} = 66\,\text{GPa}$, $C_{33} = 181\,\text{GPa}$, $C_{44} = 46.5\,\text{GPa}$, and $C_{66} = 35\,\text{GPa}$.

The same has been done for Hexagonal close-packed symmetry materials as shown in Fig. 3.5 by adapting the Vlassak and Nix's model used in the cubic case. While the range differences, and therefore the anisotropy, are not as pronounced in this case, the $E^{(hkl)}$ range remains wider than the E^* one, highlighting once again the distinct nature of each moduli.

3.6 Case Studies and Model Validation

We are now going to present a series of case studies designed to evaluate the performance and robustness of the computational framework developed for calculating the anisotropic modulus E^*. Using the theoretical model in matrix formalism established by Vlassak and Nix, we apply the code to different crystallographic orientations and materials with known elastic constants to examine its response across a variety of scenarios. These studies enable a systematic assessment of the model's predictive accuracy when applied to real-world experimental conditions. By exploring a range of material anisotropies, we gain insights into how variations in elastic constants, crystallographic orientation, and contact geometry influence the computed modulus.

Through each case study, we aim to quantify the code's sensitivity to input parameters. This approach not only validates the theoretical assumptions underpinning the Vlassak and Nix model but also highlights the practical considerations necessary for interpreting anisotropic elastic responses in nanoindentation. Ultimately, these case studies serve to bridge the gap between theoretical

predictions and experimental application, offering a practical framework for further investigation into the mechanical behavior of anisotropic materials.

3.6.1 The case of Cubic Elastic Symmetry

In the crystal's coordinates system and using Voigt notation, the cubic compliance matrix $\boldsymbol{S}$ writes classically as:

$$\boldsymbol{S} = \begin{bmatrix} S_{11} & S_{12} & S_{12} & 0 & 0 & 0 \\ S_{12} & S_{11} & S_{12} & 0 & 0 & 0 \\ S_{12} & S_{12} & S_{11} & 0 & 0 & 0 \\ 0 & 0 & 0 & S_{44} & 0 & 0 \\ 0 & 0 & 0 & 0 & S_{44} & 0 \\ 0 & 0 & 0 & 0 & 0 & S_{44} \end{bmatrix} \tag{3.7}$$

Considering a uniaxial test along the $\langle 100 \rangle$ crystallographic direction and a linear elastic generalized Hooke's law, we have then:

$$\varepsilon_1 = S_{11}\sigma_1 \text{ and } \varepsilon_2 = S_{12}\sigma_1 \tag{3.8}$$

By definition, the $\langle 100 \rangle$ Young's modulus and the the $\langle 100 \rangle$ Poisson's ratio are given by:

$$E_{\langle 100 \rangle} = \frac{\sigma_1}{\varepsilon_1} = \frac{1}{S_{11}} \text{ and } \nu_{\langle 100 \rangle} = -\frac{\varepsilon_2}{\varepsilon_1} = -\frac{S_{12}}{S_{11}} \tag{3.9}$$

In addition, the Zener ratio A is defined as the ratio of $\mu^{''}$ over $\mu^{'}$, the $\{001\}\langle 100 \rangle$ and $\{001\}\langle 110 \rangle$ shear resistances of the crystal (cf. Eq. 1.5):

$$\begin{aligned} A &= \frac{\mu^{''}}{\mu^{'}} \\ \text{with } \mu^{'} &= \frac{1}{2(S_{11} - S_{12})} \text{ and } \mu^{''} = \frac{1}{S_{44}} \end{aligned} \tag{3.10}$$

From these definitions, we can re-write $\boldsymbol{S}$ as:

$$\boldsymbol{S} = \frac{1}{E_{\langle 100\rangle}} \begin{bmatrix} 1 & -\nu_{\langle 100\rangle} & -\nu_{\langle 100\rangle} & 0 & 0 & 0 \\ -\nu_{\langle 100\rangle} & 1 & -\nu_{\langle 100\rangle} & 0 & 0 & 0 \\ -\nu_{\langle 100\rangle} & -\nu_{\langle 100\rangle} & 1 & 0 & 0 & 0 \\ 0 & 0 & 0 & \frac{2(1+\nu_{\langle 100\rangle})}{A} & 0 & 0 \\ 0 & 0 & 0 & 0 & \frac{2(1+\nu_{\langle 100\rangle})}{A} & 0 \\ 0 & 0 & 0 & 0 & 0 & \frac{2(1+\nu_{\langle 100\rangle})}{A} \end{bmatrix} \tag{3.11}$$

since $\mu^{'} = \dfrac{E_{\langle 100\rangle}}{2(1+\nu_{\langle 100\rangle})}$. By inverting $\boldsymbol{S}$, the expression of for the cubic stiffness matrix $\boldsymbol{C}$ is finally obtained:

$$\boldsymbol{C} = \frac{E_{\langle 100\rangle}}{\left(1+\nu_{\langle 100\rangle}\right)\left(1-2\nu_{\langle 100\rangle}\right)} \times \begin{bmatrix} 1-\nu_{\langle 100\rangle} & \nu_{\langle 100\rangle} & \nu_{\langle 100\rangle} & 0 & 0 & 0 \\ \nu_{\langle 100\rangle} & 1-\nu_{\langle 100\rangle} & \nu_{\langle 100\rangle} & 0 & 0 & 0 \\ \nu_{\langle 100\rangle} & \nu_{\langle 100\rangle} & 1-\nu_{\langle 100\rangle} & 0 & 0 & 0 \\ 0 & 0 & 0 & A\frac{1-2\nu_{\langle 100\rangle}}{2} & 0 & 0 \\ 0 & 0 & 0 & 0 & A\frac{1-2\nu_{\langle 100\rangle}}{2} & 0 \\ 0 & 0 & 0 & 0 & 0 & A\frac{1-2\nu_{\langle 100\rangle}}{2} \end{bmatrix} \tag{3.12}$$

3.6.2 Influence of Shear Moduli on E^*

The first case study investigates the sensitivity of the theoretical anisotropic modulus E^* to variations in shear resistances $\mu^{'}$ and $\mu^{''}$ for the principal orientations $< 001 >$, $< 101 >$, and $< 111 >$. The objective is to understand how changes in these shear moduli, which are indicative of the material's resistance to deformation under shear stress, impact the computed E^*. Figures 3.6 and 3.7 enable a comparative analysis of anisotropic responses across different crystallographic orientations across the principal orientations $< 001 >$, $< 101 >$, and $< 111 >$.

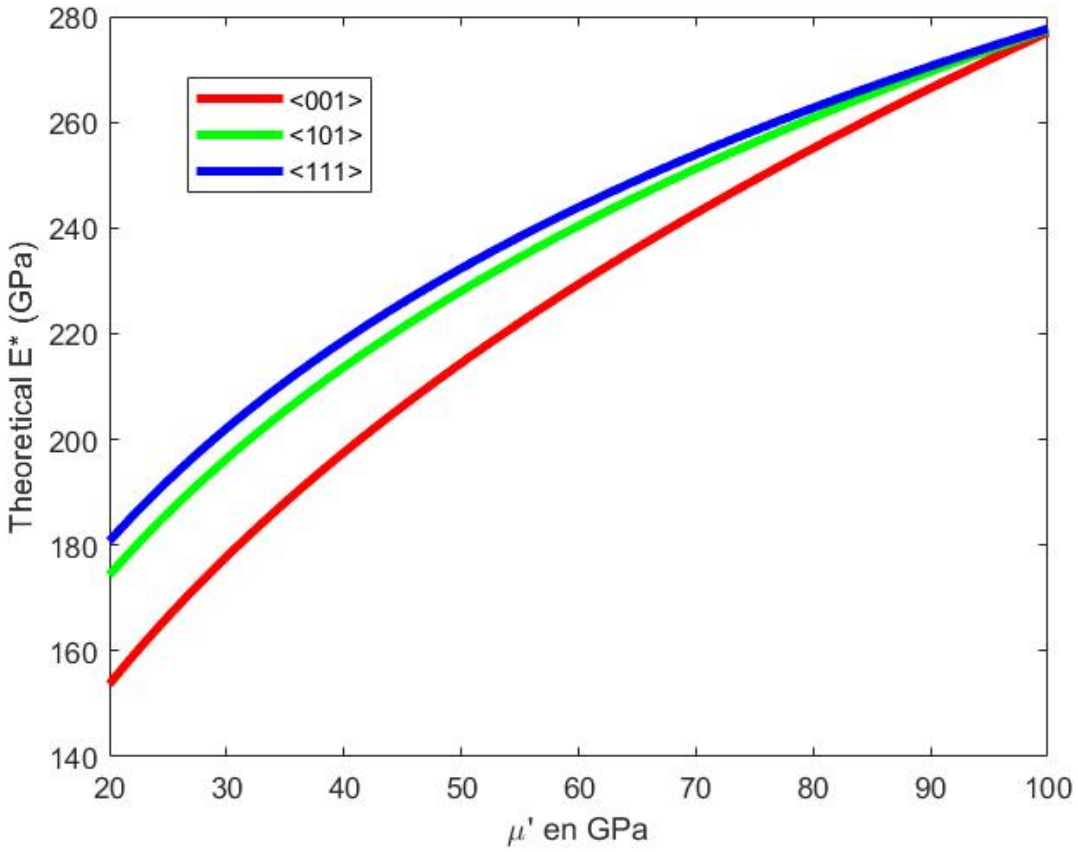

Figure 3.6: Variation of the theoretical E^* (in GPa) with $\mu^{'}$, computed for the $<\ 001\ >$, $<\ 101\ >$, and $<\ 111\ >$ cubic crystallographic orientations (for $\mu^{''} = 102GPa$).

Figure 3.6 demonstrates the dependency of E^* on $\mu^{'}$, showing a clear upward trend as $\mu^{'}$ increases from 20 to 100 GPa. For all orientations orientations, the theoretical modulus E^* rises proportionally with $\mu^{'}$, though there is a notable difference in the absolute values of the E^* of the orientation. Orientations $< 111 >$ and $< 101 >$ consistently exhibits higher E^* values while $< 001 >$ exhibits the lowest (as seen in Fig. 3.4). The spread of the values diminishes when the value of $\mu^{'}$ approaches the fixed value of $\mu^{''}$ at 102 GPa. Indeed, when $\mu^{'} = \mu^{''}$, the isotropic case is retrieved and the value of E^* is independent of the orientation.

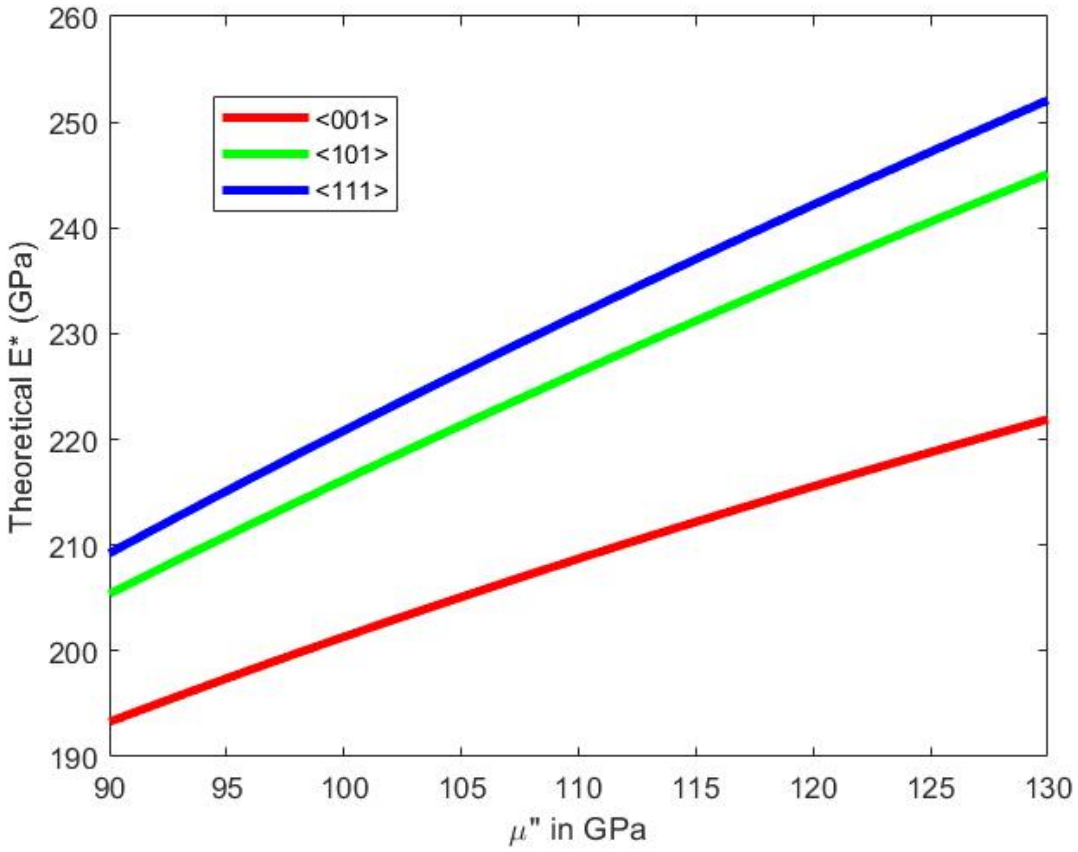

Figure 3.7: Variation of the theoretical E^* (in GPa) with $\mu^{''}$, computed for the $<\ 001\ >$, $<\ 101\ >$, and $<\ 111\ >$ cubic crystallographic orientations (for $\mu^{'} = 43GPa$).

Figure 3.7 extends the analysis by exploring the relationship between E^* and the second shear resistance $\mu^{''}$. Similar to the trends observed with $\mu^{'}$, E^* increases linearly with $\mu^{''}$ for all orientations. All three orientations have the same response through the whole, even if increase in the values of E^* for the $< 001 >$ orientation seems to be at a lower rate than for orientations $< 101 >$ and $< 111 >$. This distinct behavior between orientation underlines the complex interplay between shear resistances and orientation in determining the effective modulus.

The findings from this case study underscore the importance of accurately characterizing both $\mu^{'}$ and $\mu^{''}$ when estimating E^* in anisotropic materials. Small variations in these shear resistances lead to noticeable changes in the computed modulus, particularly for orientations that are more sensitive to shear stresses. By isolating the effects of $\mu^{'}$ and $\mu^{''}$, this study contributes valuable insights into how anisotropy affects the elastic response of materials.

3.6.3 Dependence of E^* on A, $\nu_{\langle 100\rangle}$ and $E_{\langle 100\rangle}$

In the second case study, we explore the influence of the anisotropy factor A, the directional Poisson's ratio $\nu_{\langle 100\rangle}$, and the directional Young's Modulus $E_{\langle 100\rangle}$ on the theoretical anisotropic modulus E^* for the principal orientations $< 001 >$, $< 101 >$, and $< 111 >$. The anisotropy factor, A, characterizes the deviation from isotropy in a material's elastic response, while $\nu_{\langle 100\rangle}$ reflects the ratio of lateral to axial strain. Understanding how E^* varies with these parameters is essential for tailoring nanoindentation experiments to account for material anisotropy accurately. Figures (3.8, 3.9, and 3.10) depict the response of E^* to changes in A, $\nu_{\langle 100\rangle}$, and $E_{\langle 100\rangle}$ for the principal orientations $< 001 >$, $< 101 >$, and $< 111 >$, illustrating the nuanced impact of each parameter on the modulus.

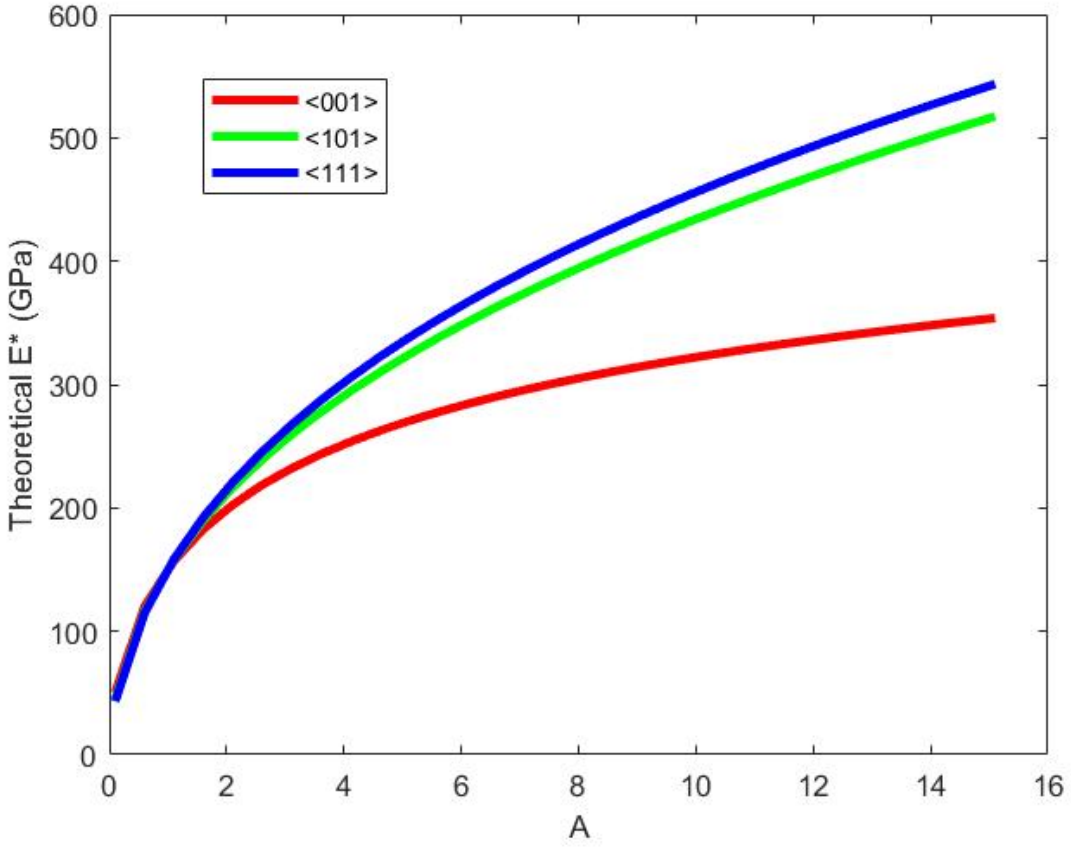

Figure 3.8: Variation of the theoretical E^* (in GPa) with A, computed for the $< 001 >$, $< 101 >$, and $< 111 >$ cubic crystallograpic orientations (for $\nu_{\langle 100\rangle} = 0.37$ and $E_{\langle 100\rangle} = 130GPa$).

As shown in Figure 3.8, E^* exhibits a nonlinear increase with rising values of A, particularly for

smaller values of A. Starting from the isotropic case where $A = 1$ all orientations display a similar trend, with orientation $< 111 >$ consistently yielding the highest E^* values and $< 001 >$ the lowest ones. This behavior suggests that increasing anisotropy, as indicated by a higher A, enhances the material's effective modulus in the indentation direction. However, the rate of increase in E^* diminishes as A grows, approaching a plateau, which implies that beyond a certain point, further increases in anisotropy have a limited effect on the indentation modulus.

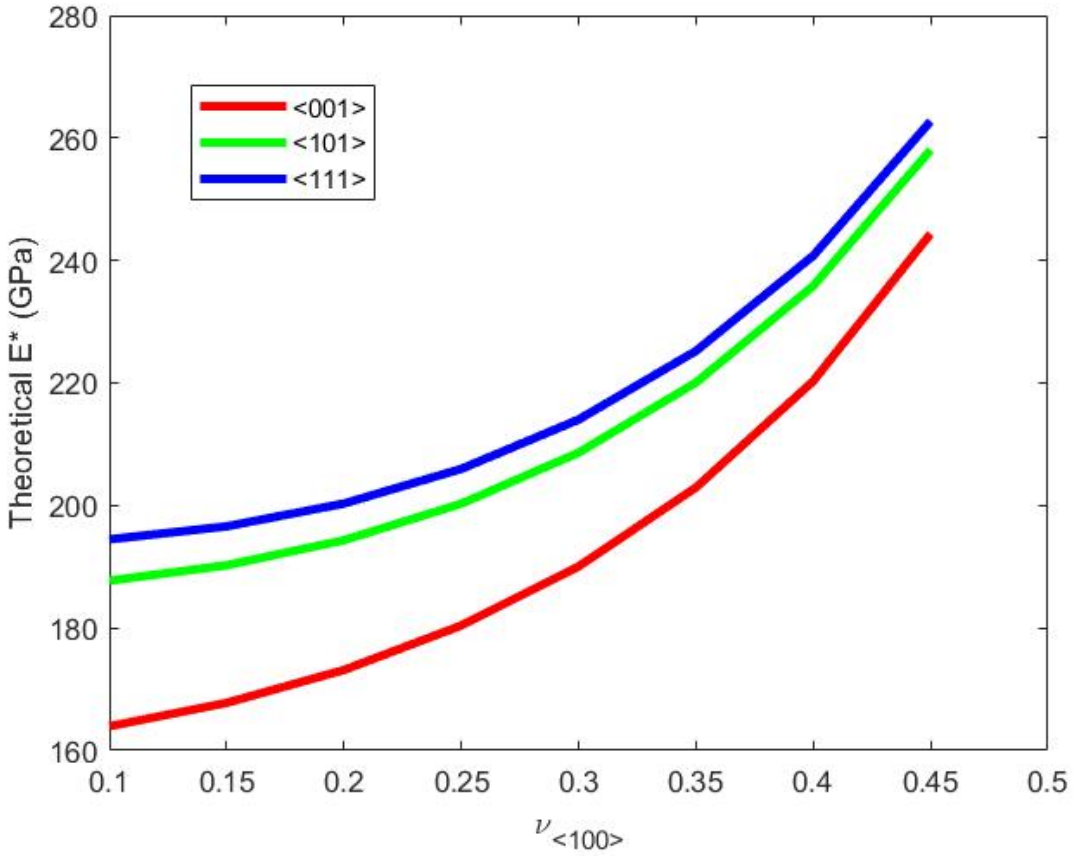

Figure 3.9: Variation of the theoretical E^* (in GPa) with $\nu_{\langle 100 \rangle}$, computed for the $< 001 >$, $< 101 >$, and $< 111 >$ cubic crystallograpic orientations (for $A = 2.3$ and $E_{\langle 100 \rangle} = 130GPa$).

Figure 3.9 demonstrates the relationship between E^* and $\nu_{\langle 100 \rangle}$, revealing a more pronounced impact on the modulus as $\nu_{\langle 100 \rangle}$ approaches higher values. For all orientations, E^* initially shows a mild increase as $\nu_{\langle 100 \rangle}$ rises from 0.1, but the slope steepens significantly around 0.3, suggesting an amplified elastic response at higher $\nu_{\langle 100 \rangle}$. This increase aligns with the material's greater tendency to resist deformation under shear when $\nu_{\langle 100 \rangle}$ is higher, contributing to an elevated effective modulus.

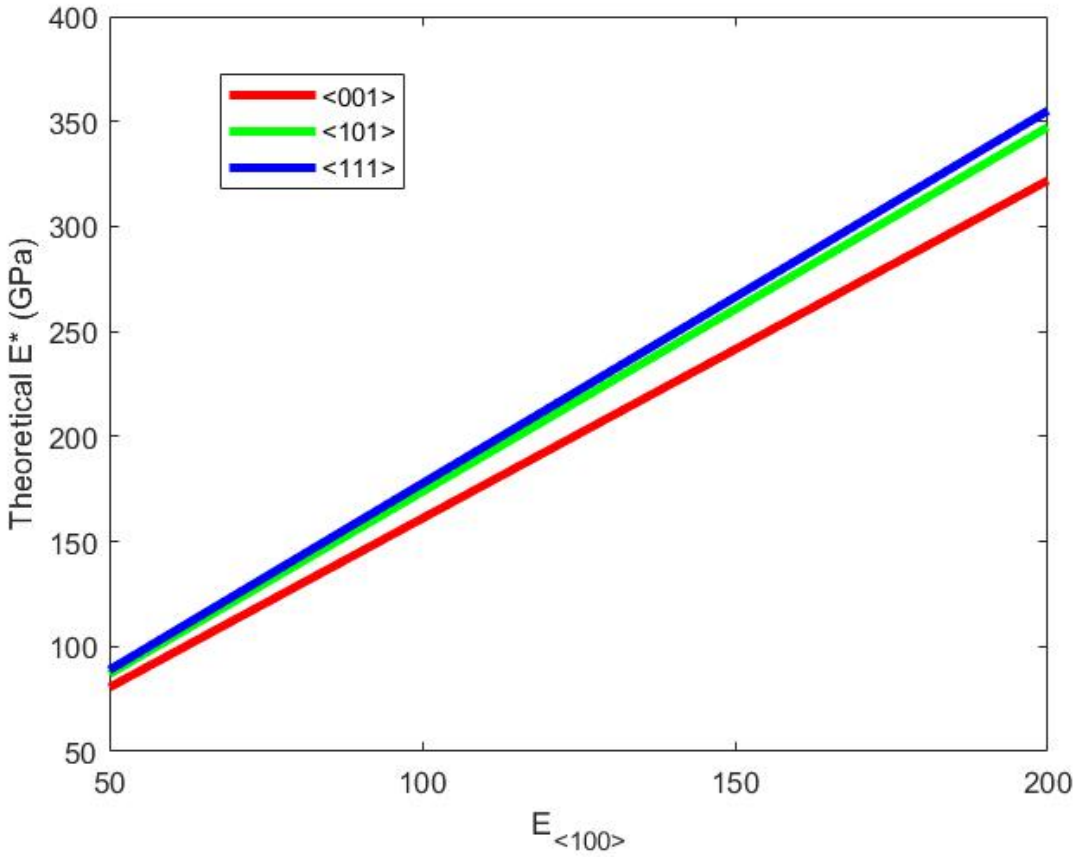

Figure 3.10: Variation of the theoretical E^* (in GPa) with $E_{\langle 100\rangle}$, computed for the $< 001 >$, $< 101 >$, and $< 111 >$ cubic crystallograpic orientations (for $A = 2.3$ and $\nu_{\langle 100\rangle} = 0.37$).

Figure 3.10 shows the relationship between E^* and the directional Young's modulus $E_{\langle 100\rangle}$, illustrating, as expected, a linear relationship between the two properties across the examined range. Despite the close grouping of the three principal orientations $< 001 >$, $< 101 >$, and $< 111 >$, a minor variations in their slope is evident, with $< 111 >$ the highest slope and $< 001 >$ the lowest one.

The comparative analysis of these three parameters—anisotropy factor A, $\nu_{\langle 100\rangle}$, and $E_{\langle 100\rangle}$—highlights the complex interplay between material anisotropy and elastic behavior under indentation. While all the parameters influence E^*, their effects manifest differently: A primarily impacts the modulus at lower values before reaching a plateau, whereas $\nu_{\langle 100\rangle}$ induces a steady increase in E^* that accelerates with higher values. The observed trends further validate the computational approach, demonstrating its effectiveness in capturing subtle variations in E^* due to anisotropy and material-specific parameters.

3.7 Conclusion

This chapter presented an efficient framework for calculating the anisotropic modulus E^* using the Vlassak and Nix model. By employing the Stroh matrix formalism and Gauss-Legendre quadrature, we achieved a computationally streamlined method that provides accurate results across various orientations with minimal error. This efficiency is crucial for experiments involving multiple orientations and use of the Vlassak and Nix model within a Bayesian inference procedure, allowing rapid data generation and consistent alignment with experimental conditions.

Case studies demonstrated the model's robustness in accounting for variations in shear moduli, anisotropy factors, $\nu_{\langle 100 \rangle}$, and $E_{\langle 100 \rangle}$, underscoring the influence of crystallographic orientation on E^*. Results confirmed that the model captures essential aspects of anisotropic elasticity, with material properties like the anisotropy factor A, $\nu_{\langle 100 \rangle}$, and $E_{\langle 100 \rangle}$ shaping the modulus distinctively across orientations. In summary, this chapter offers a practical and validated approach for calculating E^* in anisotropic materials, bridging theoretical and experimental insights into material elasticity.

Chapter 4

Bayesian Inference

4.1 Introduction

Bayesian inference has emerged as a powerful statistical tool in the field of materials science, offering a robust framework for estimating material parameters while accounting for uncertainties inherent in experimental data. Unlike traditional deterministic approaches, Bayesian inference integrates prior knowledge with experimental observations, allowing for the continual refinement of estimates as new data becomes available. This makes it particularly well-suited for the estimation of single-crystal elastic constants (SECs), where variability in experimental measurements can significantly influence the results.

In the context of this research, Bayesian inference is employed to refine the estimation of elastic constants from nanoindentation data. By integrating the Vlassak and Nix model with Bayesian statistical methods, we are able to not only estimate the SECs of cubic materials but also quantify the uncertainties associated with these estimates. This approach is especially advantageous given the challenges associated with characterizing the elastic properties of anisotropic and multiphase materials.

This chapter will first introduce the fundamental principles of Bayesian inference and discuss its application to the identification of material parameters. We will then detail the implementation of an original Bayesian method for our study, including the development of the likelihood functions and the incorporation of prior knowledge based on existing literature and experimental data. The

chapter will also explore how the Bayesian framework allows for the efficient use of computational resources by narrowing the parameter space and reducing the number of simulations needed to converge on a solution.

In conclusion, this chapter sets the stage for the subsequent presentation of results by establishing the theoretical and computational foundation of the Bayesian inference approach used in this work. The integration of nanoindentation experiments with Bayesian statistics not only improves the accuracy of SEC estimations but also provides a deeper understanding of the material properties by accounting for experimental variability and uncertainty.

4.2 Integration of Vlassak and Nix Model with Bayesian Inference

From the newly defined notation of $\boldsymbol{C}$ according to Eq. 3.12, it becomes clear that ratios of E^* computed from Eq. 1.40 depend on only two dimensionless elastic parameters which can be taken as A and $\nu_{\langle 100 \rangle}$. This finding proves to be very useful when performing Bayesian inference. As a matter of fact, the computation time is greatly reduced by varying 2 parameters instead of 3. In addition, from Born's elastic stability conditions, the limits of $\nu_{\langle 100 \rangle}$ and the lower limit of A are well-known and material's independent: $0 < \nu_{\langle 100 \rangle} < 0.5$ and $A > 0$ whereas the upper limit of A can be easily conjectured ($A < 15$) or adjusted rapidly if necessary on the basis of a first Bayesian simulation. On the contrary, the bounds of the C_{ij} constants for an unknown material are far much harder to estimate a priori (Purohit *et al.*, 2021). Hence, the present approach presents a huge advantage compared to classical ones which necessitate several Bayesian simulations just to define the correct bounds of a given material. On top of that, the use of ratios increases the number of input data: $n\left(n-1\right)/2$ independent ratios for n values of E^* and also mitigates the influence of the various parameters needed to be calibrated for a nanoindentation test, such as the projected contact area function. Indeed, considering two measurements (1) and (2) at a same contact depth, the ratio of indentation moduli can be expressed from Eqs. 1.19 and 1.36 as:

$$\frac{E^{*(1)}}{E^{*(2)}} = \frac{\dfrac{S^{(1)}}{S^{(2)}} - (1-\nu_i^2)\dfrac{E_{eff}^{(1)}}{E_i}}{1-(1-\nu_i^2)\dfrac{E_{eff}^{(1)}}{E_i}} \tag{4.1}$$

From this equation, it becomes clear that the ratios of indentation moduli depend mainly on the measured stiffness ratios $\frac{S^{(1)}}{S^{(2)}}$ while the influence of the geometrical parameter β and of the calibrated projected contact area A_p involved in the expression of the reduced modulus $E_{eff}^{(1)}$ (cf. Eq. 1.19) is negligible since $E_i \gg E_{eff}^{(1)}$.

In our Bayesian framework, Bayes' theorem (cf. Eq. 1.46) is thus applied as follows:

$$P\left(\left(A,\nu_{\langle 100\rangle}\right)|R^*\right) = \frac{P\left(R^*|\left(A,\nu_{\langle 100\rangle}\right)\right)P\left(\left(A,\nu_{\langle 100\rangle}\right)\right)}{P\left(R^*\right)} \tag{4.2}$$

R^* denotes the $m = n(n-1)/2$ independent ratios computed from the n experimental E^* values. A given ratio, denoted as R_j^i or R_k, is simply defined as:

$$R_k = R_j^i = \frac{E_i^*}{E_j^*} \tag{4.3}$$

For the Bayesian inference simulations, we consider only one average E_i^* value per grain. The corresponding standard-deviation is denoted $\sigma_{E_i^*}$. Considering a normal approximation, the standard-deviation of the ratio distribution can then be estimated as (Diaz-Francés *et al.*, 2013):

$$\sigma_{R_j^i} = \frac{E_i^*}{E_j^*}\sqrt{\frac{\sigma_{E_i^*}^2}{E_i^{*2}} + \frac{\sigma_{E_j^*}^2}{E_j^{*2}}} \tag{4.4}$$

In Eq. 4.2, $P\left(R^*|\left(A,\nu_{\langle 100\rangle}\right)\right)$ is the likelihood and stands for the probability of observing all the ratios R^* for a given couple $\left(A,\nu_{\langle 100\rangle}\right)$. It is computed as:

$$P\left(R^*|\left(A,\nu_{\langle 100\rangle}\right)\right) = \prod_{k=1}^{m} P\left(R_k|\left(A,\nu_{\langle 100\rangle}\right)\right) \tag{4.5}$$

It is noteworthy that log-probabilities are actually used in the computational framework for numerical stability. $P\left(R_k|\left(A,\nu_{\langle 100\rangle}\right)\right)$ is evaluated by comparing the experimental value of R_j^i to the ratio r_j^i obtained from the Vlassak and Nix's model (Eq. 1.40) considering the Euler angles of

the two grains and the tested values of A and $\nu_{\langle 100\rangle}$. Concretely, a normal distribution centered around R_j^i and of variance $\sigma_{R_j^i}^2$ is created while the interval $\left[0, 3\sigma_{R_j^i}\right]$ is discretized into 100 bins. The likelihood corresponds to the probability of the absolute difference $|r_j^i - R_j^i|$ to fall within a given bin. If $|r_j^i - R_j^i|$ does not fall within any of the created bins, then the likelihood corresponds to the probability of $|r_j^i - R_j^i|$ to be greater than $3\sigma_{R_j^i}$.

At the end of the Bayesian inference procedure, $P(R^*)$ serves as a normalization factor to come back from log-probabilities to the classical probabilities defined within the usual $[0, 1]$ interval. The procedure thus provides as an output $P\left(\left(A, \nu_{\langle 100\rangle}\right)|R^*\right)$ which is the probability distribution that the values of the couple $\left(A, \nu_{\langle 100\rangle}\right)$ are correct given the observations of the indentation modulus ratios R^*. From this posterior probability distribution, one can easily obtain, through summations, $P(A|R^*)$ the marginal probability distribution that the values of A are correct given the observations of R^*, as well as $P\left(\nu_{\langle 100\rangle}|R^*\right)$ the marginal probability distribution that the values of $\nu_{\langle 100\rangle}$ are correct given the observations of R^*.

On the other hand, the posterior probability distribution $P\left(E_{\langle 100\rangle}|R^*\right)$ can be obtained directly by simple allocations of the probabilities $P\left(\left(A, \nu_{\langle 100\rangle}\right)|R^*\right)$. The relevant value of $E_{\langle 100\rangle}$ which should be associated with a given couple $\left(A, \nu_{\langle 100\rangle}\right)$ can indeed be evaluated as the median of the ratios distribution between experimental indentation moduli E_i^* and normalized theoretical moduli. The latter are obtained, for each grain, from the Vlassak and Nix's model considering $E_{\langle 100\rangle} = 1$ and the tested couple $\left(A, \nu_{\langle 100\rangle}\right)$.

For both samples, no *a priori* knowledge is considered for the values of A and $\nu_{\langle 100\rangle}$. The range of A and $\nu_{\langle 100\rangle}$ values simply follows the Born's elastic stability conditions and the choice of a very high upper limit for A (15):

$$0 < A < 15 \text{ and } 0 < \nu_{\langle 100\rangle} < 0.5 \tag{4.6}$$

These broad ranges ensure that the simulations can explore a wide range of physically reasonable values for both A and $\nu_{<100>}$. In order to run the Bayesian simulations, evenly spaced values of A and $\nu_{\langle 100\rangle}$ within the above ranges are hence considered with the exact same total number of A and $\nu_{\langle 100\rangle}$ values. This procedure amounts to assume a uniform distribution for the prior belief

$P\left(\left(A, \nu_{\langle 100\rangle}\right)\right)$, reflecting a state of prior ignorance regarding the true values of A and $\nu_{<100>}$. This approach allows the experimental data to fully drive the inference process without imposing any preconceptions on the possible outcomes.

In addition to defining the prior distributions, it was also necessary to specify the values of the measurement uncertainties, denoted as $\sigma_{E_i^*}$. These uncertainties could, in principle, be estimated from the standard deviation of the measured indentation moduli within each grain. However, this approach does not account for other sources of uncertainty, such as those related to the EBSD measurements, to the linear approximation in the analysis of the oscillatory indentations (Cheng *et al.*, 2006) and to the tip and device calibrations which are fixed before performing the nanoindentation mapping. Furthermore, uncertainties related to the sample preparation process, such as surface roughness, as well as environmental factors like temperature fluctuations and vibrations, or the detection of the contact point are only partially captured by the standard deviation of the indentation moduli. Therefore, rather than relying solely on the intra-grain standard deviation, a fixed value of σ_{E^*} was adopted for all grains in the analysis.

Since the precise value of σ_{E^*} is not well-known, it was decided to continuously vary the value of σ_{E^*} during the simulations. This flexibility in the choice of σ_{E^*} allows for a detailed investigation of its impact on the posterior probability distributions. Thanks to the computational efficiency of our method, varying σ_{E^*} can be performed quickly, providing insights into the sensitivity of the results to the assumed measurement uncertainty. By varying σ_{E^*}, we ensure that the Bayesian simulations explore a range of possible interpretations of the data, leading to a more robust and stable convergence of the posterior distributions. This approach also allows for a more flexible interpretation of the experimental data, enhancing the reliability of the inferred values of A and $\nu_{<100>}$. This approach can also unravel the choice of the final retained constants by looking for stabilized values.

In parallel with the Bayesian analysis, the R2 score was computed as a comparative metric.

$$R^2\left(A, \nu_{\langle 100\rangle}\right) = 1 - \frac{\sum_k \left(R_k - r_k\left(A, \nu_{\langle 100\rangle}\right)\right)^2}{\sum_k \left(R_k - \overline{R}\right)^2} \tag{4.7}$$

where $\overline{R}$ denotes the mean of the experimental ratios and r_k the ratio obtained from the Vlassak

and Nix's model. The R^2 score increases when the least-square error, i.e. the sum of the squared differences between experimental and theoretical ratios, decreases. This least-square error provides a straightforward measure of the goodness-of-fit between the experimental data and the theoretical predictions. By comparing the R2 score to the posterior probability distributions obtained from the Bayesian inference, we can validate the results of the simulations and gain further confidence in the inferred values of A and $\nu_{<100>}$.

4.3 Bayesian Inference Workflow

In our Bayesian Inference workflow, we begin by generating a set of integration points and weights using Gauss-Legendre quadrature, which will be employed for later integrations. The experimental indentation data is then imported and extracted from an external file. Following data extraction, a range of standard deviations, representing the measurements uncertainties, is defined, for which values the inference is going to run and generate a set of results. Parameter grids are then constructed for both the anisotropy coefficient A and directional Poisson's ratio $\nu_{\langle 100\rangle}$ and their limits and increments are also defined. These grids cover a 2D-parameter space, ensuring systematic exploration of all possible values of A and $\nu_{\langle 100\rangle}$. In addition, a uniform prior probability distribution is assumed so that no initial bias is made toward any region of the parameter grid.

For each pair $\left(A, \nu_{\langle 100\rangle}\right)$, an elastic stiffness tensor with $E_{\langle 100\rangle} = 1$ is generated and a theoretical value of E^* is calculated using Vlassak & Nix's model for each experimental orientation. This will serve as a basis for comparison to the experimentally obtained values. The ratios of the experimental and theoretical E^* are calculated as well as their respective standard deviations.

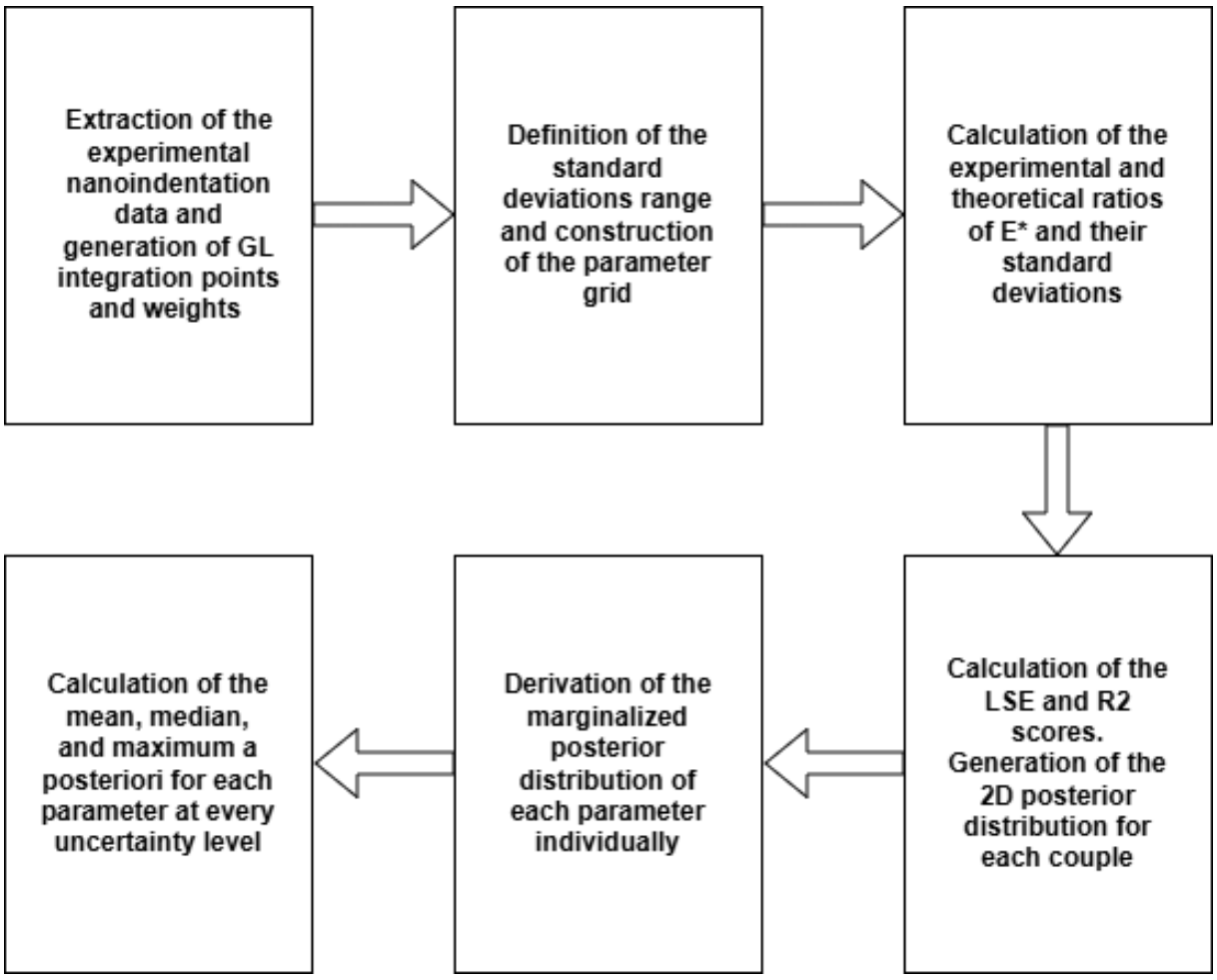

Figure 4.1: Diagram of the Bayesian inference workflow

The least-square error (LSE) is computed by summing the squared deviations between the theoretical and experimental ratios, providing a conventional point estimate of best-fit parameter for future comparison purposes. Then comes the calculation of the log-likelihood values for each parameter combination at each uncertainty level. And once the entire parameter space is evaluated, the code identifies the couple $\left(A, \nu_{\langle 100 \rangle}\right)$ that minimizes the LSE (here again for comparison purposes) in addition to generation a 2D distribution of the LSE for each couple. The Bayesian 2D posterior distribution for each couple is also generated, from which the marginalized posterior distributions of A, $\nu_{\langle 100 \rangle}$ and $E_{\langle 100 \rangle}$ are derived. The mean, median, and maximum a posteriori (MAP) for each parameter are subsequently calculated for each uncertainty level and their variation is visualized for each uncertainty level. This offers a robust way to interpret the results as the uncertainty rises and therefore aids in making the right statistical choice from the trends that

might arise.

4.4 Theoretical study with artificial data

This section addresses the question of how many theoretical points are needed to achieve satisfactory convergence in the Bayesian inference step. A number of randomly generated Euler angles for cubic grains are used and their associated theoretical nanoindentation moduli E^* are calculated for a given set of SECs ($C_{11} = 244GPa$, $C_{12} = 158GPa$, and $C_{44} = 102GPa$) corresponding to pure Ni. The values of E^* are then modified following a Gaussian probability law characterized by a given standard deviation. There are initially 5 points, and this number is incrementally increased by 5 points at a time. After each increment, the convergence behavior of the posterior marginal probabilities estimates are evaluated and we are able to determine the threshold beyond which additional points yield diminishing returns in accuracy. This study helps clarifying the practical considerations for implementing Bayesian inference in the case where nanoindentation experiments had to be setup on each grain individually, which can be very time consuming. For the sake of cohesion, the 2D posterior distributions shown below for each case are the ones corresponding to a standard deviation of 30 GPa.

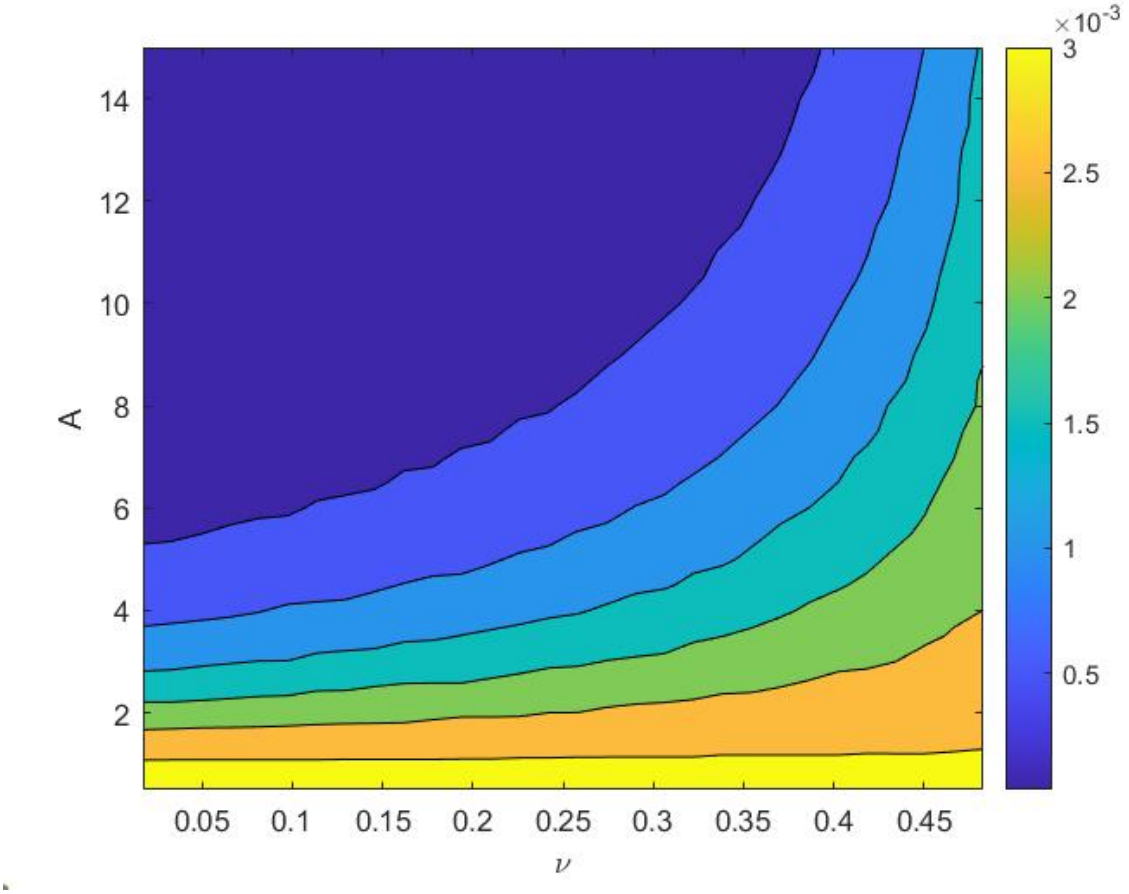

Figure 4.2: 2D distributions of the posterior probability $P\left(\left(A, \nu_{\langle 100\rangle}\right)|R^*\right)$ with respect to A and $\nu_{\langle 100\rangle}$ for 5 theoretically generated points.

Starting with just 5 generated points, the high probabilities posterior distribution (Fig. 4.2, see Eq. 4.2) remains relatively broad and diffuse, showing a wide range of A and $\nu_{\langle 100\rangle}$ values that could be interpreted as the actual values. The contours are also widely spaced, indicating high uncertainty in the parameter estimates. This indicates that 5 generated points are not sufficient to constraint the A and $\nu_{\langle 100\rangle}$ space.

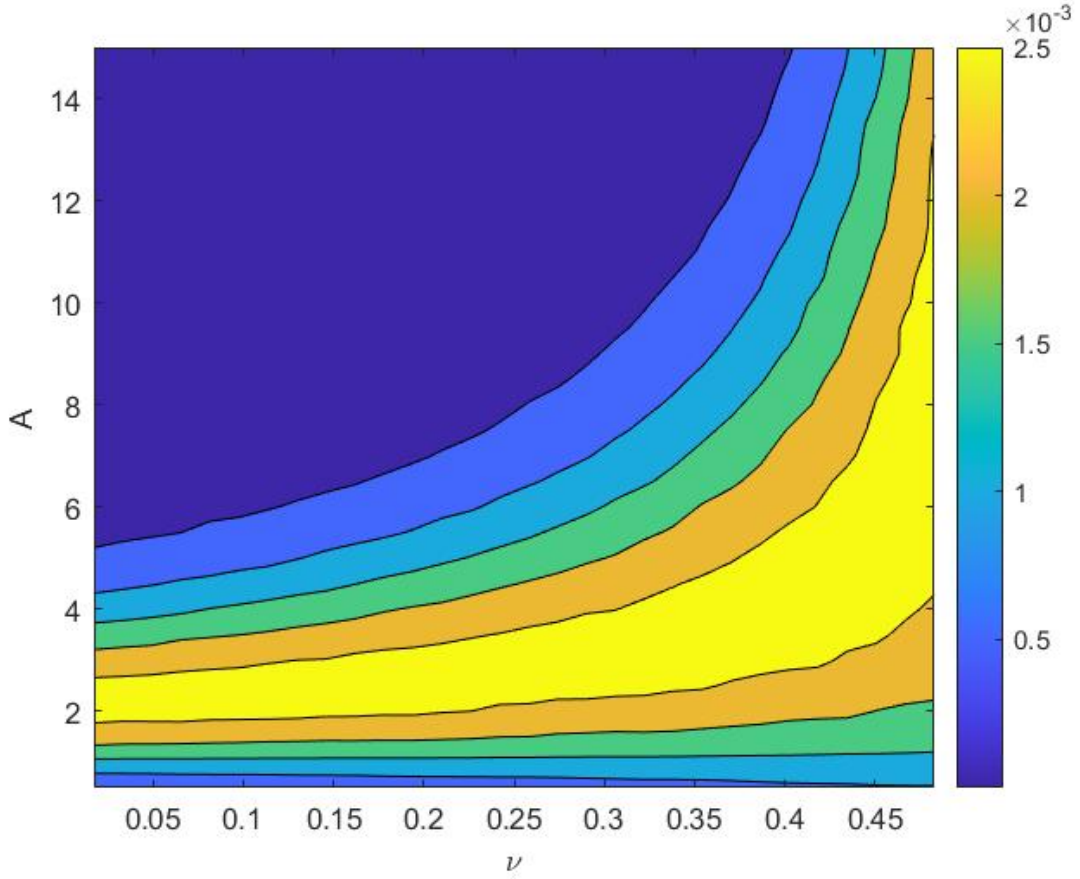

Figure 4.3: 2D distributions of the posterior probability $P\left(\left(A, \nu_{\langle 100\rangle}\right)|R^*\right)$ with respect to A and $\nu_{\langle 100\rangle}$ for 10 theoretically generated points.

Moving on to 10 generated points, the posterior distribution (Fig.4.3) begins to refine, even though the improvement remains modest. The contours start to tighten are certain regions of the A and $\nu_{\langle 100\rangle}$ parameter space, reflecting a slight decrease in the uncertainty around the parameter estimates. We also start seeing emerging structures with a clear indication that certain parameter ranges are more plausible than others.

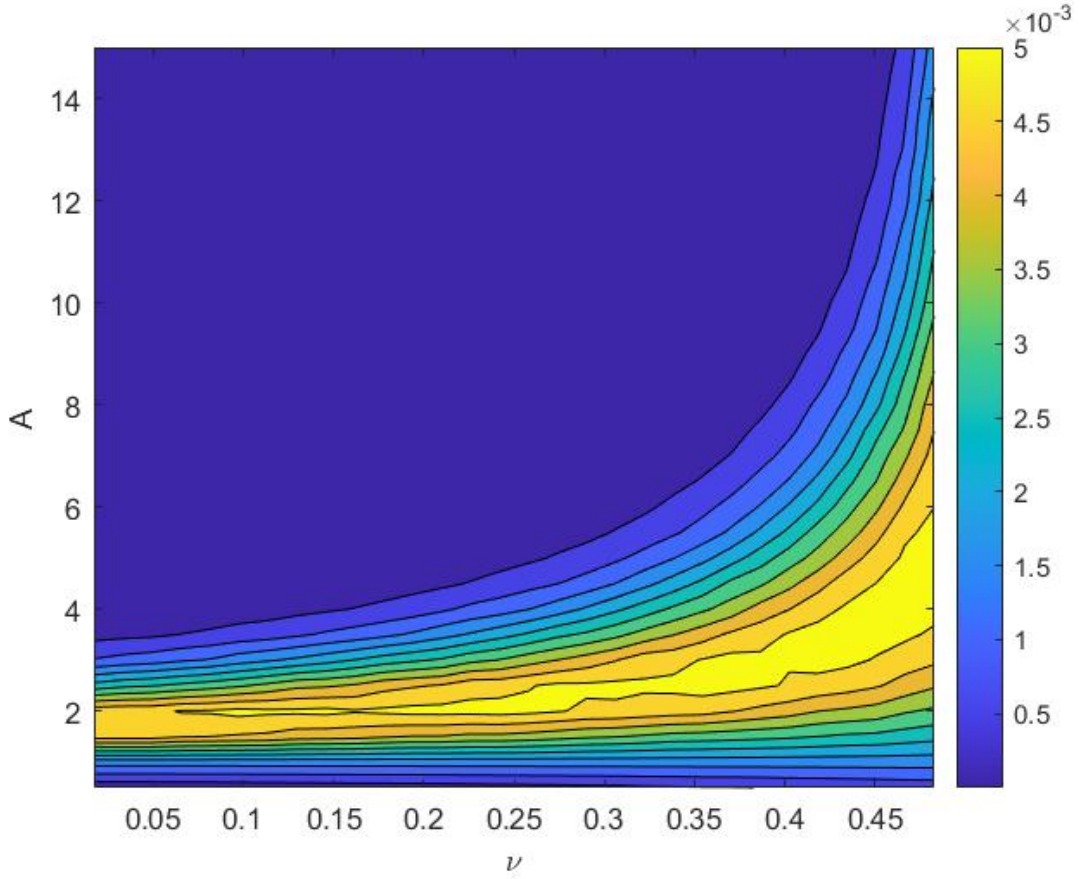

Figure 4.4: 2D distributions of the posterior probability $P\left(\left(A, \nu_{\langle 100\rangle}\right)|R^*\right)$ with respect to A and $\nu_{\langle 100\rangle}$ for 15 theoretically generated points.

With 15 generated points, the posterior distribution (Fig.4.4) becomes noticeably more constrained. It shows less spread and more pronounced contour gradients. As a results, the posterior distribution narrows and smooths out, and the we get a better and more definitive indication of where the best parameters lie in the A and $\nu_{\langle 100\rangle}$ space.

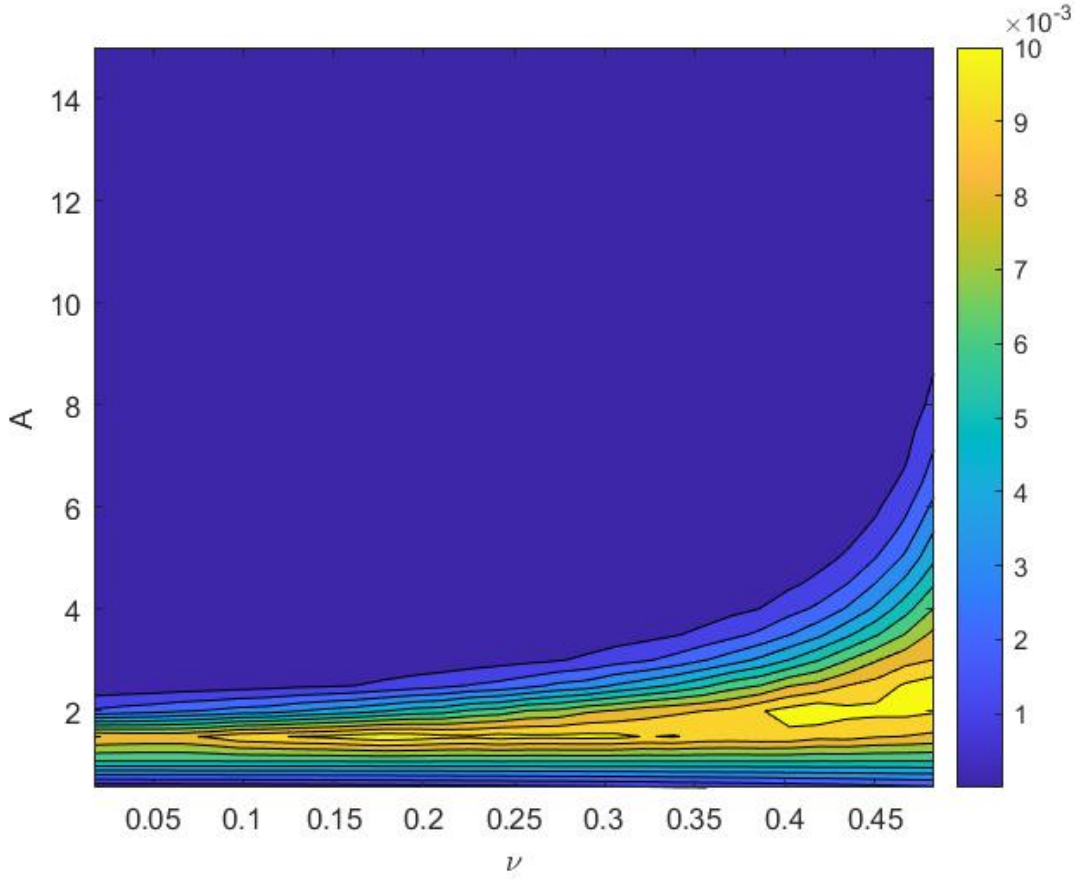

Figure 4.5: 2D distributions of the posterior probability $P\left(\left(A, \nu_{\langle 100\rangle}\right)|R^*\right)$ with respect to A and $\nu_{\langle 100\rangle}$ for 20 theoretically generated points.

As for 20 generated points, the posterior distribution (Fig.4.5) contours exhibit a more focused and coherent pattern. The A and $\nu_{\langle 100\rangle}$ parameter space that is consistent with the input date has become noticeably smaller, reflecting the high decrease in the uncertainty around the estimates. We start seeing closely spaced contours around a narrower set of values, showing that the model is beginning to close in on a particular solution.

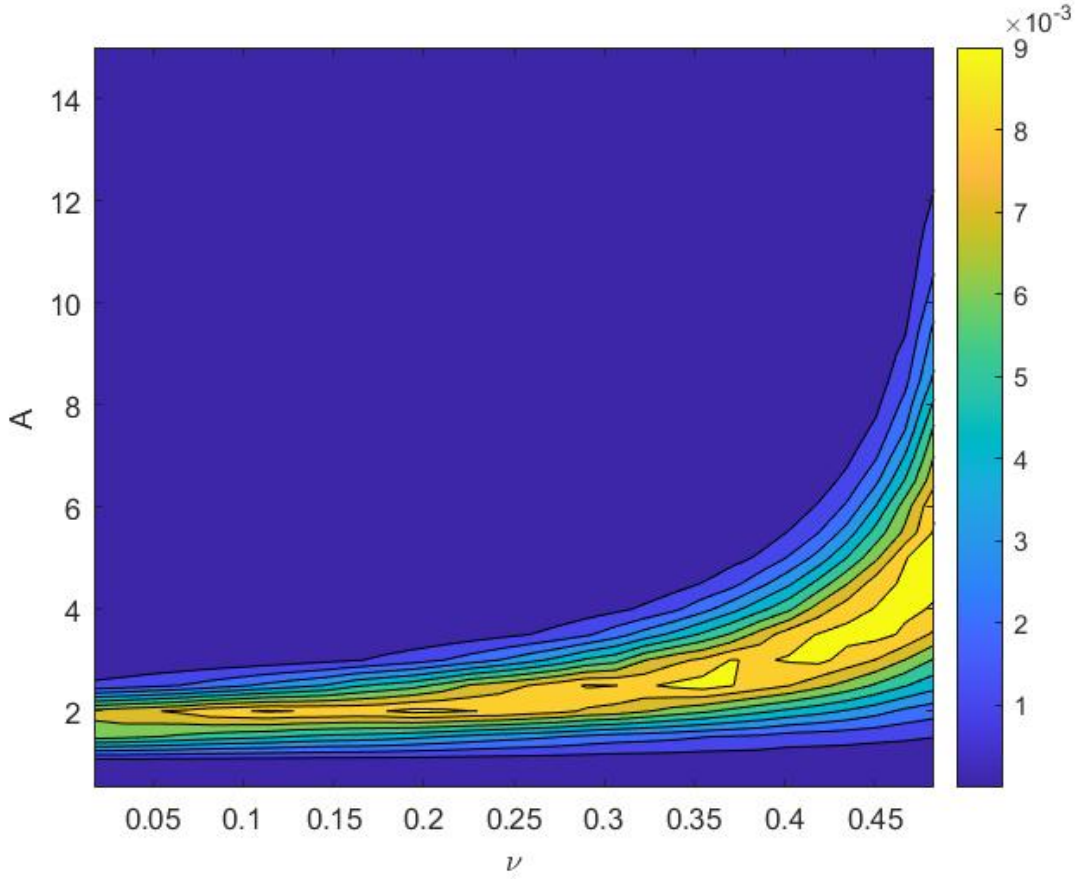

Figure 4.6: 2D distributions of the posterior probability $P\left(\left(A, \nu_{\langle 100\rangle}\right)|R^*\right)$ with respect to A and $\nu_{\langle 100\rangle}$ for 25 theoretically generated points.

By the time we reach 25 generated points, the posterior probability distribution (Fig.4.6) has reached a level of refinement and stability that leaves little doubt about which parameter region values are most likely to be consistent with the input data. The contours are distincly peaked and the preferred A and $\nu_{\langle 100\rangle}$ parameter space is tightly bounded. This demonstrates how the addition of generated data points guides the Bayesian inference into robust results.

4.5 Case study: Impact of A, $\nu_{\langle 100\rangle}$ and $E_{\langle 100\rangle}$ on the ratios of E^*

In this case study, we explore the effect of anisotropic mechanical properties, focusing on the anisotropy coefficient A, directional Poisson's ratio $\nu_{\langle 100\rangle}$ and directional Young's modulus $E_{\langle 100\rangle}$,

on the ratio of indentation moduli for two grains (A and B) with fixed orientations ($Phi1_A = 291$, $Phi_A = 131$, $Phi2_A = 221$, $Phi1_B = 159$, $Phi_B = 167$, and $Phi2_B = 267$) selected so that $E_A^* > E_B^*$. The objective is to understand how changes in these mechanical properties influence the ratio $\frac{E_A^*}{E_B^*}$. The parameters are varied systematically over a defined range to simulate different material behaviors. This approach allows us to explore the sensitivity of the anisotropic modulus ratio to changes in A, $\nu_{\langle 100 \rangle}$ and $E_{\langle 100 \rangle}$ for grains with predefined orientations.

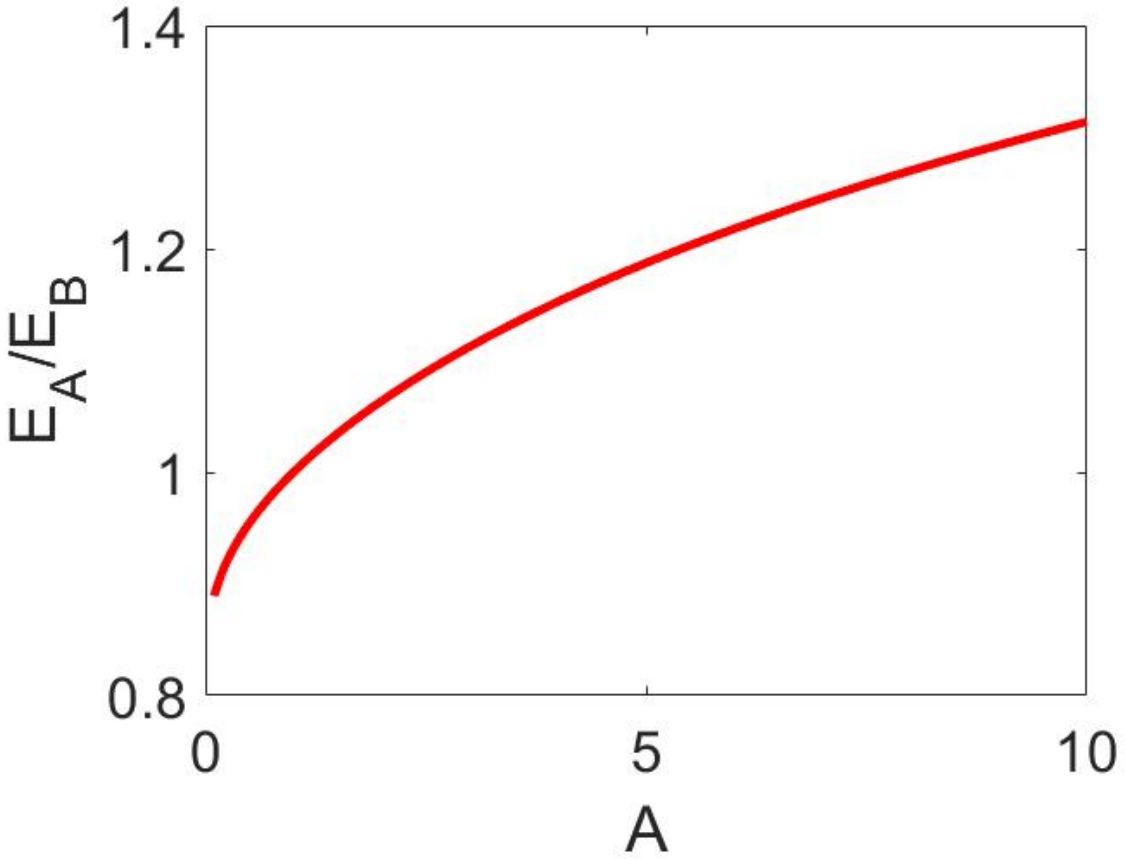

Figure 4.7: Variation of the anisotropic modulii ratio $\frac{E_A}{E_B}$ as a function of the anisotropy factor A.

Fig. 4.7 represents the behavior of the ratio $\frac{E_A^*}{E_B^*}$ as a function of the anisotropy coefficient A. The latter is varied in a range from 0 to 10, resulting in a clear upward trend in the ratio $\frac{E_A^*}{E_B^*}$. It is checked that for the isotropic case at $A = 1$, $\frac{E_A^*}{E_B^*} = 1$ as expected. However, as A increases or decreases, the ratio rises or drops steadily, respectively. The non-linear increase of A with $\frac{E_A^*}{E_B^*}$

shows however an ever-diminishing influence of A on E^* ratios.

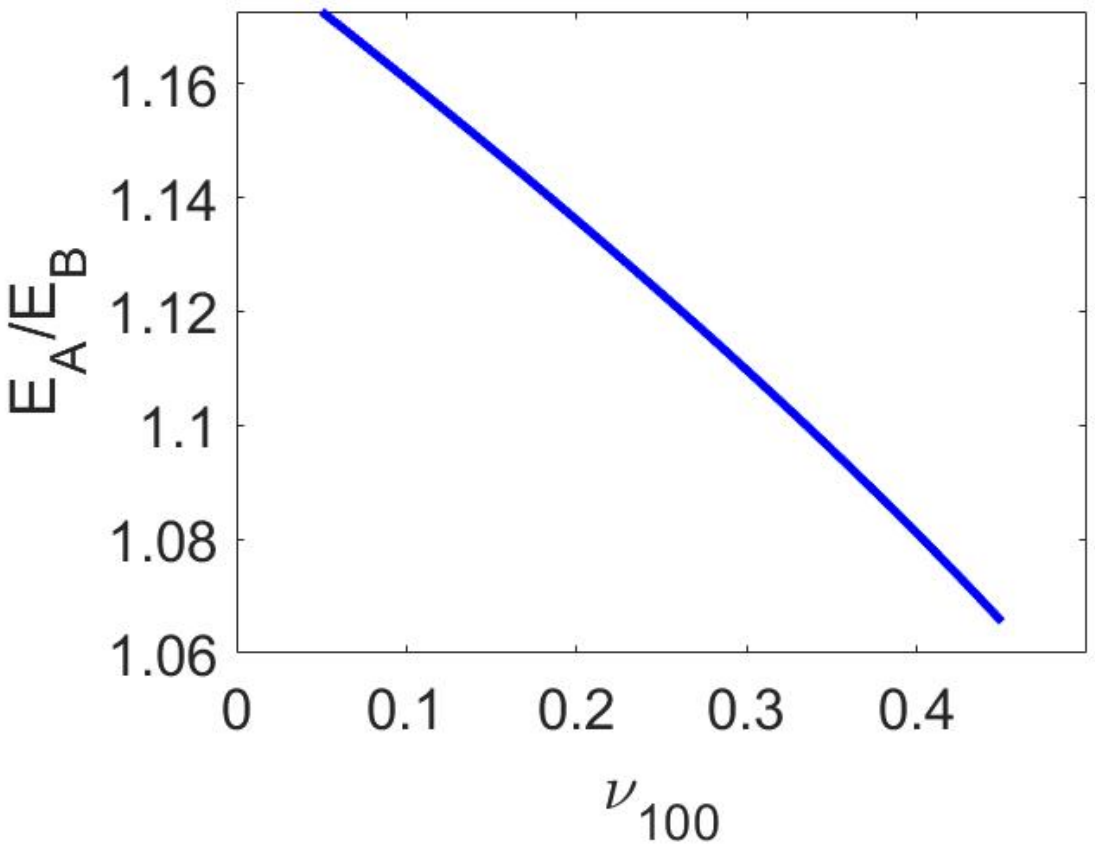

Figure 4.8: Variation of the anisotropic modulii ratio $\frac{E_A}{E_B}$ as a function of the directional Poisson's ratio $\nu_{\langle 100\rangle}$.

Fig. 4.8 on the other hand represents the behavior of the ratio $\frac{E_A^*}{E_B^*}$ as a function of the directional Poisson's ratio $\nu_{\langle 100\rangle}$. As it increases from 0.05 to 0.45, $\frac{E_A^*}{E_B^*}$ decreases steadily, indicating a negative correlation where an increase in $\nu_{\langle 100\rangle}$ reduces the relative stiffness of grain A compared to grain B. This means that a higher $\nu_{\langle 100\rangle}$ tends to soften grain A compared to grain B. The almost linear trend shows that the material becoming more incompressible leads to a reduction in the stiffness contrast between the two grains.

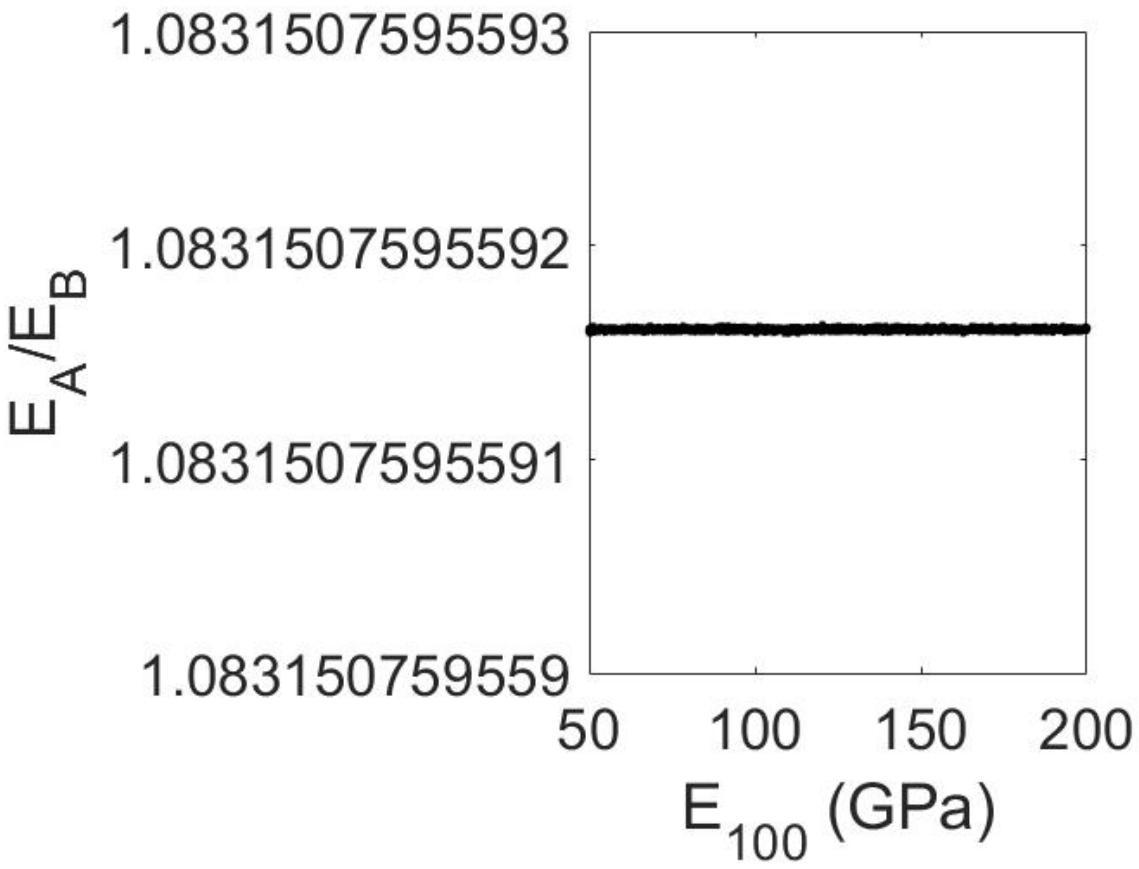

Figure 4.9: Variation of the anisotropic modulii ratio $\frac{E_A}{E_B}$ as a function of the directional Young modulus $E_{\langle 100\rangle}$.

Finally, Fig. 4.9 indicates that $\frac{E_A^*}{E_B^*}$ remains constant across the entire range of $E_{\langle 100\rangle}$ values. As it has can been inferred from Eq. 1.40 since $E_{\langle 100\rangle}$ can be factored out of the elastic stiffness tensor (cf. Eq. 3.12), this flat behavior brings a numerical confirmation that variations in $E_{\langle 100\rangle}$ do not affect the relative stiffness of two grains. Hence, the ratios $\frac{E_A^*}{E_B^*}$ depend on only the two dimensionless parameters A and $\nu_{\langle 100\rangle}$.

4.6 Conclusion

In this chapter, we have successfully demonstrated the application of Bayesian inference to the estimation of single-crystal elastic constants (SECs) using nanoindentation data. A key aspect of our approach was the use of indentation modulus ratios, which allowed for a more efficient

and robust exploration of the parameter space. By employing ratios instead of absolute values, we reduced the dependency on calibration parameters and increased the quantity of usable data, thereby improving the accuracy of the elastic constant estimations.

The integration of the Vlassak and Nix's model with Bayesian statistical methods enabled us to calculate the anisotropic elastic constants of cubic materials while simultaneously accounting for uncertainties in the experimental data. The use of indentation modulus ratios, along with the Bayesian framework, significantly enhanced the computational efficiency of the analysis, as much fewer simulations are required to achieve convergence.

One of the biggest advantage of the proposed method is that the limits of $\nu_{\langle 100 \rangle}$ and the lower limit of A are well-known from elastic stability conditions and are material's independent. Furthermore, the upper limit of A can be easily conjectured unlike the bounds of C_{ij} constants which are much harder to estimate *a priori* for an unknown material.

In conclusion, the use of indentation modulus ratios in combination with Bayesian inference represents a significant advancement in the characterization of SECs for cubic materials. This methodology not only improves the accuracy and reliability of the estimates but also offers a computationally efficient solution to the challenges posed by anisotropic and multiphase materials. The results presented in this chapter provide a strong foundation for further analysis and comparison with literature values in the following chapters.

Chapter 5

Results & Discussion

5.1 Introduction

In this chapter, a comprehensive analysis of the elastic properties of high-purity Ni and Inconel 718 that leverages nanoindentation experiments and Bayesian inference to extract key parameters such as the anisotropy factor and directional Poisson's ratio is going to be presented. The results are organized into distinct sections, focusing on different experimental datasets and methodologies, including high-speed nanoindentation mapping (HSNM) with Berkovich tips performed at ICA and spherical nanoindentation tests performed at LEM3. By combining experimental data with theoretical predictions from the Vlassak and Nix's model, the chapter aims to provide a detailed understanding of the materials' anisotropic behavior, while highlighting the influence of experimental uncertainty and dataset quality.

The first section explains the steps we took in pre-processing a preparing the experimental data obtained from measurements on our sample. We then move on to evaluate the broader implications of the results for the characterization of anisotropic materials. The high correlation between experimental and theoretical modulus values reinforces the validity of the Vlassak and Nix's model, particularly for IN718, where input data quality is superior.

The presentation of the results first focuses on HSNM results, providing insights into the anisotropic response of Ni and IN718 over a wide range of crystallographic orientations. The Bayesian analysis of these data offers robust posterior probability distributions for A, $\nu_{<100>}$,

and $E_{<100>}$, demonstrating the method's capacity to infer elastic properties while accounting for variability in the experimental input. Comparisons between R2 score distributions and posterior probability distributions further validate the reliability of the results. The analysis then transitions to the spherical nanoindentation data for high-purity Ni, where the smaller dataset necessitates a careful examination of parameter space constraints. Despite the reduced number of experimental points, the Bayesian inference approach remains effective, providing focused posterior distributions.

The discussion section integrates the findings across all datasets, comparing the inferred parameters to literature values, and examining the consistency of the results. The stabilized median values of the posterior distributions are highlighted as the most reliable statistical estimates for the desired parameters, given the non-symmetric nature of the probability distributions and their alignment with theoretical expectations. The influence of experimental variability, particularly in the Ni dataset, is critically analyzed, emphasizing the need for robust statistical frameworks such as Bayesian inference to handle uncertainties and outliers effectively.

Finally, the chapter concludes by evaluating the broader implications of the results for the characterization of anisotropic materials. The high correlation between experimental and theoretical modulus values reinforces the validity of the Vlassak and Nix's model, particularly for IN718, where input data quality is superior. These findings not only provide reference elastic constants for future studies but also demonstrate the potential of combining nanoindentation experiments with statistical inference to advance the understanding of materials anisotropy.

5.2 Pre-processing of Experimental Data

For the spherical nanoindentation tests conducted on high-purity Ni, each indentation modulus E_i^* value used in Eq. 4.3 was derived as the average of four individual measurements within a same grain. This procedure follows the methodology described in Section 2.5, ensuring consistency and reliability in the experimental results. Careful attention was paid to the selection of grains to guarantee a broad sampling of orientations. The chosen grains represented orientations close to the two extreme crystallographic directions, namely (001) and (111), as well as several intermediate orientations between these two extremes (see Fig. 5.2). This approach allowed for a comprehensive

evaluation of the anisotropic mechanical properties of the Ni sample across a range of orientations. In total, 21 experimental values of E_i^* were obtained from the spherical nanoindentation tests, and these values were subsequently used as inputs for the Bayesian simulations, providing a robust dataset for the inference process.

For the high-speed nanoindentation mapping performed with Berkovich tips, the data acquisition was considerably more extensive (see Section 2.6). After application of the sampling mask to remove indents located in carbides and close to grain boundaries, a total of 58 and 70 grains with a minimum of four indentations were available for the high-purity Ni and the Inconel 718 samples, respectively. Hence, each average value was calculated from a minimum of four indentations per grain, ensuring statistical significance and reducing the impact of outliers or local variations in the material. The high number of indentation points allowed for a detailed mapping of the mechanical properties across a wide range of grain orientations. However, for the Bayesian simulations, only large grains having a standard deviation on E^* lower than 12 GPa were kept. The purpose of this approach was to handle a more balanced number of input values for the Bayesian simulations between the two materials and to increase even more the robustness of the input data by ensuring that average values of E^* result mostly from indents far way from grain boundaries. Considering the difference of grain size and step size between the two samples (see Table 2.2), grains with equivalent diameter greater than 100 μm and 6 μm were selected for the Ni and IN718 samples, resulting in reduced numbers of 57 and 69 grains, respectively. This severe pre-processing ensured that both datasets were of comparable quality and could be used effectively in the subsequent Bayesian analysis.

5.3 Results from the correlative mechanical microscopy

We first present results from the correlative mechanical microscopy analyses, i.e., how the nanoindentation measurements are correlated to the crystallographic orientations obtained by EBSD. Regarding this issue, Fig. 5.1 shows side-by-side EBSD inverse pole figures according to the nanoindentation direction and maps of E^* obtained by HSNM within the same area for the two samples. From Fig. 5.1, it can be observed that the shape of almost all the grains of the IN718 sample

can be retrieved from the map of E^*. The map is very clear with well-defined grains. For the Ni sample, the map of E^* is more blurred, probably mainly because the surface finish was not as good as for the IN718 sample. The fact of having worked on a larger map with a lower spatial resolution and a lower CSM frequency (see Table 2.2) with a different nanoindentation system (FTI04 and a NMT04 sytems from Femtotools^{AG}, see Section 2.6) certainly also played a role. Nevertheless, a majority of grains can still be clearly identified. As expected from theoretical calculations in face-centered-cubic (fcc) structures with Zener ratio greater than one (see, e.g., Fig.3.4), the softest and stiffest grains correspond to grains with z-axis nearly aligned with $\langle 100 \rangle$ (red grains) and $\langle 111 \rangle$ (blue grains) directions, respectively.

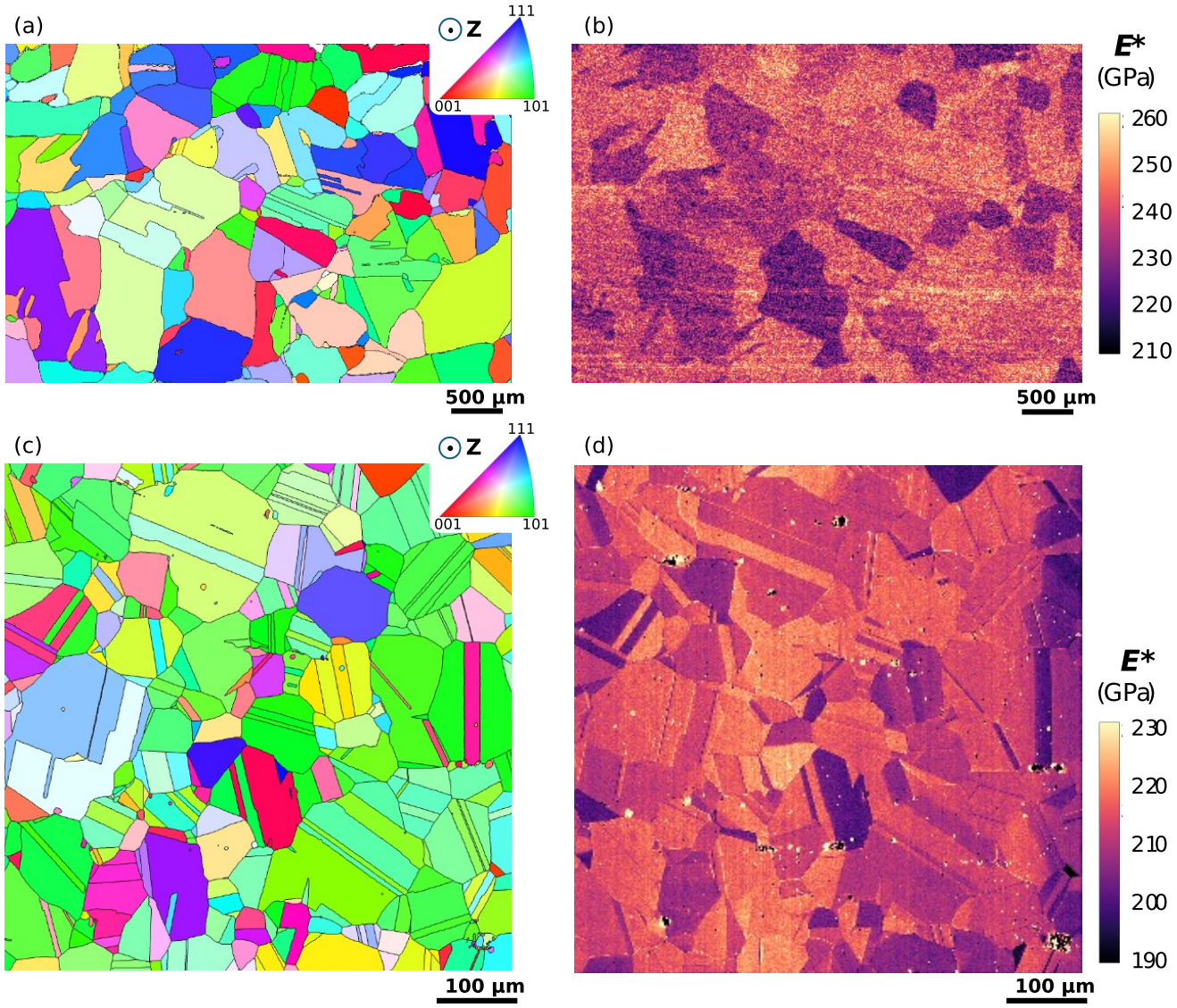

Figure 5.1: EBSD inverse pole figures of the Ni (a) and IN718 (c) samples along the indentation direction and corresponding maps of indentation modulus E^* within the same area (Ni (b) and IN718 (d)) obtained by MSNM at ICA.

In addition, the average values per grain of E^* selected for the Bayesian inference simulations according to the procedure detailed in Section 5.2 are plotted in an inverse pole figure along the indentation direction for the three samples in Fig. 5.2. This figure shows the relevance of our approach, with a variation of E^* which is globally consistent with the theoretical IPF map of Fig. 3.4.

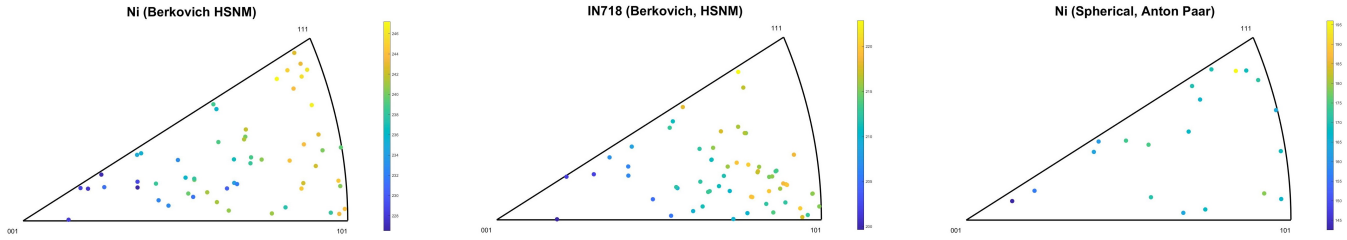

Figure 5.2: Experimental average values of E^* (in GPa) plotted in an inverse pole figure along the indentation direction for the three samples.

5.4 Results from Bayesian inference simulations

The results of the Bayesian inference simulations are presented in two separate sections. The first section corresponds to the HSNM measurements performed at ICA on high-purity Ni and IN718 samples. The second section focuses on the spherical nanoindentation data for high-purity Ni. In each case, the results include a comparison between the 2D distribution of the R2 score and the posterior probability distribution $P\left((A, \nu_{<100>})\,|R^*\right)$. Additionally, marginal posterior distributions of A and $\nu_{<100>}$ are illustrated for different values of σ_{E^*}, alongside examples of the probability distributions of $E_{<100>}$, providing a comprehensive overview of the inferred elastic properties. Finally, the evolution of the maximum a posteriori (MAP), median, and mean values of the marginal posterior distributions for A, $\nu_{<100>}$, and $E_{<100>}$ as a function of σ_{E^*} are examined to highlight the sensitivity of the results to the assumed measurement uncertainty.

5.4.1 High speed nanoindentation mapping (ICA)

In this section, the results of the Bayesian inference simulations are presented, beginning with Figs. 5.3 and 5.4, which illustrate the 2D distributions of the R^2 score (Eq. 4.7) and the posterior probability distribution $P\left(\left(A, \nu_{\langle 100\rangle}\right)|R^*\right)$ (Eq. 4.2). These two distributions exhibit pretty similar shapes and the trend is also similar between Ni and IN718 samples. The contour plots reveal that a significant portion of the $\left(A, \nu_{\langle 100\rangle}\right)$ parameter space can be ruled out due to either negative R^2 score or negligible posterior probabilities, indicating that many combinations of A and $\nu_{\langle 100\rangle}$ are unlikely. However, it is important to note that the regions of high posterior probability or high

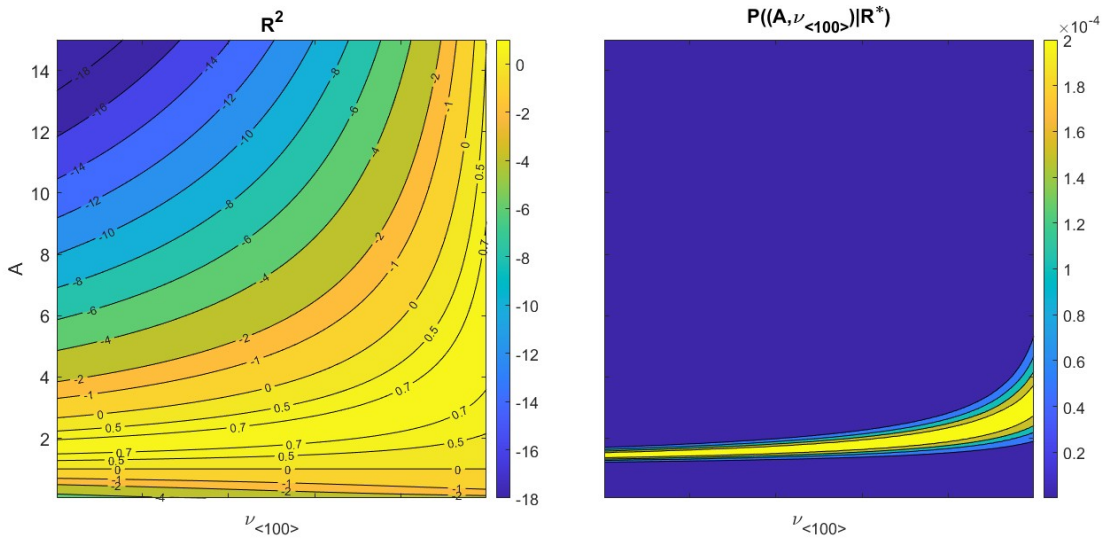

Figure 5.3: 2D distributions of the R^2 score and of the posterior probability $P\left(\left(A, \nu_{\langle 100 \rangle}\right) | R^*\right)$ for $\sigma_{E^*} = 50\,\text{GPa}$ with respect to A and $\nu_{\langle 100 \rangle}$ for the Ni sample.

R^2 score do not form a concentric pattern. While the range of likely A values is clearly restricted by this analysis, the situation for $\nu_{\langle 100 \rangle}$ is more complex. A broad spectrum of $\nu_{\langle 100 \rangle}$ values can still be associated with relatively high posterior probabilities or high R^2 score, indicating that it is difficult to constrain the value of $\nu_{\langle 100 \rangle}$ as precisely as A based on this analysis alone.

This first analysis demonstrates the challenge of selecting the most appropriate values for A and $\nu_{\langle 100 \rangle}$ purely from the computation of the R2 score, especially when a clear and well-defined global minimum does not emerge from the data. The non-concentric nature of the high-probability regions clearly makes it difficult the identification of a single, best-fit solution. Fortunately, Bayesian inference allows for a more nuanced approach by enabling the computation of marginal posterior distributions for A and $\nu_{\langle 100 \rangle}$. This is done by summing over the joint probability distribution $P\left(\left(A, \nu_{\langle 100 \rangle}\right) | R^*\right)$ for fixed values of either A or $\nu_{\langle 100 \rangle}$, which helps isolate the contributions of each parameter independently.

Figures 5.5, 5.6, 5.7 and 5.8 illustrate several examples of these marginal posterior distributions at different values of the uncertainty parameter σ_{E^*}. As can be seen, the marginal posterior distributions for A exhibit well-defined peaks, though the distributions are slightly asymmetric in shape. This suggests that, although there is a clear most likely value for A, the uncertainty surrounding this value is not distributed symmetrically, potentially indicating that extreme values of A are

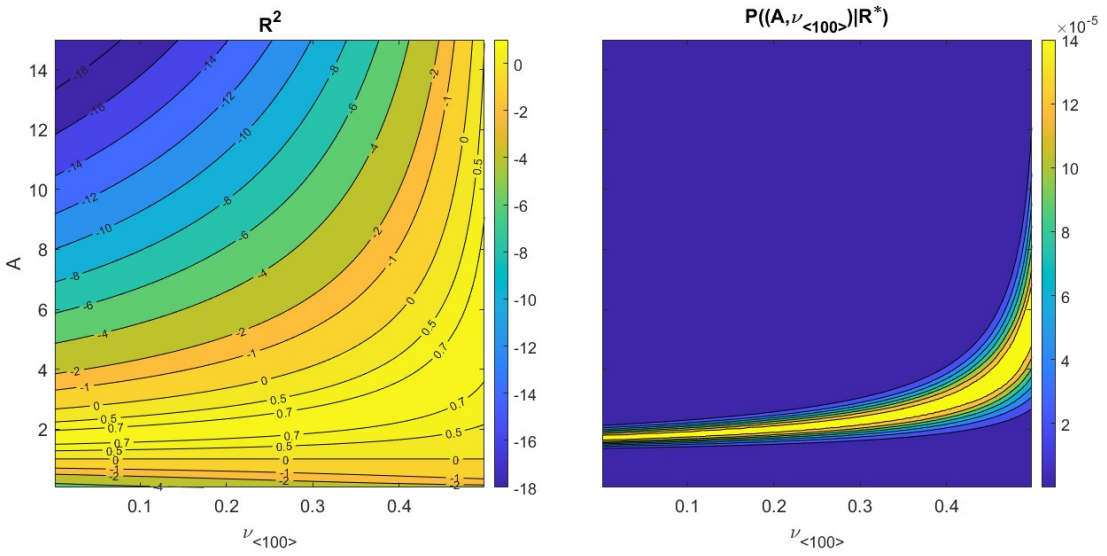

Figure 5.4: 2D distributions of the R^2 score and of the posterior probability $P\left(\left(A, \nu_{\langle 100\rangle}\right)|R^*\right)$ for $\sigma_{E^*} = 50\,\text{GPa}$ with respect to A and $\nu_{\langle 100\rangle}$ for the IN718 sample.

less likely but not entirely ruled out. On the other hand, the marginal posterior distributions for $\nu_{\langle 100\rangle}$ are distinctly different, displaying strong asymmetry and frequently showing saturation of the maximum probability near the upper boundary of 0.5. This saturation suggests that, while some values of $\nu_{\langle 100\rangle}$ are more probable than others, there remains a wide range of possible values, particularly at the high end of the distribution.

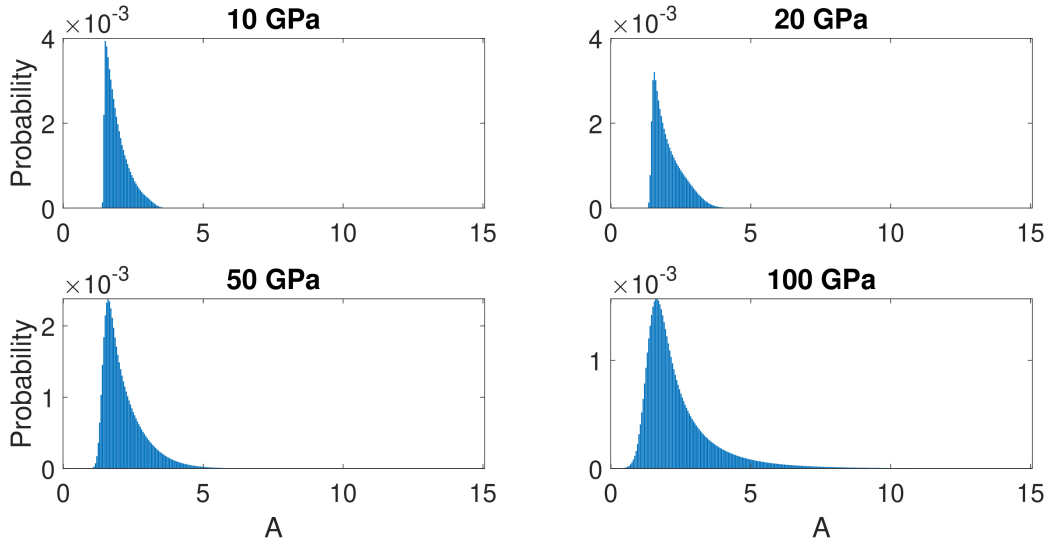

Figure 5.5: Marginal posterior distributions of A at 4 different values of σ_{E^*} for the Ni sample.

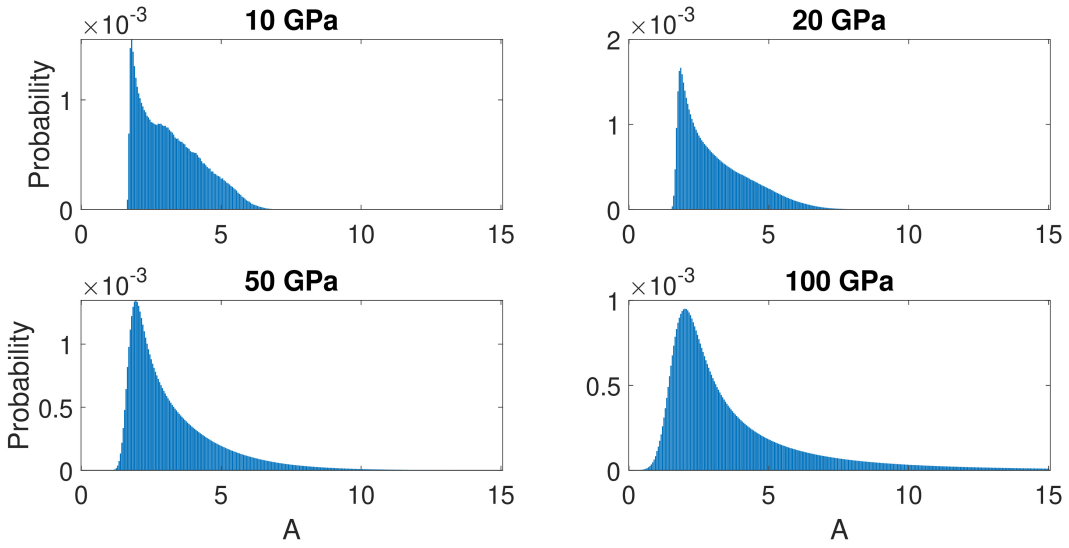

Figure 5.6: Marginal posterior distributions of A at 4 different values of σ_{E^*} for the IN718 sample.

In addition to these distributions, Figs. 5.9 and 5.10 provide examples of the posterior probability distributions for $E_{\langle 100 \rangle}$ at different values of σ_{E^*}. As with the other parameters, these distributions are not symmetric, although the degree of asymmetry decreases as σ_{E^*} increases. This trend indicates that as the uncertainty in the measured values of E^* increases, the Bayesian inference becomes more stable, producing less skewed distributions. This behavior is expected, as larger uncertainties generally lead to broader, more balanced probability distributions.

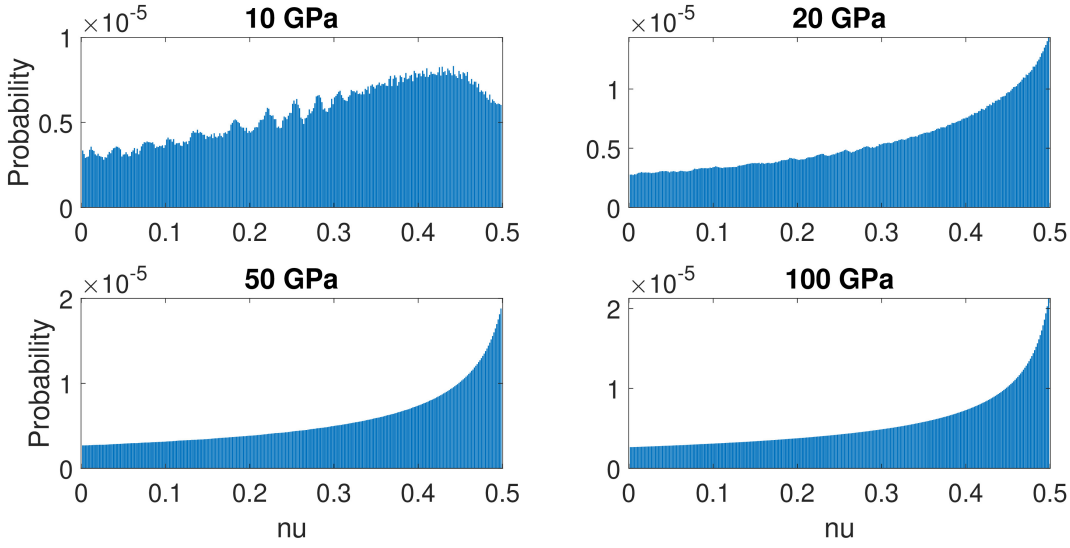

Figure 5.7: Marginal posterior distributions of $\nu_{\langle 100 \rangle}$ at 4 different values of σ_{E^*} for the Ni sample.

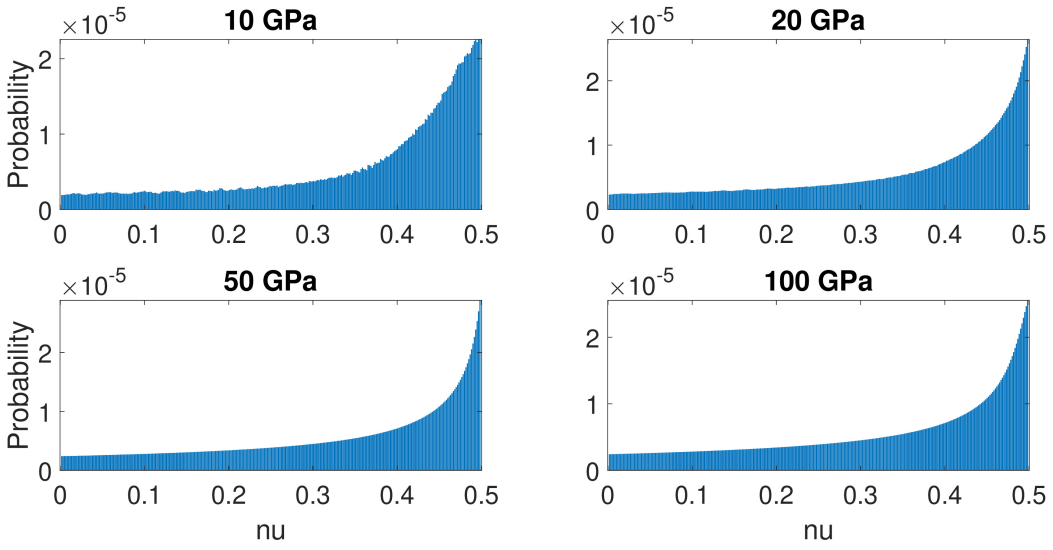

Figure 5.8: Marginal posterior distributions of $\nu_{\langle 100 \rangle}$ at 4 different values of σ_{E^*} for the IN718 sample.

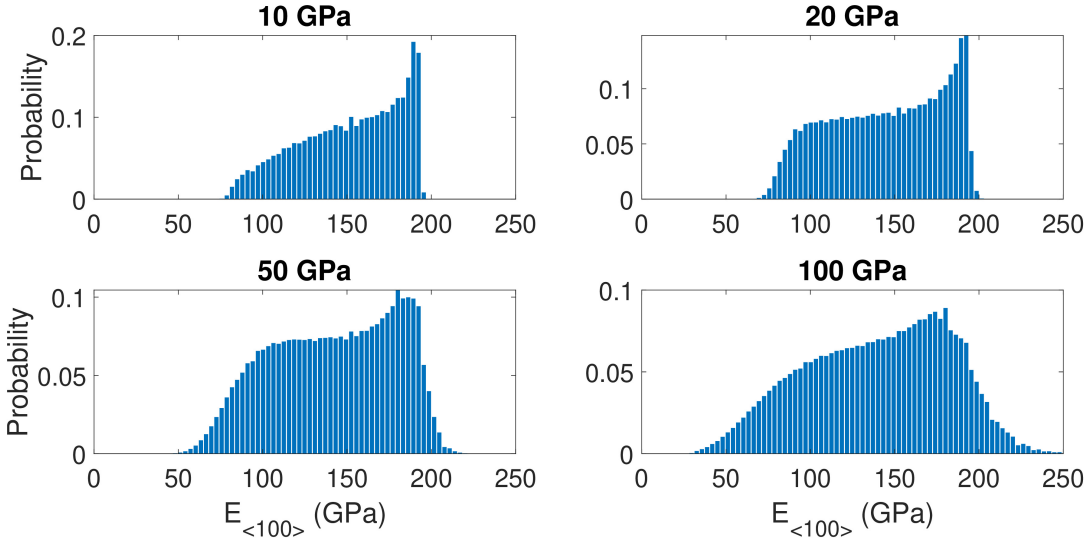

Figure 5.9: Posterior probability distributions of $E_{\langle 100 \rangle}$ at 4 different values of σ_{E^*} for the Ni sample.

Finally, Figs. 5.11 and 5.12 present the evolution of the MAP (maximum a posteriori), median, and mean values of the marginal posterior distributions for A, $\nu_{\langle 100 \rangle}$, and $E_{\langle 100 \rangle}$ as a function of σ_{E^*}. For comparison, the values of A and $\nu_{\langle 100 \rangle}$ corresponding to the maximum R^2 score and the maximum posterior probability $P\left(\left(A, \nu_{\langle 100 \rangle}\right) | R^*\right)$ are also indicated.

The results show that the median values of the posterior distributions for A, $\nu_{\langle 100 \rangle}$, and $E_{\langle 100 \rangle}$ remain stable as σ_{E^*} increases, suggesting that the Bayesian inference method produces consistent

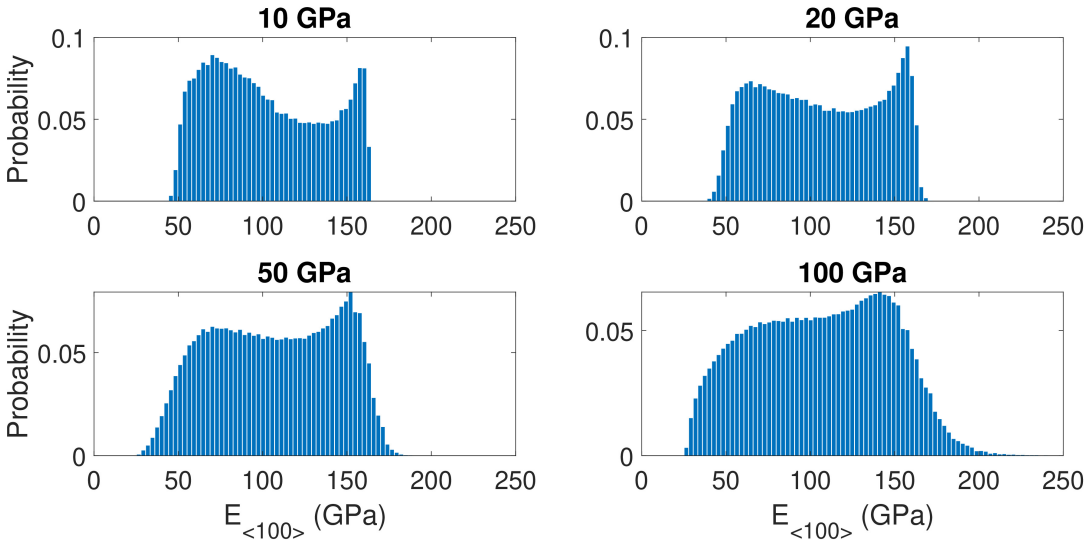

Figure 5.10: Posterior probability distributions of $E_{\langle 100\rangle}$ at 4 different values of σ_{E^*} for the IN718 sample.

results even as the uncertainty in E^* changes. In contrast, the mean values of $\nu_{\langle 100\rangle}$ and $E_{\langle 100\rangle}$ also stabilize as σ_{E^*} increases, but the mean value of A continues to rise with increasing σ_{E^*}. This difference highlights the importance of considering both the mean and median values when interpreting the results. The MAP values exhibit similar trends, with A increasing as σ_{E^*} rises, while $E_{\langle 100\rangle}$ decreases slightly and $\nu_{\langle 100\rangle}$ stabilizes near its upper limit of 0.5.

It is important to emphasize that a value of $\nu_{\langle 100\rangle} = 0.5$ results in a high posterior probability only when associated with very high values of A (see Figs. 5.3 and 5.4). However, such high values of A (greater than 4) are unrealistic, as indicated by the marginal posterior distributions of A (see Figs.5.5 and 5.6) and values found in the literature (see further Tables 5.1 and 5.2). Consequently, relying solely on the maximum posterior probability $P\left(\left(A, \nu_{\langle 100\rangle}\right)|R^*\right)$ does not yield consistent results, as substantial variations are observed when changing σ_{E^*} (see Figs. 5.11 and 5.12).

Therefore, based on all these considerations, it is well justified to adopt the stabilized median values of the posterior distributions for A, $\nu_{\langle 100\rangle}$, and $E_{\langle 100\rangle}$ as the final retained values.

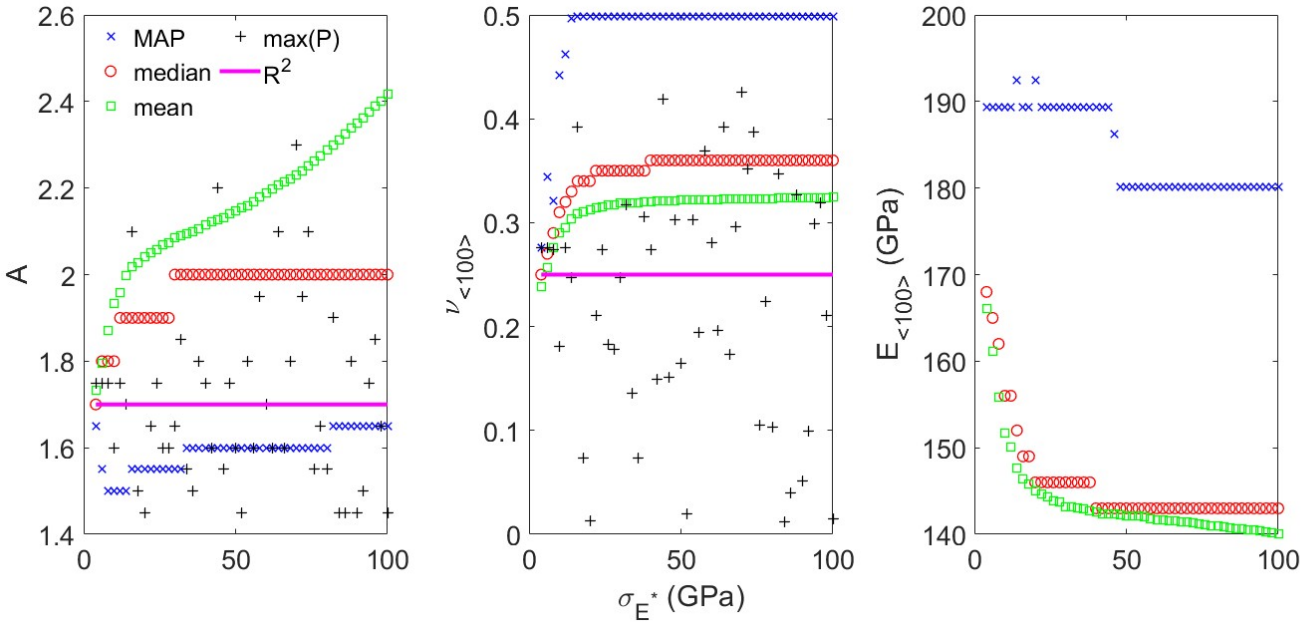

Figure 5.11: For the Ni sample, evolution with σ_{E^*} of the MAP, median and mean values of the marginal posterior distributions of A and $\nu_{\langle 100\rangle}$, along with the values of A and $\nu_{\langle 100\rangle}$ associated to the maximum of $P\left(\left(A, \nu_{\langle 100\rangle}\right)|R^*\right)$ (max(P)) and the ones corresponding to the maximum R^2 score. The evolution of the MAP, median and mean values of the posterior probability distributions of $E_{\langle 100\rangle}$ are shown as well.

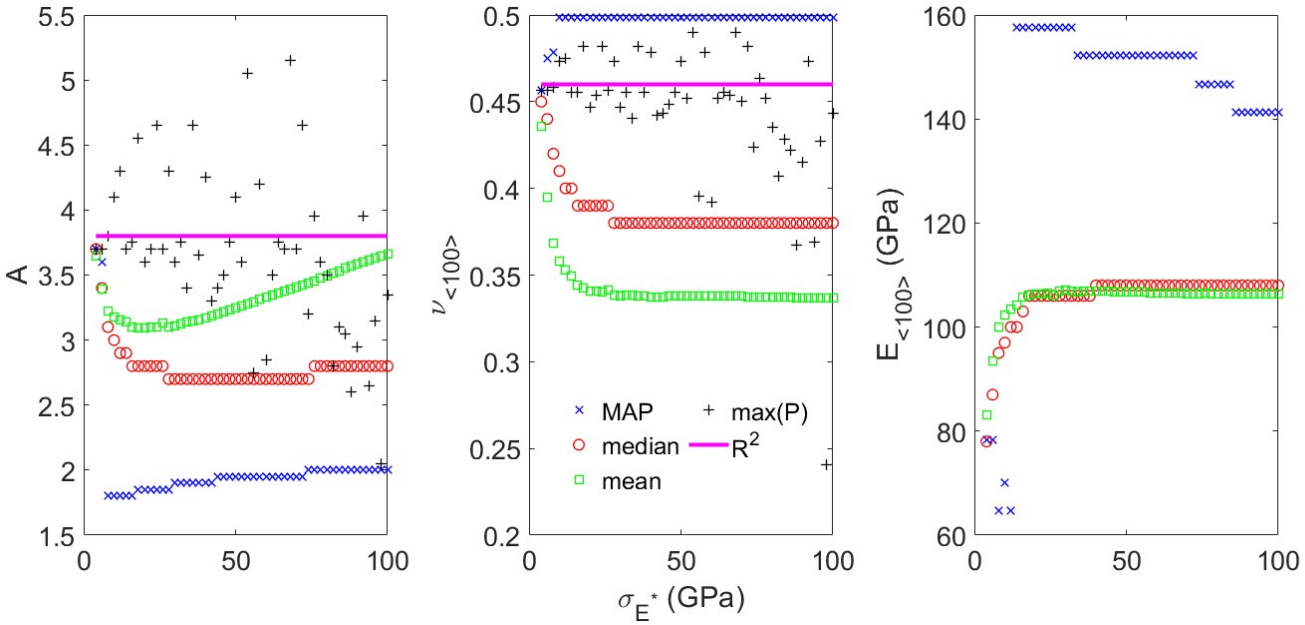

Figure 5.12: For the IN718 sample, evolution with σ_{E^*} of the MAP, median and mean values of the marginal posterior distributions of A and $\nu_{\langle 100\rangle}$, along with the values of A and $\nu_{\langle 100\rangle}$ associated to the maximum of $P\left(\left(A, \nu_{\langle 100\rangle}\right)|R^*\right)$ (max(P)) and the ones corresponding to the maximum R^2 score. The evolution of the MAP, median and mean values of the posterior probability distributions of $E_{\langle 100\rangle}$ are shown as well.

5.4.2 Ni Spherical (LEM3)

We are now moving to the results of the Bayesian inference simulations performed on experimental data obtained from spherical nanoindentation tests on pure Ni samples at LEM3. Fig. 5.13 shows the 2D distribution of the R2 score (left) and the posterior probability distribution (right). Like for HSNM results, the two distributions display very similar behavior, with both showing non-concentric patterns and a clear dependence on the values of A and $\nu_{<100>}$. The posterior probability distribution highlights a focused region of probable combinations for A and $\nu_{<100>}$ that is wider than the one obtained using HSNM, given the fact that we are working with less experimental points this time. The high-probability region of $\nu_{<100>}$ lacks symmetry, with higher posterior values being concentrated closer to the upper boundary of 0.5. On the contrary, the posterior values of A are more narrowly defined.

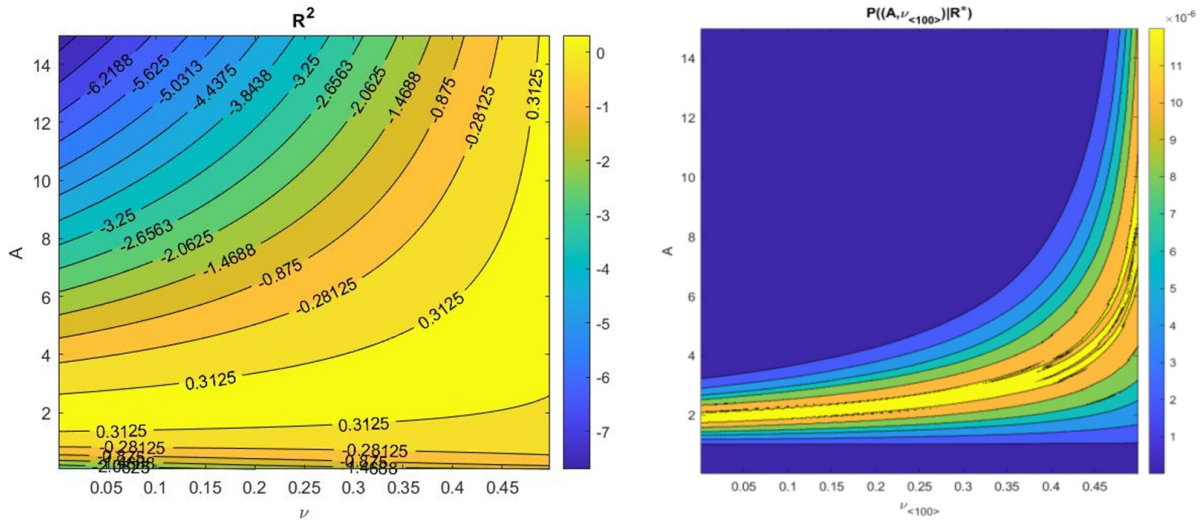

Figure 5.13: On the left, 2D distributions of the R^2 score (cf. Eq. 4.7) with respect to A and ν_{100} values considering the spherical nanoindentation data on high-purity Ni. On the right, posterior probability distribution $P\left((A, \nu_{<100>})\,|R^*\right)$ for $\sigma_{E^*} = 50\,\text{GPa}$.

Figs. 5.14, and 5.15 display here again multiple examples of the marginal posterior distributions at different values of the uncertainty parameter σ_{E^*}. As the uncertainty increases, the posterior distributions evolve significantly, broadening and shifting in shape. At lower uncertainty levels, the distribution is characterized by a sharp peak, indicating a well-defined most likely value for A. However, as σ_{E^*} increases, the peak diminishes in height, and the distribution becomes more

skewed, suggesting an increasing likelihood of larger A values. Like for HSNM, this indicates that extremely high values for A are not entirely statistically ruled out but are less likely to be the right values. The marginal posterior distributions for $\nu_{<100>}$ still display high asymmetry with probabilities increasingly saturating near the upper boundary as σ_{E^*} increases. This behavior highlights the difficulty of narrowing down $\nu_{<100>}$'s value due to its behavior.

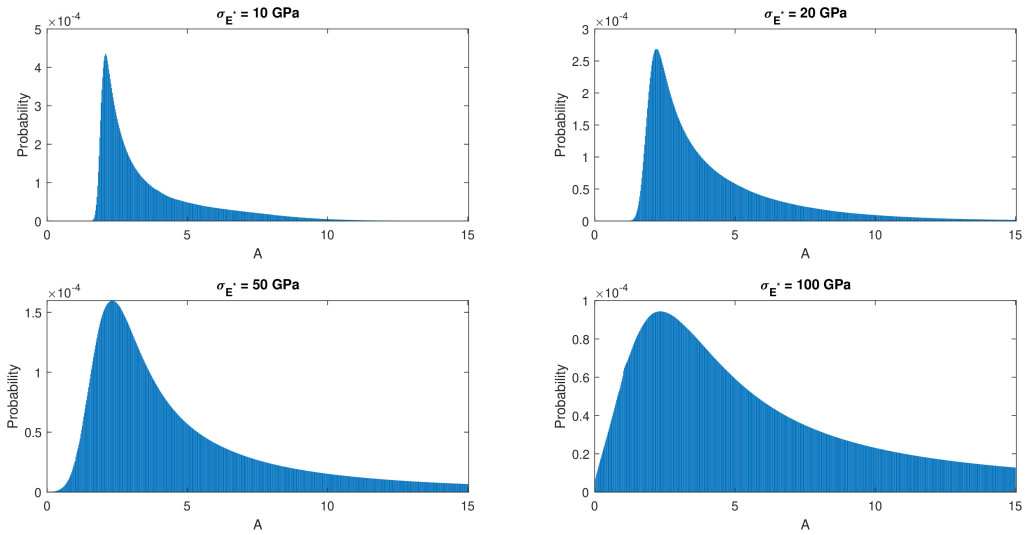

Figure 5.14: Marginal posterior distributions of A at 4 different values of σ_{E^*} considering the spherical nanoindentation data on high-purity Ni.

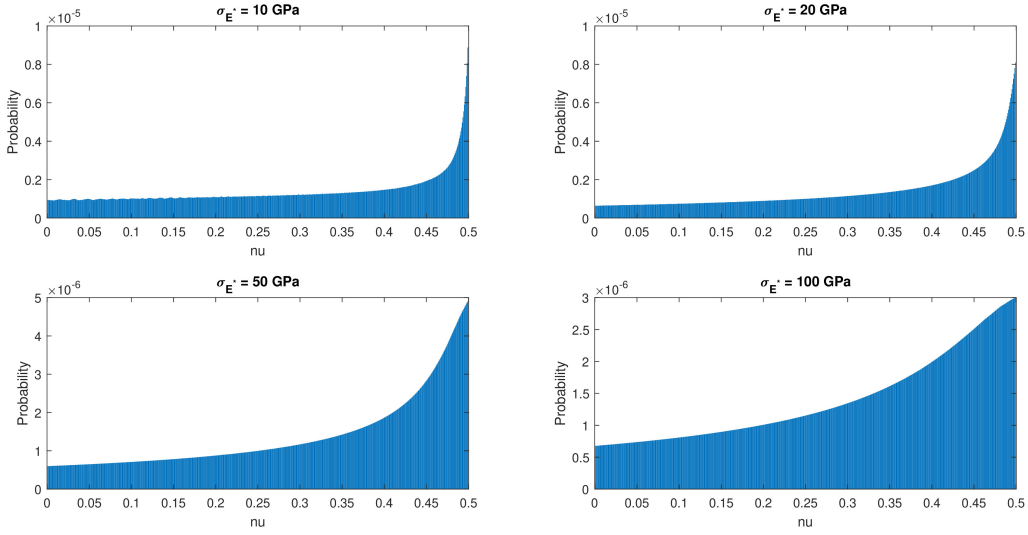

Figure 5.15: Marginal posterior distributions of $\nu_{<100>}$ for 4 different values of σ_{E^*} considering the spherical nanoindentation data on high-purity Ni.

Combining the experimental values of E^* with the theoretical ones obtained using Vlassak

& Nix's model, we are again able to provide the posterior probabilities for $E_{<100>}$ as shown in Fig. 5.16. Similar to A and $\nu_{<100>}$ posterior distributions, they are asymmetric for low values of σ_{E^*}, with the asymmetry decreasing with increasing σ_{E^*} values.

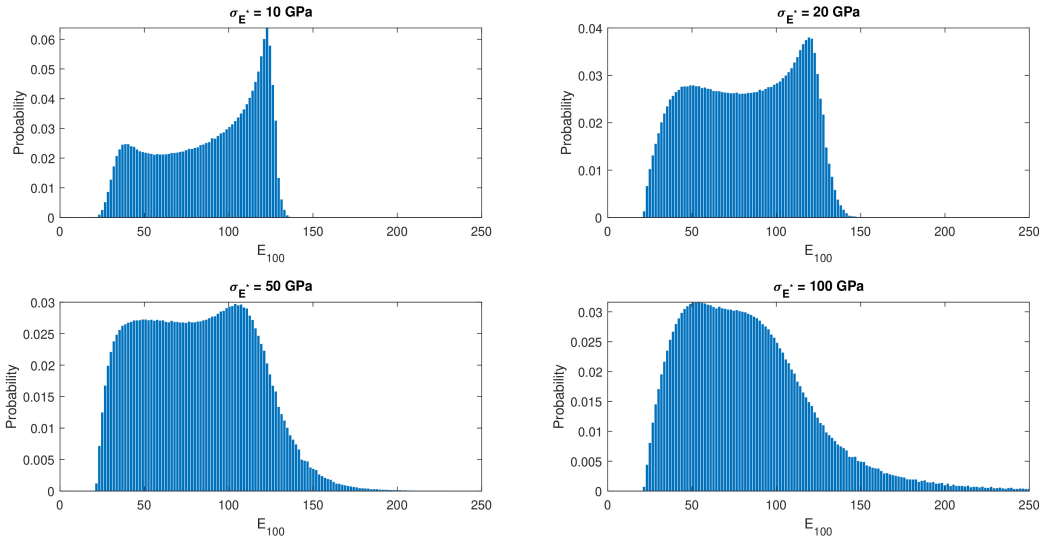

Figure 5.16: Probability distributions of $E_{<100>}$ for 4 different values of σ_{E^*} considering the spherical nanoindentation data on high-purity Ni.

We conclude with Fig. 5.17 that again showcases the evolution of the MAP, median, and mean values of the marginal posterior distribution for A, $\nu_{<100>}$ and $E_{<100>}$ as a function of σ_{E^*}. Here again, the results show that the median values of the posterior distributions of $\nu_{<100>}$ and $E_{<100>}$ remain stable with an increasing uncertainty parameter σ_{E^*}. The mean values almost stabilize also with increasing σ_{E^*}, but the asymmetry of the marginal posterior distributions makes the median a better choice when it comes to statistical representation. However, concerning the marginal posterior distribution of A, the median does not really stabilize but rather show an increasing trend. On the contrary, the MAP value of A stabilizes pretty well and appears thus a better choice. Therefore, based on the above considerations, we have chosen the stabilized MAP value of the posterior distribution of A and the stabilized median values of the posterior distributions of $\nu_{<100>}$ and $E_{<100>}$ as the final retained values.

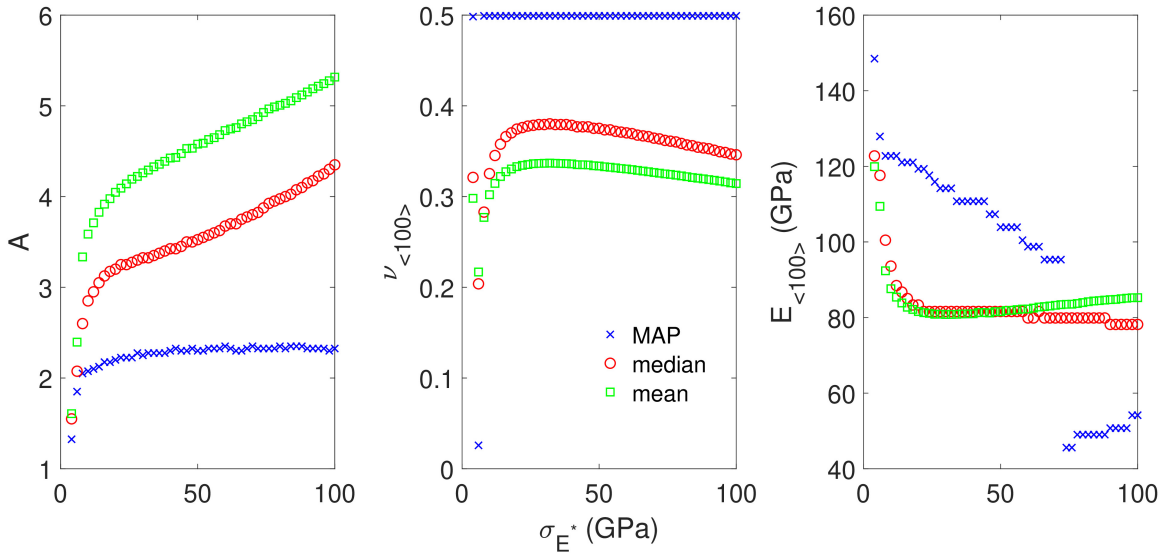

Figure 5.17: Evolution with σ_{E^*} of the MAP, median and mean values of the marginal posterior distributions of A and $\nu_{<100>}$, as well as of the probability distribution of $E_{<100>}$, as results of the Bayesian inference simulations considering the spherical nanoindentation data on high-purity Ni.

5.5 Discussion

The retained SEC values for high-purity Ni can be compared to those of the literature values present in Table 5.1. The latter are taken from reference (Ledbetter *et al.*, 1973). It gathers the main literature values for the SEC of pure Ni measured by different experimental techniques. On the whole, these values show a good agreement. It is seen that the SEC values obtained by the current approach are well within the literature range, although the values of A and $\nu_{\langle 100\rangle}$ lie at the lower limit. When performing the conversion in terms of C_{11}, C_{12} and C_{44} values, the match is actually a little bit less good for C_{11} and C_{12}. This is due to the difference between our value for $\nu_{\langle 100\rangle}$ and the typical literature value around 0.38. Indeed, when $\nu_{\langle 100\rangle}$ get close to 0.5, C_{11} and C_{12} start to diverge because of the presence of the $\left(1-2\nu_{\langle 100\rangle}\right)$ term in the denominator of Eq. 3.12.

The main literature values for the SEC of IN718 are gathered in Table 5.2. Compared to pure Ni, there are much less data available and much more variability. It should be also emphasized that, contrary to the Ni data, the SEC values correspond to estimations based on indirect methods, with results closely depending on the choice of the micromechanical model (Haldipur, 2006; Martin

et al., 2014; Schröder *et al.*, 2023). The SEC values obtained by our approach are nevertheless well within this literature range. It can be noticed that the value of $E_{\langle 100\rangle}$ (108 GPa) is just a little bit below the minimum of the literature (114 GPa).

Besides, it is noteworthy that the stabilized median values of the posterior distributions are closer to the literature ranges compared to the stabilized mean or MAP values. Moreover, approaches that consider directly the best couple of $\left(A, \nu_{\langle 100\rangle}\right)$, from either the maximum posterior probability $P\left(\left(A, \nu_{\langle 100\rangle}\right)|R^*\right)$ or the maximum R2 score, provide results which are in general very far from the literature ranges (see Figs.5.11 and 5.12). The choice to consider the median values of the marginal posterior distributions seems thus well-justified from both the non-symmetric shapes of the probability distributions, the stabilization of the three SEC with σ_{E^*} and the comparisons with the literature data.

Reference	C_{11}	C_{12}	C_{44}	A	$\nu_{<100>}$	$E_{<100>}$
Present study (spherical tip)	154	94	68	2.3	0.38	82
Present study (Berkovich tip)	240	135	105	2.0	0.36	143
Honda *et al.*, 1937	252	151	104	2.1	0.37	139
Bozorth *et al.*, 1949	250	160	119	2.6	0.39	125
Bozorth *et al.*, 1951	252	157	123	2.6	0.38	131
Neighbours *et al.*, 1952	253	152	124	2.5	0.38	139
Yamamoto, 1950	244	158	102	2.4	0.39	120
Levy *et al.*, 1953	247	152	121	2.5	0.38	131
De Klerk *et al.*, 1955	243	149	119	2.5	0.38	130
Shirakawa *et al.*, 1958	255	169	90	2.1	0.40	120
De Klerk, 1959	246	150	121	2.5	0.38	132
Alers *et al.*, 1960	251	150	124	2.5	0.37	139
Sakurai *et al.*, 1964	251	153	124	2.5	0.38	135
Epstein *et al.*, 1965	248	154	124	2.6	0.38	130
Vintaikin, 1966	247	144	124	2.4	0.37	141
Salama *et al.*, 1969	252	154	122	2.5	0.38	135
Shirakawa *et al.*, 1969	288	181	124	2.3	0.39	148

Table 5.1: Literature values in GPa of C_{11}, C_{12} and C_{44} constants for high purity Ni and conversion into A, $\nu_{<100>}$and $E_{<100>}$ (in GPa) values.

Next, it should be underlined that if part of the present results were obtained by performing High-Speed Nanoindentation Mapping, the latter is not crucial for the success of the method, as we have shown that acceptable results can be achieved using classical targeted indentations. The proposed procedure should work as well with conventional nanoindentation experiments. In

Ref.	A	$\nu_{\langle 100\rangle}$	$E_{\langle 100\rangle}$	C_{11}	C_{12}	C_{44}
Present study	2.7	0.38	108	202	124	106
Martin *et al.*, 2014	2.7	0.41	114	260	179	110
Schröder *et al.*, 2023	2.4	0.35	124	201	109	110
Haldipur, 2006	2.0	0.36	141	242	139	104

Table 5.2: Values of A, $\nu_{\langle 100\rangle}$ and $E_{\langle 100\rangle}$ (in GPa) retained after the Bayesian inference simulations for Inconel 718 and their conversion into C_{11}, C_{12} and C_{44} values (in GPa) (Present study). Comparisons with literature values (found as C_{11}, C_{12} and C_{44} values and converted in terms of A, $\nu_{\langle 100\rangle}$ and $E_{\langle 100\rangle}$).

fact, the method does not necessarily work better if more data are considered. By increasing the number of input data, the probability of having outliers is also increased. A few outliers are however enough to influence the final results in the wrong direction, as can been inferred from the multiplication of individual probabilities to get the likelihood (Eq. 4.5). The big advantage of HSNM lies in the possibility to visualize directly how relevant are the input data by comparing EBSD and indentation modulus maps, as done in Fig. 5.1.

Considering this aspect, it may be conjectured that the analysis made for the IN718 sample is certainly more reliable than the one made for the Ni sample, given the much better match between EBSD and E^* maps while the two materials have close elastic anisotropy. The lesser accuracy of the input data for the Ni sample might be the source of the small underestimation of A and $\nu_{\langle 100\rangle}$ values. On the contrary, the good accuracy of the input data for the IN718 sample provides some trust in the SEC values found by our approach (Table 5.2). This is corroborated by the results of Fig. 5.18 where the indentation moduli computed with the Vlassak and Nix's model using the retained values for A, $\nu_{\langle 100\rangle}$ and $E_{\langle 100\rangle}$ in Tables 5.1 and 5.2 are plotted with respect to the experimental indentation moduli. Both the Ni and IN718 samples exhibit high values of the Pearson correlation coefficient with $r = 0.85$ and $r = 0.87$, respectively. Such a strong positive correlation indicate that the Vlassak and Nix's model captures very well the variation of E^* with the crystallographic orientation of the indentation surface. However, it can be noticed that the R^2 score, herein computed directly from the indentation moduli and not from the ratios as in Figs. 5.3 and 5.4, is much higher for the IN718 sample ($R^2 = 0.70$) than for the Ni sample ($R^2 = 0.56$). This should be related to the stronger scatter of the Ni data as can be seen from the larger width of the points cloud distribution. Indeed, considering close grain orientations, the measured indentation

moduli can sometimes be very different whereas any physical model will predict close values. This issue unavoidably leads to errors between predictions and observations and justify the need to adopt a statistical approach as the Bayesian inference to handle the experimental uncertainties.

Accordingly, given the reliability of our experimental measurements for the IN718 sample and the good match with the Vlassak and Nix's model, the SEC obtained by the present approach could serve as reference for future studies, especially considering the few, and not totally reliable, data currently available in the literature (Haldipur, 2006; Martin *et al.*, 2014; Schröder *et al.*, 2023. It is important also to notice that if indents in carbides were systematically removed, the presence of the small and narrowly distributed precipitates, $L1_2$-γ'-$Ni_3(Ti,Al)$ and DO_{22}-γ"-Ni_3Nb, cannot be excluded from the indented volumes. Hence, the SEC found for the IN718 sample should be interpreted as effective elastic constants that include the effect of these precipitates.

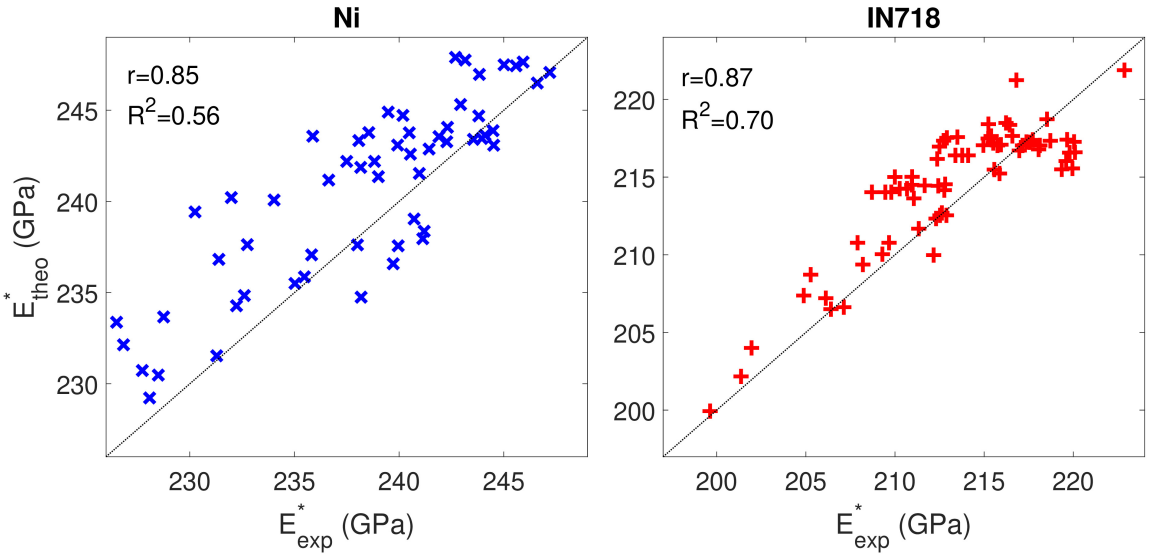

Figure 5.18: Indentation moduli E^*_{theo} computed with the Vlassak and Nix's model using the corrective multiplicative factor of 1.06 and the retained values for A, $\nu_{\langle 100\rangle}$ and $E_{\langle 100\rangle}$ in Tables 5.1 and 5.2 versus the experimental indentation moduli E^*_{exp} (average per grain). r denotes the Pearson correlation coefficient while the R^2 score corresponds to the coefficient of determination.

Regarding the use of the Vlassak and Nix's model with a Berkovich tip, it must be noticed that the value of the corrective factor of 1.06 has no influence on the distributions of A and $\nu_{\langle 100\rangle}$ since the method is based on E^* ratios. However, the value of this corrective factor may affect the posterior distributions of $E_{\langle 100\rangle}$. Moreover, it is noteworthy that the orientation of

the Berkovich tip in the indentation surface is not considered in the current model. This can create some uncertainties and might explain the need to consider relatively high values of σ_{E^*} in the Bayesian inference simulations to reach convergence. Indeed, increasing the experimental variances lead to an overlapping with a larger set of possible theoretical values, thereby improving the inclusivity of the model. As mentioned in Section 1.4.2, the Vlassak and Nix's model should actually represent a better approximation of E^* values obtained by spherical indentation tests even though the contact area is still, in general, not circular but elliptic due to anisotropic elasticity and though a real tip is never perfectly spherical either. The Vlassak and Nix model can be considered as very good approximation to estimate E^* from spherical indentation tests even though the contact area is in general not circular but elliptic in anisotropic elasticity for a random surface and though the real tip is never perfectly spherical. However, it affects the distributions of $E_{<100>}$. Various reasons can be put forward to explain the underestimation of $E_{<100>}$ from spherical indentation such as inaccurate definitions of the contact's points which influence directly the values of h_0 used to compute the stiffness or bad calibration of the indenter's radius. Also, the fact to perform a linear analysis of the oscillatory indentation may have an influence. Indeed, as explained in Cheng *et al.*, 2006, when a spherical indenter is driven by a sinusoidal force, the displacement to the power 3/2 is sinusoidal not the displacement itself as assumed in our analysis.

5.6 Conclusion

The results presented in this chapter demonstrate the effectiveness of combining nanoindentation experiments, theoretical modeling, and Bayesian inference to characterize the anisotropic elastic properties of high-purity Ni and Inconel 718 (IN718). By analyzing multiple datasets, including high-speed nanoindentation mapping (HSNM) and spherical nanoindentation tests, single-crystal elastic constants were inferred with a high degree of robustness. The results not only validate the applicability of Bayesian inference for handling experimental uncertainties but also highlight its ability to provide meaningful posterior probability distributions, even when working with limited or noisy datasets.

The comparison of results across different experimental approaches revealed important in-

sights into the influence of data quality and quantity. The larger HSNM dataset provided more constrained posterior distributions and a stronger agreement with theoretical predictions, emphasizing the advantage of extensive mapping in capturing the anisotropic response of materials. In contrast, the spherical nanoindentation data, while more limited in scope, still produced reliable results, demonstrating the flexibility of the Bayesian framework in adapting to varying levels of experimental input.

The discussion highlighted the alignment of the inferred elastic constants with literature values, particularly for IN718, where the data quality was superior. The stabilized median values of the posterior distributions were identified as the most reliable estimates, given their consistency across varying levels of experimental uncertainty and their alignment with theoretical expectations. The influence of experimental variability was most evident in the Ni dataset, where increased scatter led to broader regions of uncertainty. Nonetheless, the results for both materials reinforce the reliability of the Vlassak and Nix model in predicting anisotropic elastic behavior. Overall, this chapter establishes the significance of combining experimental data and statistical inference to advance the characterization of anisotropic materials. The method developed serves as a robust framework for future studies on a wide range of materials, especially when exploring spaces of new material compositions.

Conclusion

In this thesis, we proposed and demonstrated a protocol that combines nanoindentation experiments, the Vlassak and Nix model, and Bayesian inference to estimate the single-crystal elastic constants (SECs) of cubic materials, focusing on high-purity Ni as a known sample material to validate and Inconel 718 (IN718), as a less-known one. By combining these techniques, we can systematically produce meaningful statistics using the Bayesian inference from which we can make a choice of parameters set. By using the ratios of E^* instead of each measurement individually, not only did this approach address the inherent variability in both measurements and modelling, it was also able to provide for more input points and reduce the time needed to converge to a solution as the ratio only depend on two dimensionless parameters (A and $\nu_{\langle 100 \rangle}$) of which limits are well-known and material's independent.

The use of High-Speed Nanoindentation Mapping (HSNM) provided extensive datasets for both Ni and IN718, revealing in the process a strong correlation between the experimental modulus measurements and theoretical prediction. Its large dataset helped in narrowing the posterior distributions, highlighting the advantages of widespread mapping across varying crystallographic orientations. By contrast, the smaller spherical indentation dataset for Ni, while only containing 21 points, still yielded physically meaningful distribution, demonstrating the flexibility of our Bayesian approach in handling varying data qualities and quantities.

A comparison of the final, inferred parameters with literature showed that, for both Ni and IN718, our estimations lie within previously reported ranges, albeit being in the lower ranges of it. Notably, for IN718, our results are particularly reliable due to the high quality of the experimental

data, making them potentially useful as reference elastic constants for future studies. Moreover, the choice of the stabilized median (or maximum a posteriori for the spherical case) was justified by the non-symmetric shape of many posterior distributions and their good alignment with theoretical expectations and literature benchmarks.

Another significant point lies in the necessity of careful pre-processing and data quality checks of the experimental data. The outliers were removed, such as those located near grain boundaries, to ensure robust inputs. Consequently, this filtering process improved the final inference results and underscores the importance of methodical data-curation strategies.

Beyond the insights gained into Ni and IN718, the broader implications of this work suggest that combining nanoindentation, semi-analytical modeling such as the Vlassak and Nix model, and Bayesian inference can be extended to other anisotropic materials of cubic symmetry. The significant time reduction achieved by substituting finite element simulations with the Vlassak and Nix model is a central advantage, making this protocol suitable for faster, large-scale characterization efforts, such as exploring new material composition spaces rapidly. Future refinements could include further optimization of the indentation process and better calibrations of the spherical tips.

Looking ahead, several opportunities exist to enhance and expand the presented protocol. A primary step will involve refining the spherical nanoindentation procedure used, particularly in terms of calibration, repeatability, and data processing. Standardization across experimental nanoindentation practices—especially in protocols for mapping and pre-processing—will be crucial for ensuring comparability across studies and institutions. Additionally, applying this approach to more complex crystallographic systems, such as hexagonal close-packed (HCP) structures, will test the generalization and robustness of the method beyond cubic materials.

Further validation of the protocol should also target increasingly challenging material systems. Applying the methodology to multiphase alloys or completely unknown materials could provide critical insights into its versatility and limits. In such cases, the Bayesian inference's ability to handle sparse, noisy, or uncertain data becomes a distinct advantage. As material systems grow in complexity, this capability will be especially valuable. Moreover, this protocol aligns well with the emerging needs of materials discovery and design, offering a powerful tool for exploring vast

material spaces in a high-throughput and uncertainty-aware fashion.

Lastly, this work highlights the growing importance of advanced statistical tools in materials science. The successful integration of Bayesian inference not only enhances the precision of inferred mechanical properties but also advocates for its broader adoption within the field. By embedding statistical reasoning at the heart of experimental interpretation, researchers can better quantify uncertainty and gain deeper confidence in their results. The findings of this thesis thus not only contribute to the methodological landscape but also promote a more rigorous, data-driven culture in experimental mechanics and materials characterization.

In summary, this study demonstrates that merging experimental measurements with Bayesian inference is a powerful and efficient approach to capturing both tendencies and uncertainties of the probed mechanical properties. As material design and development is becoming increasingly complex, the ability to pinpoint elastic constants in a high-throughput, reliable, and uncertainty-conscious way will play an essential role in accelerating materials-related innovations. The methodology and findings presented in this thesis provide a solid foundation for future work on a diverse range of anisotropic cubic polycrystalline materials.

Bibliography

Abramowitz, M. and Stegun, I. A. (1968). *Handbook of mathematical functions with formulas, graphs, and mathematical tables*. Vol. 55. US Government printing office.

Alers, G., Neighbours, J., and Sato, H. (1960). "Temperature dependent magnetic contributions to the high field elastic constants of nickel and an Fe-Ni alloy". *Journal of Physics and Chemistry of Solids* 13.1-2, pp. 40–55.

Aspinall, J., Armstrong, D., and Pasta, M. (2022). "EBSD-coupled indentation: nanoscale mechanics of lithium metal". *Materials Today Energy* 30, p. 101183. DOI: 10.1016/j.mtener.2022.101183.

Bacon, D., Barnett, D., and Scattergood, R. O. (1980). "Anisotropic continuum theory of lattice defects". *Progress in Materials Science* 23, pp. 51–262.

Barnett, D. and Lothe, J. (1975). "Line force loadings on anisotropic half-spaces and wedges". *Physica Norvegica* 8, pp. 13–22.

Bayes, T. (1763). "LII. An essay towards solving a problem in the doctrine of chances. By the late Rev. Mr. Bayes, FRS communicated by Mr. Price, in a letter to John Canton, AMFR S". *Philosophical transactions of the Royal Society of London* 53, pp. 370–418.

Bozorth, R., Mason, W., and McSkimin, H. (1951). "Frequency dependence of elastic constants and losses in nickel". *Bell System Technical Journal* 30.4, pp. 970–989.

Bozorth, R., Mason, W., McSkimin, H., and Walker, J. (1949). "Elastic Constants and Internal Loss of Single Nickel Crystals". *Physical Review* 75.12, p. 1954.

Caer, C., Patoor, E., Berbenni, S., and Lecomte, J.-S. (2013). "Stress induced pop-in and pop-out nanoindentation events in CuAlBe shape memory alloys". *Materials Science and engineering: A* 587, pp. 304–312.

Castillo, A. and Kalidindi, S. R. (2019). "A Bayesian framework for the estimation of the single crystal elastic parameters from spherical indentation stress-strain measurements". *Frontiers in Materials* 6, p. 136.

Cazzani, A. and Rovati, M. (2003). "Extrema of Young's modulus for cubic and transversely isotropic solids". *International Journal of Solids and Structures* 40.7, pp. 1713–1744.

Cheng, Y.-T., Ni, W., and Cheng, C.-M. (2006). "Nonlinear analysis of oscillatory indentation in elastic and viscoelastic solids". *Physical review letters* 97.7, p. 075506.

Cho, J., Dye, D., Conlon, K., Daymond, M., and Reed, R. (2002). "Intergranular strain accumulation in a near-alpha titanium alloy during plastic deformation". *Acta materialia* 50.19, pp. 4847–4864.

D'Agostini, G. (2003). "Bayesian inference in processing experimental data: principles and basic applications". *Reports on Progress in Physics* 66.9, p. 1383.

De Klerk, J. (1959). "Ultrasonic Wave Propagation in a Nickel Single Crystal". *Proceedings of the Physical Society* 73.3, p. 337.

De Klerk, J. and Musgrave, M. (1955). "Internal conical refraction of transverse elastic waves in a cubic crystal". *Proceedings of the Physical Society. Section B* 68.2, p. 81.

Delbergue, D., Texier, D., Lévesque, M., and Bocher, P. (2019). "Diffracting-grain identification from electron backscatter diffraction maps during residual stress measurements: a comparison between the sin2ψ and cosα methods". *Journal of Applied Crystallography* 52.4, pp. 828–843.

deWit, R. (2008). "Elastic constants and thermal expansion averages of a nontextured polycrystal". *Journal of mechanics of materials and structures* 3.2, pp. 195–212.

Diaz-Francés, E. and Rubio, F. J. (2013). "On the existence of a normal approximation to the distribution of the ratio of two independent normal random variables". *Statistical Papers* 54, pp. 309–323.

Doerner, M. F. and Nix, W. D. (1986). "A method for interpreting the data from depth-sensing indentation instruments". *Journal of Materials research* 1.4, pp. 601–609.

Epstein, S. and Carlson, O. (1965). "The elastic constants of nickel-copper alloy single crystals". *Acta metallurgica* 13.5, pp. 487–491.

Everaerts, J., Papadaki, C., Li, W., and Korsunsky, A. M. (2019). "Evaluation of single crystal elastic stiffness coefficients of a nickel-based superalloy by electron backscatter diffraction and nanoindentation". *Journal of the Mechanics and Physics of Solids* 131, pp. 303–312.

Fernandez-Zelaia, P., Joseph, V. R., Kalidindi, S. R., and Melkote, S. N. (2018). "Estimating mechanical properties from spherical indentation using Bayesian approaches". *Materials & Design* 147, pp. 92–105.

Field, J. and Swain, M. (1993). "A simple predictive model for spherical indentation". *Journal of Materials Research* 8.2, pp. 297–306.

Field, J. and Swain, M. (1995). "Determining the mechanical properties of small volumes of material from submicrometer spherical indentations". *Journal of Materials Research* 10.1, pp. 101–112.

Fischer-Cripps, A. C. and Nicholson, D. (2004). "Nanoindentation. Mechanical engineering series". *Appl. Mech. Rev.* 57.2, B12–B12.

Fréour, S., Gloaguen, D., François, M., Perronnet, A., and Guillén, R. (2005). "Determination of single-crystal elasticity constants in a cubic phase within a multiphase alloy: X-ray diffraction measurements and inverse-scale transition modelling". *Journal of Applied Crystallography* 38.1, pp. 30–37.

Fréour, S., Gloaguen, D., François, M., Guillen, R., Girard, E., and Bouillo, J. (2002). "Determination of the macroscopic elastic constants of a phase embedded in a multiphase polycrystal-application to the β-phase of a Ti-17 titanium based alloy". In: *Materials science forum*. Vol. 404, pp. 723–728.

Gemperlova, J., Paidar, V., and Kroupa, F. (1989). "Compatibility stresses in deformed bicrystals". *Czechoslovak Journal of Physics B* 39.4, pp. 427–446.

Gerberich, W., Nelson, J., Lilleodden, E., Anderson, P., and Wyrobek, J. (1996). "Indentation induced dislocation nucleation: The initial yield point". *Acta Materialia* 44.9, pp. 3585–3598. DOI: https://doi.org/10.1016/1359-6454(96)00010-9.

Habiyaremye, F., Guitton, A., Chen, X., Richeton, T., Berbenni, S., Schäfer, F., Laplanche, G., and Maloufi, N. (2024). "Influence of pre-existing configurations of dislocations on the initial pop-in load during nanoindentation in a CrCoNi medium-entropy alloy". *Philosophical Magazine* 104.3, pp. 137–160. DOI: 10.1080/14786435.2023.2290541.

Haldipur, P. (2006). *Material characterization of nickel-based super alloys through ultrasonic inspection*. Iowa State University.

Hertz, H. (1896). *Miscellaneous papers*. Macmillan.

Hielscher, R. and Schaeben, H. (2008). "A novel pole figure inversion method: Specification of the MTEX algorithm". *Journal of Applied Crystallography* 41.6, pp. 1024–1037. DOI: 10.1107/S0021889808030112.

Hill, R. (1952). "The elastic behaviour of a crystalline aggregate". *Proceedings of the Physical Society. Section A* 65.5, p. 349.

Honda, K. and Shirakawa, Y. (1937). "On Young's modulus of elasticity of single crystal of nickel". *J. Japan Inst. Metals* 1, pp. 217–219.

Kalidindi, S. R. and Pathak, S. (2008). "Determination of the effective zero-point and the extraction of spherical nanoindentation stress–strain curves". *Acta Materialia* 56.14, pp. 3523–3532.

Kang, S., Jung, Y.-S., Yoo, B.-G., Jang, J.-i., and Lee, Y.-K. (2012). "Orientation-dependent indentation modulus and yielding in a high Mn twinning-induced plasticity steel". *Materials Science and Engineering: A* 532, pp. 500–504. DOI: https://doi.org/10.1016/j.msea.2011.10.116.

King, R. (1987). "Elastic analysis of some punch problems for a layered medium". *International Journal of Solids and Structures* 23.12, pp. 1657–1664.

Ledbetter, H. M. and Reed, R. P. (1973). "Elastic properties of metals and alloys, I. Iron, nickel, and iron-nickel alloys". *Journal of Physical and Chemical Reference Data* 2.3, pp. 531–618.

Levy, S. and Truell, R. (1953). "Ultrasonic attenuation in magnetic single crystals". *Reviews of Modern Physics* 25.1, p. 140.

Lhadi, S., Berbenni, S., Gey, N., Richeton, T., and Germain, L. (2018). "Micromechanical modeling of the effect of elastic and plastic anisotropies on the mechanical behavior of β-Ti alloys". *International Journal of Plasticity* 109, pp. 88–107.

Li, T., Gao, Y., Bei, H., and George, E. P. (2011). "Indentation Schmid factor and orientation dependence of nanoindentation pop-in behavior of NiAl single crystals". *Journal of the Mechanics and Physics of Solids* 59.6, pp. 1147–1162.

Marano, A., Ribart, C., and Proudhon, H. (2024). "Towards a data platform for multimodal 4D mechanics of material microstructures". *Current Opinion in Solid State and Materials Science* submitted.

Martin, G., Ochoa, N., Sai, K., Hervé-Luanco, E., and Cailletaud, G. (2014). "A multiscale model for the elastoviscoplastic behavior of Directionally Solidified alloys: Application to FE structural computations". *International Journal of Solids and Structures* 51.5, pp. 1175–1187.

Matthies, S., Priesmeyer, H., and Daymond, M. (2001). "On the diffractive determination of single-crystal elastic constants using polycrystalline samples". *Journal of applied crystallography* 34.5, pp. 585–601.

McSkimin, H. (1953). "Measurement of elastic constants at low temperatures by means of ultrasonic waves–data for silicon and germanium single crystals, and for fused silica". *Journal of applied physics* 24.8, pp. 988–997.

Mejri, M., Malard, B., Thimont, Y., Connétable, D., Floquet, P., Laloo, R., Proietti, A., and Estournès, C. (2022). "Investigation of the mechanical properties of Mn15Si26 via EBSD-nanoindentation coupling and ab-initio calculation". *Journal of Alloys and Compounds* 900, p. 163458.

Millan-Espitia, N. and Kalidindi, S. R. (2022). "Study of a Bimodal α–β Ti Alloy Microstructure Using Multi-Resolution Spherical Indentation Stress-Strain Protocols". *Journal of Composites Science* 6.6, p. 162.

Millan-Espitia, N., Mohan, S., Pilchak, A. L., and Kalidindi, S. R. (2021). "Mechanical Responses of Primary-α Ti Grains in Polycrystalline Samples: Part I—Measurements of Spherical Indentation Stress–Strain Curves". *Integrating Materials and Manufacturing Innovation* 10, pp. 82–98.

Neighbours, J., Bratten, F., and Smith, C. S. (1952). "The elastic constants of nickel". *Journal of Applied Physics* 23.4, pp. 389–393.

Oliver, W. C. and Pharr, G. M. (2004). "Measurement of hardness and elastic modulus by instrumented indentation: Advances in understanding and refinements to methodology". *Journal of materials research* 19.1, pp. 3–20.

Oliver, W. C. and Pharr, G. M. (1992). "An improved technique for determining hardness and elastic modulus using load and displacement sensing indentation experiments". *Journal of materials research* 7.6, pp. 1564–1583.

Pathak, S. and Kalidindi, S. R. (2015). "Spherical nanoindentation stress–strain curves". *Materials science and engineering: R: Reports* 91, pp. 1–36.

Proudhon, H., Richeton, T., Texier, D., Dziri, A., Sirvin, Q., and Legros, M. (2024). *Correlative analysis of EBSD and high speed nanoindentation mapping datasets in pure titanium.* DOI: 10.5281/zenodo.10842559.

Purohit, R. R. P. P. R., Richeton, T., Berbenni, S., Germain, L., Gey, N., Connolley, T., and Castelnau, O. (2021). "Estimating single-crystal elastic constants of polycrystalline β metastable titanium alloy: A Bayesian inference analysis based on high energy X-ray diffraction and micromechanical modeling". *Acta Materialia* 208, p. 116762.

Raghunathan, S., Stapleton, A., Dashwood, R., Jackson, M., and Dye, D. (2007). "Micromechanics of Ti–10V–2Fe–3Al: In situ synchrotron characterisation and modelling". *Acta Materialia* 55.20, pp. 6861–6872.

Rappel, H., Beex, L. A., and Bordas, S. P. (2018). "Bayesian inference to identify parameters in viscoelasticity". *Mechanics of Time-Dependent Materials* 22, pp. 221–258.

Reuss, A. and Angnew, Z. (1929). "A calculation of the bulk modulus of polycrystalline materials". *Math Meth* 9, p. 55.

Reynolds, M. B. (1952). *The determination of the elastic constants of metals by the ultrasonic pulse technique*. Knolls Atomic Power Laboratory.

Richeton, T. and Berbenni, S. (2013). "Effects of heterogeneous elasticity coupled to plasticity on stresses and lattice rotations in bicrystals: A Field Dislocation Mechanics viewpoint". *European Journal of Mechanics-A/Solids* 37, pp. 231–247.

Richeton, T., Tiba, I., Berbenni, S., and Bouaziz, O. (2015). "Analytical expressions of incompatibility stresses at Σ3¡ 111¿ twin boundaries and consequences on single-slip promotion parallel to twin plane". *Philosophical Magazine* 95.1, pp. 12–31.

Sakurai, J., Fujii, M., Nakamura, Y., and Takaki, H. (1964). "Elastic constants of NI-FE and NI-CU alloys". *Journal of the Physical Society of Japan* 19.3, pp. 308–310.

Salama, K. and Alers, G. (1969). "Third-order elastic moduli of pure nickel and some dilute copper-nickel alloys". *IEEE Trans. Sonics Ultrason* 1, p. 28.

Schröder, J., Heldmann, A., Hofmann, M., Evans, A., Petry, W., and Bruno, G. (2023). "Determination of diffraction and single-crystal elastic constants of laser powder bed fused Inconel 718". *Materials Letters* 353, p. 135305.

Seehaus, M., Lee, S.-H., Stollenwerk, T., Wheeler, J. M., and Korte-Kerzel, S. (2023). "Estimation of directional single crystal elastic properties from nano-indentation by correlation with EBSD and first-principle calculations". *Materials & Design* 234, p. 112296.

Shirakawa, Y. and Numakura, K. (1958). "Elasticity Constants of Single Crystals of Nickel-Copper Alloys". *Sci. Reports Res. Institutes, Tohoku Univ. Ser. A, Physics, Chem. Metall* 10, pp. 51–57.

Shirakawa, Y., Tanji, Y., Moriya, H., and Oguma, I. (1969). "Elastic constants of Ni and Ni-Fe–FCC–alloys". *J Japan Inst Metals* 33.10, pp. 1196–1202.

Sneddon, I. N. (1965). "The relation between load and penetration in the axisymmetric boussinesq problem for a punch of arbitrary profile". *International Journal of Engineering Science* 3.1, pp. 47–57. DOI: https://doi.org/10.1016/0020-7225(65)90019-4.

Stroh, A. (1958). "Dislocations and cracks in anisotropic elasticity". *Philosophical magazine* 3.30, pp. 625–646.

Texier, D., Richeton, T., Proudhon, H., Dziri, A., Sirvin, Q., and Legros, M. (2024). "Increase in elastic and hardness anisotropy of titanium with oxygen uptake due to high temperature oxidation: a multimodal framework using high speed nanoindentation mapping". *Materials Characterization* XX.XX, Under review.

Tiba, I., Richeton, T., Motz, C., Vehoff, H., and Berbenni, S. (2015). "Incompatibility stresses at grain boundaries in Ni bicrystalline micropillars analyzed by an anisotropic model and slip activity". *Acta Materialia* 83, pp. 227–238.

Timoshenko, T. and Goodier, J. (1951). *Theory of Elasticity*. 2nd Ed. McGraw-Hill, N.Y.

Ting, T. (1992). "Image singularities of Green's functions for anisotropic elastic half-spaces and bimaterials". *The Quarterly Journal of Mechanics and Applied Mathematics* 45.1, pp. 119–139.

VanLandingham, M. R. (2003). "Review of instrumented indentation". *Journal of research of the National Institute of Standards and Technology* 108.4, p. 249.

Venkatraman, A., McDowell, D. L., and Kalidindi, S. R. (2022). "Bayesian analysis of parametric uncertainties and model form probabilities for two different crystal plasticity models of lamellar grains in $\alpha+\beta$ titanium alloys". *International Journal of Plasticity* 154, p. 103289.

Vintaikin, E. (1966). "X-Ray Determination of the Elastic Constants of Pure Nickel and Its Alloy with Aluminum". In: *Soviet Physics Doklady*. Vol. 11, p. 91.

Vlassak, J., Ciavarella, M., Barber, J., and Wang, X. (2003). "The indentation modulus of elastically anisotropic materials for indenters of arbitrary shape". *Journal of the Mechanics and Physics of Solids* 51.9, pp. 1701–1721. DOI: 10.1016/S0022-5096(03)00066-8.

Vlassak, J. and Nix, W. D. (1993). "Indentation modulus of elastically anisotropic half spaces". *Philosophical Magazine A: Physics of Condensed Matter, Structure, Defects and Mechanical Properties* 67.5, pp. 1045–1056. DOI: 10.1080/01418619308224756.

Vlassak, J. and Nix, W. (1994). "Measuring the elastic properties of anisotropic materials by means of indentation experiments". *Journal of the Mechanics and Physics of Solids* 42.8, pp. 1223–1245. DOI: 10.1016/0022-5096(94)90033-7.

Voigt, W. (1928). "Lehrbuch der Kristallphysik (Textbook of crystal physics)". *BG Teubner, Leipzig und Berlin*.

Weaver, J. S., Priddy, M. W., McDowell, D. L., and Kalidindi, S. R. (2016). "On capturing the grain-scale elastic and plastic anisotropy of alpha-Ti with spherical nanoindentation and electron back-scattered diffraction". *Acta Materialia* 117, pp. 23–34.

Winckel, G. von (2004). *Legendre-Gauss Quadrature Weights and Nodes*.

Yamamoto, M. (1950). "On elastic constants of nickel crystals". *Physical Review* 77.4, p. 566.

Yin, J., Barnett, D. M., and Cai, W. (2010). "Efficient computation of forces on dislocation segments in anisotropic elasticity". *Modelling and Simulation in Materials Science and Engineering* 18.4, p. 045013.